ISOTHIOCYANATE LIGAND DERIVATIVES OF PLATINUM(II) TERPYRIDINES

by

Bradley Peter Waldron

B.Sc. (Hons), (University of KwaZulu-Natal)

Submitted in fulfillment of the requirements
for the degree of Master of Science in the
School of Chemistry
Faculty of Science and Agriculture
University of KwaZulu-Natal
Pietermaritzburg

September 2008

Abstract

The novel compounds $[Pt(trpy)(NCS)]SbF_6$ (**1**) and $[Pt\{4'\text{-}(Ph)trpy\}(NCS)]SbF_6$ (**2**) where trpy = 2,2':6',2''-terpyridine, have been synthesised and characterised by means of elemental analysis, infrared and ^1H NMR spectroscopy, and mass spectroscopy. Compounds **1** and **2** were also prepared with the labelled $S^{13}C^{15}N^-$ ion as co-ligand; their ^{13}C and ^{15}N NMR spectra recorded at room temperature in CD_3CN show that the ambidentate ion is coordinated to the Pt atom mainly (~ 95%) through the N atom, but that a small amount of the S-bound isomer also co-exists in an acetonitrile solution.

The synthesis of **1** is preceded by the isolation of yellow **1·CH$_3$CN—Y** (Y = yellow) for which the crystal structure has been determined by single crystal X-ray diffraction; this shows that the SCN^- ion is linearly bound to the Pt atom through the N atom in the solid state, and that the cation is planar. The solvate rapidly loses acetonitrile to form maroon **1—M** (M = maroon). The maroon compound exhibits ^{3}MMLCT (metal-metal-to-ligand charge transfer) emission in the solid state as evidenced by a red-shift in the emission maximum from 653 nm at 473 K to 770 nm at 80 K. However, there are anomalous changes in the emission intensity below 200 K; this phenomenon is explained in terms of competitive emission by defect sites in the material. Interestingly, **1—M** displays thermochromic behaviour (accompanied by phase changes at Ts > 473 K) that have been documented over the temperature range 80-548 K by means of photography, emission spectral and powder X-ray diffraction measurements. Compound **1—M** also exhibits selective and reversible vapochromic behaviour with acetonitrile, DMF and pyridine – the solvates are yellow. We also report solvent specific changes in the emission spectra between **1—M** and its acetonitrile, DMF and pyridine solvates. The thermo- and vapochromism of **1—M** are linked to the making and breaking of metallophilic Pt◦◦◦Pt interactions that occur when the planar cations slide in and out of different positions with respect to each other in a π-stack.

Single crystals of compound **2** are isolated by desolvation of single crystals of **2·CH$_3$CN**. The single-crystal to single-crystal transformation is easily reversed by exposing **2** to vapours of acetonitrile, as confirmed by X-ray structure determinations of **2** and **2·CH$_3$CN** performed on the *same* single crystal. These show that the SCN^- ion is linearly bound to the Pt atom through the N atom and that the cation is nearly planar. Significantly, there are only very small changes in the cation and anion atom positions between **2** and **2·CH$_3$CN**; thus, single crystals of **2** have a porous metal-organic structure with solvent accessible voids/channels. As such, **2** also sorbs methanol and acetone molecules from the vapour phase, the former without loss of single crystallinity, as confirmed by an X-ray crystal structure determination of **2·CH$_3$OH**. Single crystals of **2·(CH$_3$)$_2$CO** were obtained by direct crystallization from acetone and an X-ray structure determination performed. Interestingly, a single crystal **2·(CH$_3$)$_2$CO** desolvates under ambient conditions to give a single crystal of **2** with the original porous metal-organic crystal structure; on the other hand **2·CH$_3$OH** does not readily desolvate because of O─H◦◦◦S hydrogen-bonding. Compound **2** and its solvates are yellow, as expected, since the planar cations hardly move on solvent uptake – in marked contrast to the easily moved cations in **1─M** – suggestions as to why are given. Finally, we report the solid state photoluminescence (measured at 77 K) of **2**, **2·CH$_3$CN**, **2·CH$_3$OH**, **2·(CH$_3$)$_2$CO** and **2·CH$_3$OH_DS** where **DS** denotes desolvation of the methanol solvate. Emission from **2** is characterised by dual emission from ^{3}MLCT (metal-to-ligand charge transfer) and excimeric $^3(\pi\text{-}\pi^*)$ excited states; with the latter being the predominant origin of emission at 77 K. On the other hand, the **2·CH$_3$CN** and **2·(CH$_3$)$_2$CO** solvates give well defined monomeric ^{3}MLCT emission exclusively. The excimeric emission is representative of the cation packing arrangement in the crystal lattice, and the fact that it is not observed for **2·CH$_3$CN** and **2·(CH$_3$)$_2$CO** is probably a result of an increase in the potential energy barrier to the formation of excimers when free space is occupied by CH_3CN or $(CH_3)_2CO$ included in the crystal lattice. Emission by **2·CH$_3$OH** and **2·CH$_3$OH_DS** is further complicated by ^{3}MMLCT emission that arises because of d_{z^2}(Pt)-d_{z^2}(Pt) orbital interactions present in the solid. As a result multiple emission from ^{3}MLCT, excimeric and ^{3}MMLCT excited states is observed for **2·CH$_3$OH** and **2·CH$_3$OH_DS**.

Declaration

I *Bradley P. Waldron* declare that:

1. The research reported in this thesis, except where otherwise indicated, is my original work.
2. The thesis has not been submitted for any degree or examination at any other university.
3. This thesis does not contain other persons' data, pictures, graphs or other information, unless specifically acknowledged as being sourced from other researchers.
4. The thesis does not contain other persons' writing, unless specifically acknowledged as being sourced from other researchers. Where other written sources have been quoted:
    a. Their words have been rewritten but the general information attributed to them has been referenced;
    b. Where their exact words have been used, their writing has been placed inside quotation marks, and referenced.
5. This thesis does not contain text, graphics or tables copied and pasted from the internet, unless specifically acknowledged, and the source thereof being detailed in the thesis and in the References sections.

Signed: _____ (**Bradley P. Waldron**) Date: _____

I hereby certify that this is correct, and as the candidate's supervisor I have/have not approved this thesis for submission

Signed: _____ **Professor J. S. Field (supervisor)** Date: _____

Signed: _____ **Professor O. Q. Munro (co-supervisor)** Date: _____

Contents

Acknowledgements

I would like to extend my sincere gratitude and thanks to *Professor John Field*, whose enthusiasm and love of the chemistry has made the last two years exciting and unforgettable. The knowledge and experience gained whilst under his supervision has been invaluable, and made all the difference to my future studies. I am especially grateful for the daily talks, endless support and freedom to choose my own direction. His input during the write up of this thesis has been patient, constructive and guided me in the right direction.

I would also like to acknowledge the following people:

Professor Orde Munro for his technical and instrumental advice, and continuous support throughout the year. He has been instrumental in ensuring that state-of-the-art facilities and instruments are available, making the Department one of the best in South Africa.

Craig Grimmer for all the hard work, not only regarding the NMR spectroscopy of my complexes, but in many other areas. A special thanks for being so patient, willing to help and advise on almost anything. His input has been invaluable.

Paul Forder and *Clarence Mortlock* for all the time they spent making and designing weird and wonderful glassware for me. I would have been lost without their expertise.

Dr Murray Low for his support and expert advice over the last two years. The occasional suggestion to “get a move-on” kept me on track.

Les Mayne for designing and building the apparatus used for the solvation studies.

James Ryan for the many hours designing and building the heating block used for the high temperature emission and phase change studies.

Matthew Akerman and *Dr Kirsty Stewart* for their assistance with single crystal structure X-ray structure determinations.

Dr Louis Titshall for giving up his time to do my powder X-ray diffraction experiments.

The laboratory technicians and friends in the Inorganic research lab for making the lab a great place to work and helping whereever possible.

Dr Peter Ledwaba for taking the time to teach me the essential laboratory techniques.

The *National Research Foundation* for funding.

Courtney and my Family for the endless support, understanding and encouragement they showed during the course of the write-up. For always pushing me to do better, looking after me and spending many boring hours keeping me company whilst I was writing.

1 Background and aims of the project

In this chapter we first provide background information relevant to the results presented in Chapters 2 and 3. In the last section we briefly outline the aims of the project.

1 Photophysics of ionic platinum terpyridines

1.1 Introduction

The compounds that are the subject of study in this thesis fall into the category of ionic terpyridyl ligand complexes of platinum(II) with the general formula, [Pt{4'-(R)trpy}X]A; where trpy is 2,2':6',2''-terpyridine, X^- is the co-ligand, A^- is typically a large counterion, and R is a possible substituent in the 4'-position of the trpy moiety. Typical choices for R, X^- and A^- are illustrated in Scheme 1.1. These complexes have been studied for a number of reasons, but the property of interest here is that they (specifically the cations) often exhibit novel photophysical properties, both in fluid solution and in the solid state.[1-36] This has led to a variety of potential applications such as:[3,4,6,7-9,14,17,19,21,25-30,36-41]

- potential sensors for chemical and biological analytes, e.g. coordinating molecules quench emission in fluid solution, binding at remote sites alters emission
- DNA metallo-intercalators
- solid state optical sensors in electrical devices which respond to changes in temperature, e.g. non-linear optical devices, light emitting diodes
- solid state vapochromic optical sensors
- luminescent labelling agents
- building blocks for luminescent supramolecular assemblies
- photosensitisers in solar energy conversion

- photogeneration of hydrogen from water.

In so far as the valence orbitals of the cations are concerned these are identified as follows: the HOMO is a platinum 5d orbital (probably, but not certainly, the $5d_{xy}$-orbital) and the LUMO is the low-lying π*-orbital on the trpy ligand. Clearly, the energy of the HOMO depends on the choice of co-ligand.[1,2,6,8,10,12,13,15-20,22,23-25,28,31-36] For example, for weak field ligands the HOMO will be relatively high in energy, while a strong field ligand will cause a greater d-orbital splitting and the HOMO will be correspondingly lower in energy. Similarly, the energy of the π*-LUMO can be influenced, but in this case by the introduction of a substituent in the 4'-position of the trpy moiety. However, with complexes of this type, the lowest energy absorption is invariably of the d-π* type, i.e. the lowest energy band in the absorption spectrum of the complex derives from a metal-to-ligand charge transfer (MLCT) transition. Also true for these complexes is that trpy ligand-based, or intraligand (IL), π-π* absorptions occur at higher energies.[1,2,6,8,10,12,13,15-20,22,23-25,28,30-36] To illustrate this point we have reproduced the absorption spectrum of $[Pt(trpy)Cl]^+$ in Figure 1.1.

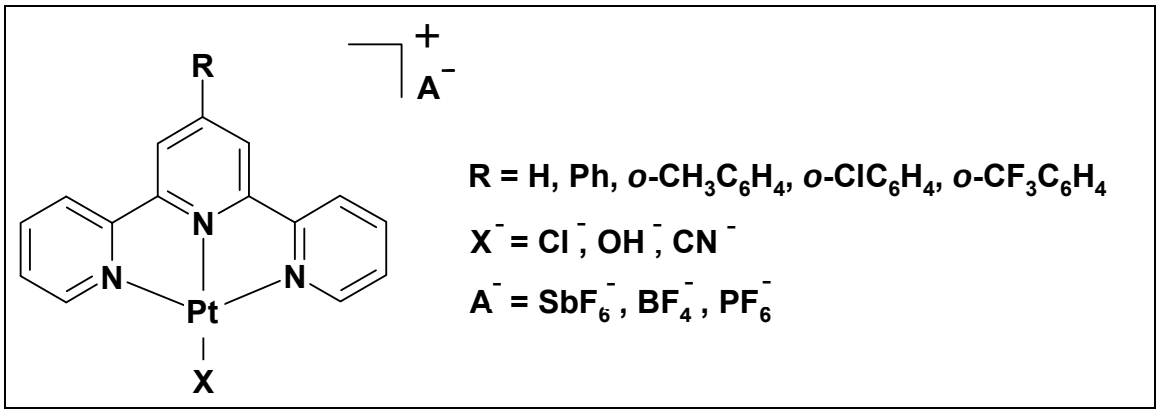

Scheme 1 Typical choices for substituents (R), counterion (A^-) and co-ligand (X^-) for ionic platinum terpyridines.[1,2,5,6,10-13,15-19,22,23,24,31,33]

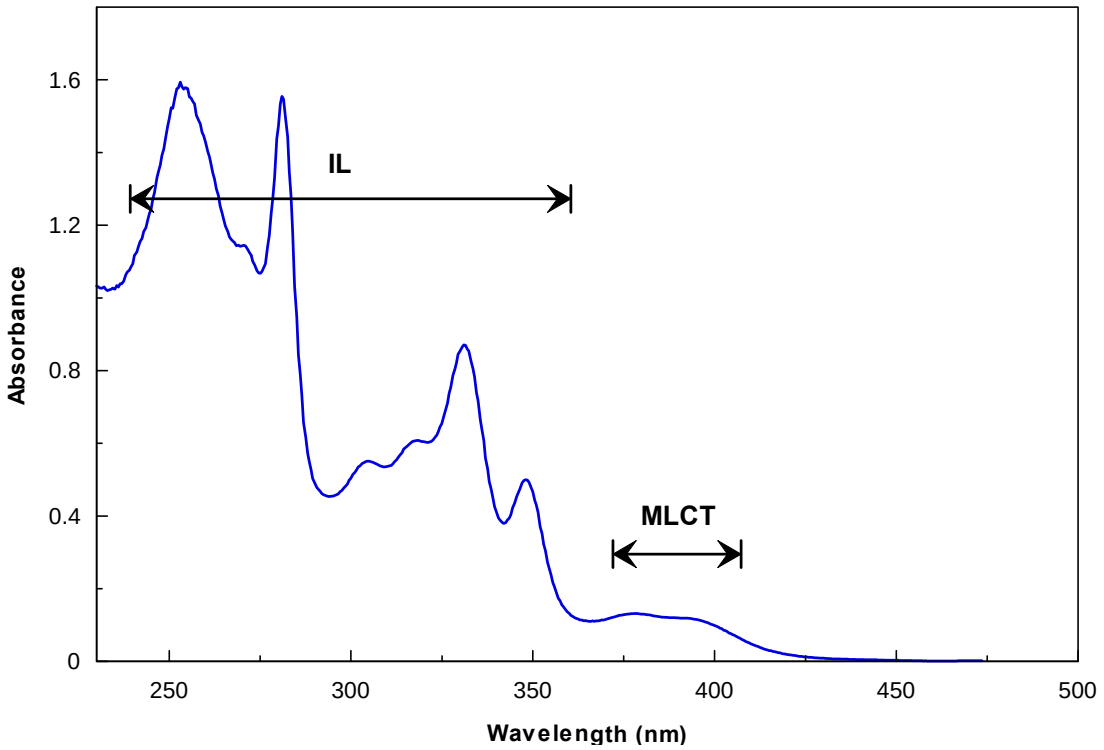

Figure 1.1 UV-vis absorption spectrum of $[Pt(trpy)Cl]^+$ measured in acetonitrile. The high energy π-π* and lower energy d-π* absorptions are indicated by the IL (intraligand) and MLCT (metal-to-ligand charge transfer) regions respectively.

1.2 Emission in fluid solution

We now address the question of what kind of photoluminescence can be expected from complexes of this type. Note that at this point of the discussion we are only concerned with emission in dilute *fluid solution*, i.e. where one is dealing with isolated cations. Given that the lowest energy absorption is d-π*, we can expect that the excited state first accessed on excitation of the complex will correspond to the electronic configuration, $(d)^1(\pi^*)^1$, where the unpaired electrons have parallel spins; as such it is labelled a ^{1}MLCT state. Intersystem crossing then occurs (rapidly due to the presence of the heavy metal atom) to give a ^{3}MLCT state of lower energy and from which radiative decay to the ground state can occur: see Figure 1.2. Thus ^{3}MLCT emission is anticipated and, in fact,

is extremely common for terpyridyl ligand complexes of platinum(II).[2,13,16-20,22,23-25,30,33] One example is shown in Figure 1.3. Note that the envelope of vibronic structure shows a monotonic decrease in intensity with increase in wavelength, a feature that is diagnostic for well-resolved monomeric ^{3}MLCT emission.[13,23] Two cautionary points need to be made at this juncture. Firstly, the ^{3}MLCT emission is usually quenched when the emission spectrum is recorded in coordinating solvents; this is because binding of the solvent to the vacant coordination sites above or below the platinum atom, provides a mechanism by which *non-radiative* decay to the ground state is facilitated: see Figure 1.2.[14] Secondly, one needs to recognise that singlet-triplet splitting for a d-π* excitation is relatively small, in particular when compared to the singlet-triplet splitting for the π-π* excitation.[42,43] What this means is that, though the d-π^* absorption is invariably the lowest in energy, the lowest energy excited state (the emitting state) may be ^{3}π-π*, or as it is sometimes labelled, ^{3}IL. Clearly, this is most likely to happen when the co-ligand bound to the platinum exerts a sufficiently strong field to force the energy of the d-π* absorption to a value so high that ^{3}IL emission can compete with ^{3}MLCT emission. However, pure ^{3}IL emission is seldom observed for ionic platinum terpyridines of the type discussed here. The best examples are complexes with the strong field cyanide ion as the co-ligand.[11,15,24,33] An example of such a spectrum is provided in Figure 1.4. Note the 'domed' profile for the Frank-Condon envelope of vibronic structure that is diagnostic of well-resolved ^{3}π-π* emission.[44-46]

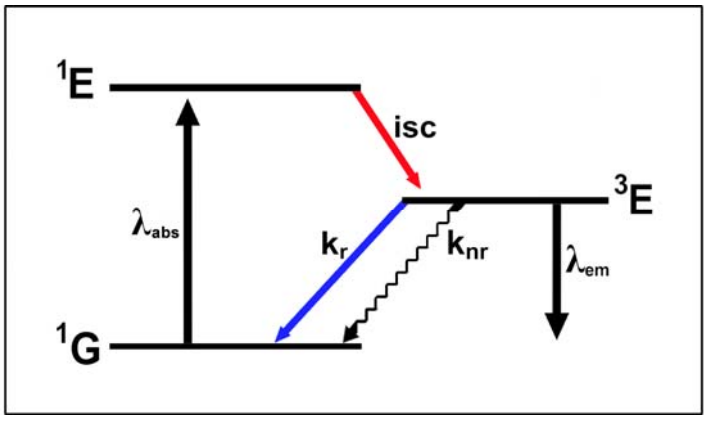

Figure 1.2 Jablonski diagram illustrating intersystem crossing (isc) for platinum terpyridines. 'k_r' is the radiative rate constant; and 'k_{nr}' is the non-radiative rate constant.

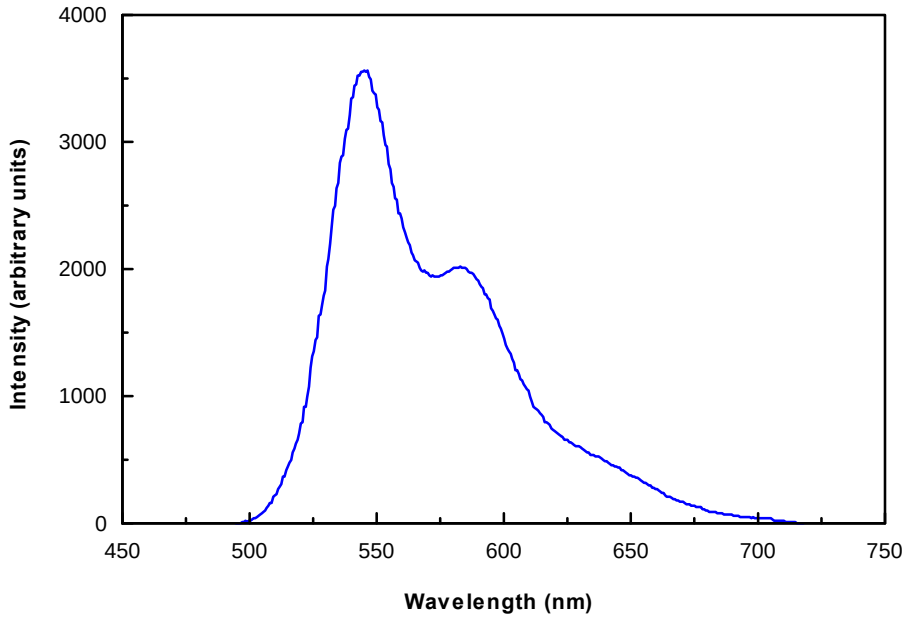

Figure 1.3 Emission spectrum of $[PtLCl]^+$ {where L = 4'-phenyl(dimesityboryl)-2,2':6',2''-terpyridine} assigned as ^{3}MLCT, recorded in chloroform at 298 K.[30]

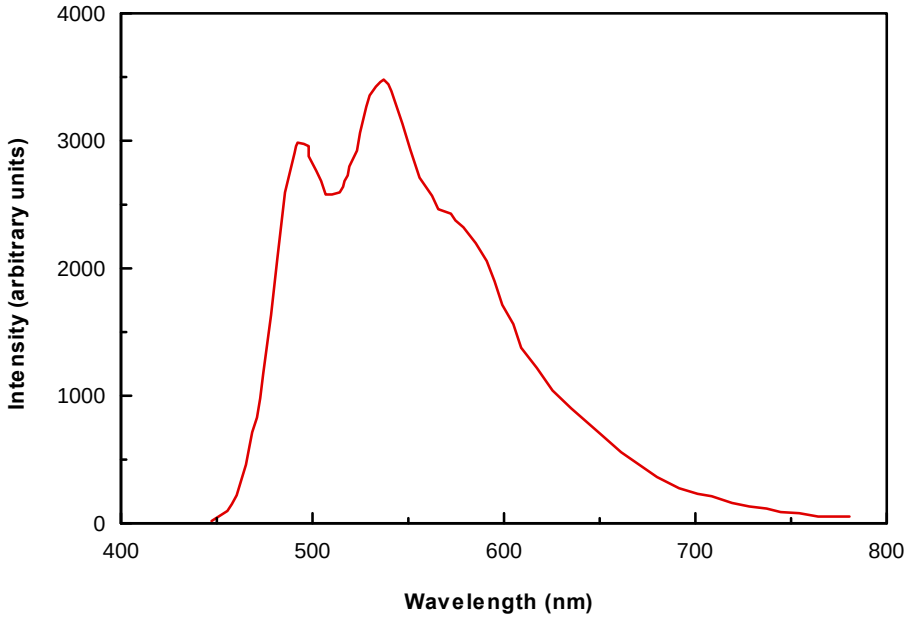

Figure 1.4 Emission spectrum of $[Pt\{4'\text{-}(o\text{-}CH_3C_6H_4)trpy\}(CN)]^+$ recorded in dichloromethane, assigned as ^{3}IL emission.[33]

1.3 Emission in the solid state

In this thesis the main focus is on the **solid state** emission by **isothiocyanate** ligand derivatives of platinum terpyridines, for reasons which will become apparent in subsequent chapters. We need, therefore, to introduce the role that intermolecular interactions in the solid state play in modifying the kind of emission discussed above for ionic platinum terpyridines in fluid solution. There are two important types of intermolecular interactions that can be present in the solid state structures of ionic platinum terpyridines. These are: (i) d_{z^2}(Pt)-d_{z^2}(Pt) orbital interactions and (ii) π(trpy)-π(trpy) interactions. Each of these will be discussed with particular reference to the geometry of the interactions and their effect on the emission spectrum recorded in the solid state. Note that there are examples of ionic platinum terpyridines that exhibit monomeric emission in the solid state, i.e. emission spectra are observed whose profiles match those recorded in fluid solution. These examples are also briefly discussed.

1.3.1 d_{z^2}(Pt)-d_{z^2}(Pt) orbital interactions

Square planar complexes of platinum(II) are able to form metallophilic interactions between adjacent Pt atoms as a result of the overlap of full Pt $5d_{z^2}$ orbitals which point above and below the plane of the cation. In order for effective metallophilic interactions to occur two structural criteria must be met. First, the adjacent Pt atoms must be within 3.5 Å of each other and second, the Pt atoms should be aligned vertically so as to facilitate d_{z^2}(Pt)-d_{z^2}(Pt) orbital overlap:[47] see Figure 1.5.

If the structural criteria are fulfilled the d_{z^2}-orbitals combine to form fully occupied bonding (dσ) and antibonding (dσ*) levels. Similarly the $6p_z$ orbitals of adjacent Pt atoms split into pσ and pσ* levels: see Figure 1.6. The stabilisation resulting from d_{z^2}(Pt)-d_{z^2}(Pt) orbital interactions does not originate directly from the orbital interaction, since both dσ and dσ* are fully occupied, i.e. a formal Pt─Pt bond is not formed. Rather, a configurational interaction between the dσ* and pσ orbitals stabilises the dσ* level resulting in a net energy decrease: see Figure 1.6.[48] It should be noted that the MO

diagram in Figure 1.6 is drawn for only two interacting cations. In the case of extended Pt∘∘∘Pt interactions further stabilisation of the dσ* level is expected.

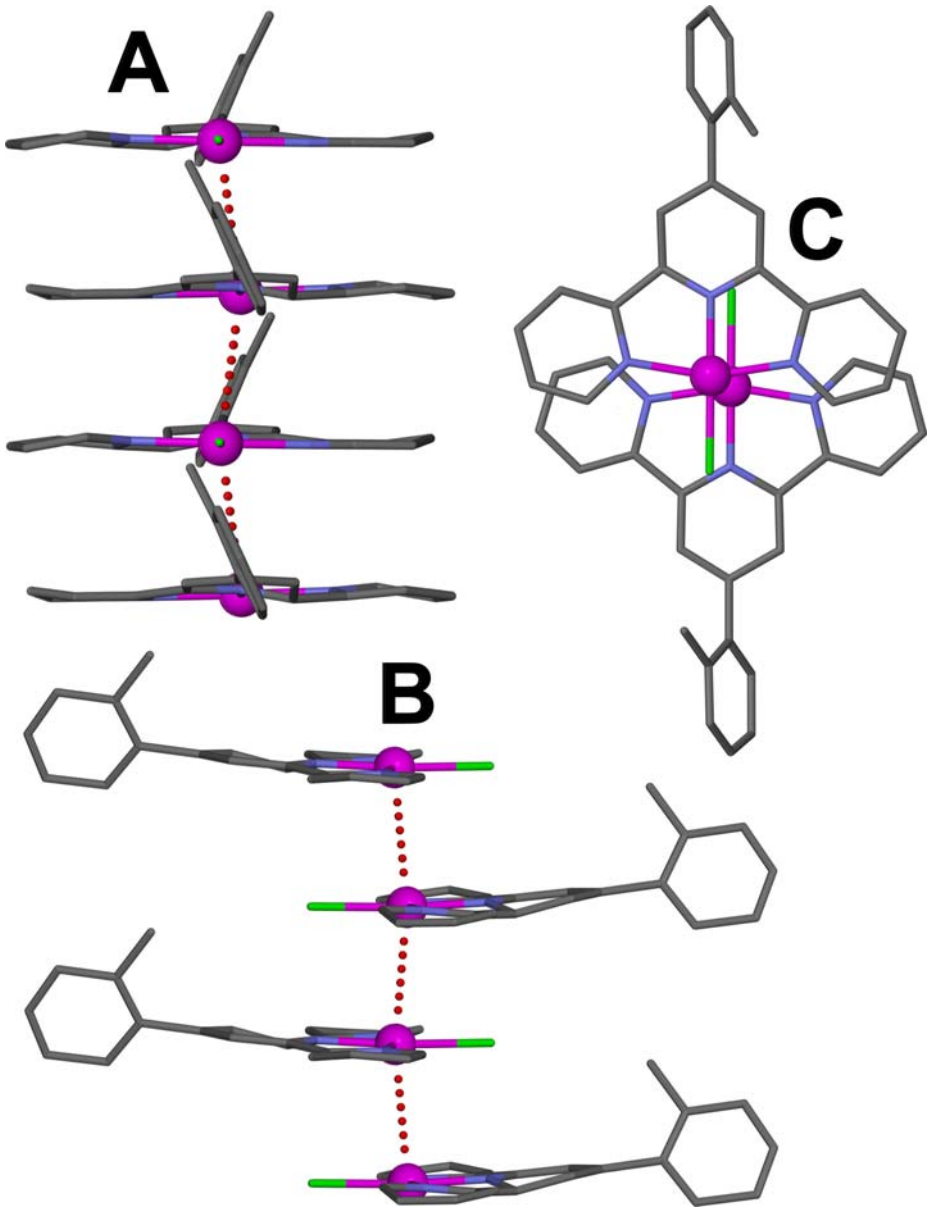

Figure 1.5 Different views of the cation stacks in [Pt{4'-(*o*-$CH_3C_6H_4$)trpy}Cl]SbF_6.[18] In both (A) and (B) the view is approximately parallel to the mean plane through PtN_3 unit; but the former is along the Pt-Cl bond whereas the latter is perpendicular to it. In (C) a view perpendicular to the PtN_3 plane is given that shows the near eclipsed relative orientation of the Pt atoms. The Pt∘∘∘Pt contacts shown by dotted red lines are < 3.5 Å.

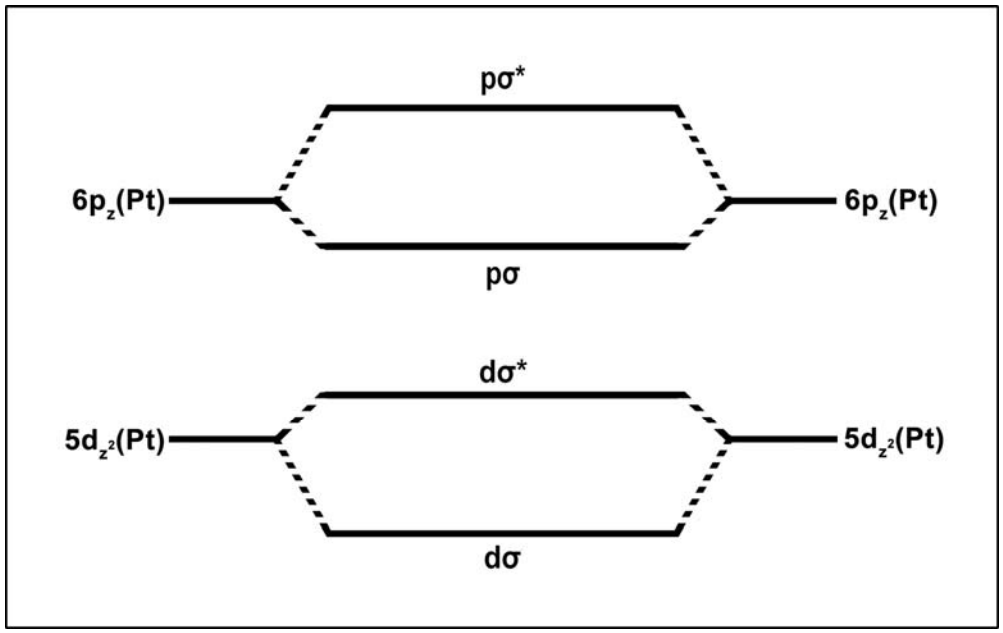

Figure 1.6 Molecular orbital diagram showing the origin of the stabilisation due to configurational interaction of the dσ* and pσ orbitals.[48]

As is the case in fluid solution, when isolated platinum terpyridine cations are excited by incident light an electron in the HOMO is elevated to the LUMO (a π* orbital on the trpy moiety). However in the presence of finite d_{z^2}(Pt)-d_{z^2}(Pt) orbital interactions, the HOMO is no longer an atomic d-orbital but rather the dσ* MO that is elevated to higher energies: see Figure 1.6. In such a situation the absorption is labelled ^{1}MMLCT (metal-metal-to-ligand charge transfer), and will be at a lower energy than that of the d-π* absorption for an isolated cation in fluid solution. As a result the 'modified' emission occurs at a lower energy and, following intersystem crossing, is assigned as ^{3}MMLCT emission. An example of ^{3}MMLCT emission is given in Figure 1.7. A single asymmetric band devoid of vibrational structure is observed at 280 K. Upon cooling the expected increase in intensity of the emission (as a result of reduced non-radiative decay to the ground state) is accompanied by a red-shift of the emission energy: see Figure 1.7. This can be explained by the fact that cooling causes contraction of the unit cell dimensions and hence a shortening of the Pt◦◦◦Pt distances. The shorter contact causes a further destabilisation of the dσ* orbital and a corresponding reduction of the HOMO-LUMO energy gap; hence the emission occurs at a lower energy. Note too that the band narrows on cooling from a

full-width-at-half-maximum (fwhm) value of ~ 1300 cm^{-1} at 280 K to one of ~ 1000 cm^{-1} at 80 K. All these features are diagnostic for ^{3}MMLCT emission. Also true is that when strong d_{z^2}(Pt)-d_{z^2}(Pt) orbital interactions extend through the solid, the colour of the material is invariably maroon or red. On the other hand, if the d_{z^2}(Pt)-d_{z^2}(Pt) orbital interactions are localised to Pt_2 dimers the solid is generally deep-yellow or orange in colour.[6,9,10,12,15,16,18,19,22-24,28,30,34-35] Finally, note that solutions of ionic platinum terpyridines (an environment which supports isolated cations) are invariably yellow in colour, regardless of the colour in the solid state.

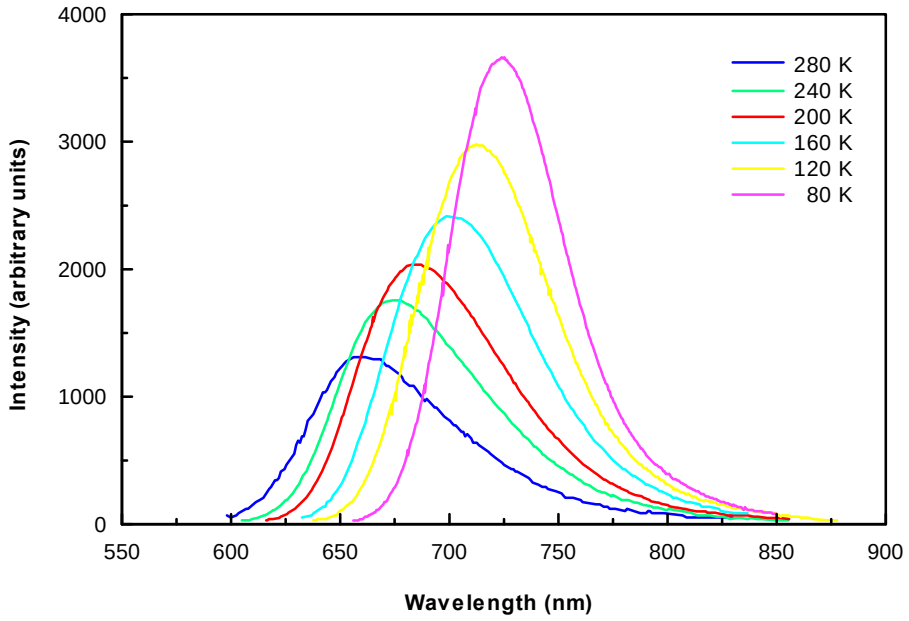

Figure 1.7 Solid state variable temperature emission spectra of [Pt{4'-(Ph)trpy}Cl]BF_4·CH_3CN (red form) recorded at 40 K intervals from 80-280 K. The red-shift of λ_{em}^{max} and band narrowing on cooling are characteristic of ^{3}MMLCT emission.[10]

1.3.2 π(trpy)-π(trpy) interactions

In the absence of d_{z^2}(Pt)-d_{z^2}(Pt) orbital interactions, π(trpy)-π(trpy) interactions may be present in the solid state; in fact, we are not aware of any examples of ionic platinum terpyridines that show the cations present as isolated monomers. Note that d_{z^2}(Pt)-d_{z^2}(Pt) orbital interactions and π(trpy)-π(trpy) interactions are not mutually exclusive; however if

the former are present, their influence usually dominates the photophysical properties of the compound. For instance, ionic platinum terpyridines with only π(trpy)-π(trpy) interactions are invariably yellow in colour whereas, as noted above, when strong d_{z^2}(Pt)-d_{z^2}(Pt) orbital interactions extend through the solid it will be red to maroon in colour.[6,9,10,12,15,16,18,19,22-24,28,30,34-35]

We now turn our attention to the nature of π(trpy)-π(trpy) interactions, in particular to the structural requirements for these interactions to be ***net*** stabilising. In a seminal paper, Hunters and Saunders proposed that aromatic moieties consist of positively charged σ-frameworks "sandwiched" between negatively charged π-electron clouds.[49] This model makes it clear that a co-facial (or directly eclipsed) juxtaposition of two aromatic systems will be destabilising, simply because repulsion between the π-electron clouds will dominate.[49] Instead, the model predicts that for the intermolecular interaction to be stabilising an offset π-stacked (or parallel displaced) geometry is favoured, since this maximises the π-σ attractive electrostatic forces.[49] Furthermore, their calculations show that the optimal perpendicular separation for a stabilising interaction between adjacent aromatic moieties is ~ 3.4 Å.[49] To summarise, the stabilising effect of so-called "π(trpy)-π(trpy)" interactions in π-stacked aromatic systems derives from ***non-covalent***, ***electrostatic*** π-σ attractive forces that overcome π-π repulsions.[49]

Janiak has further developed this model for application to *heteroatom* aromatic systems bonded to metals; of interest here is his analysis of the intermolecular interactions between adjacent terpyridyl ligands bonded to platinum.[50] Again, an offset π-stacked geometry is predicted on the grounds that π(trpy)-π(trpy) attractive electrostatic forces will be maximised. However, Janiak notes that, because of the concerted electron-withdrawing effect of the nitrogen atoms of the pyridine rings and the cationic metal atom, closer approach of the π-systems will be facilitated.[50] Moreover, if adjacent cations adopt a ***head-to-tail*** conformation, dipole-dipole interactions will stabilise the π-π interaction further. This conformation also has the advantage of placing the electronegative nitrogen atoms as far apart as possible, thus minimising repulsions.[50] Janiak is correct: the head-to-tail conformation, as indicated by a X•••Pt•••Pt•••X

(X = co-ligand) torsion angle of 180°, is the one most commonly found in the crystal structures of ionic platinum terpyridines.[10,15,16,18,19,23,24,33,35] However, as Janiak admits "the complex molecules and ligands can adopt different orientations relative to each other".[50] He cites the example of the crystal structure determination of [Pt{4'-Ph)trpy}Cl]BF_4,[10] which shows that "the Pt∘∘∘Pt contact is the major driving force which brings the systems together".[50] Thus relative orientations other than head-to-tail have been reported.[3,10,12,51]

We now address the question of the role (if any) of the π(trpy)-π(trpy) interactions on the solid state photophysical properties of ionic platinum terpyridines. As it turns out there is no clear explanation in the literature of the link between the π(trpy)-π(trpy) interactions as evidenced by a crystal structure determination, and the solid state photoluminescent properties of the compound. For this reason, we start by simply describing a well characterised and representative example.

This is the yellow complex [Pt{4'-(*o*-$CH_3C_6H_4$)trpy}Cl]BF_4: in Figure 1.8 the cation-cation overlap is illustrated, whilst in Figure 1.9 the variable temperature solid state emission spectra are shown.[18]

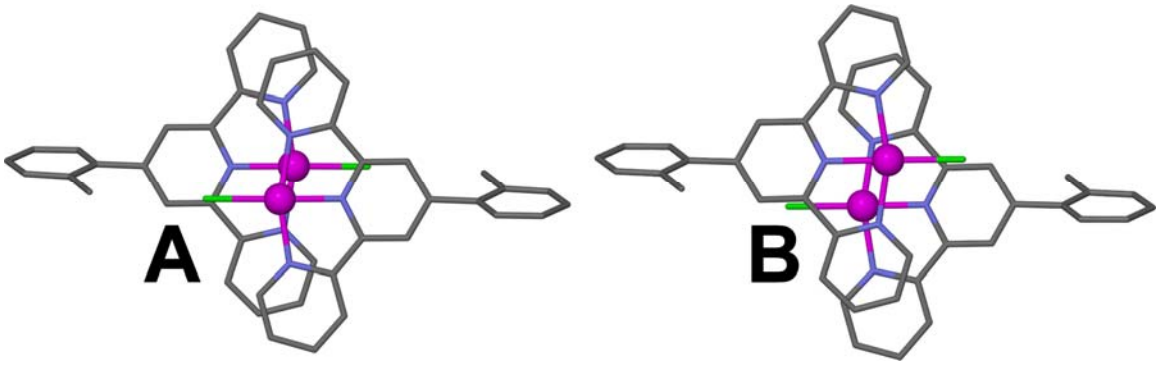

Figure 1.8 View perpendicular to the PtN_3 coordination plane of pairs of cations in the cation stacks present in the crystal structure [Pt{4'-(*o*-$CH_3C_6H_4$)trpy}Cl]BF_4. In (A) the methyl groups point into the space between the cations while in (B) they point outwards. Note that the Pt atoms are not eclipsed and that neither Pt∘∘∘Pt distance is < 3.5 Å. The perpendicular separation between the mean planes through the trpy ligand non-hydrogen atoms of successive cations is ~ 3.4 Å.[18]

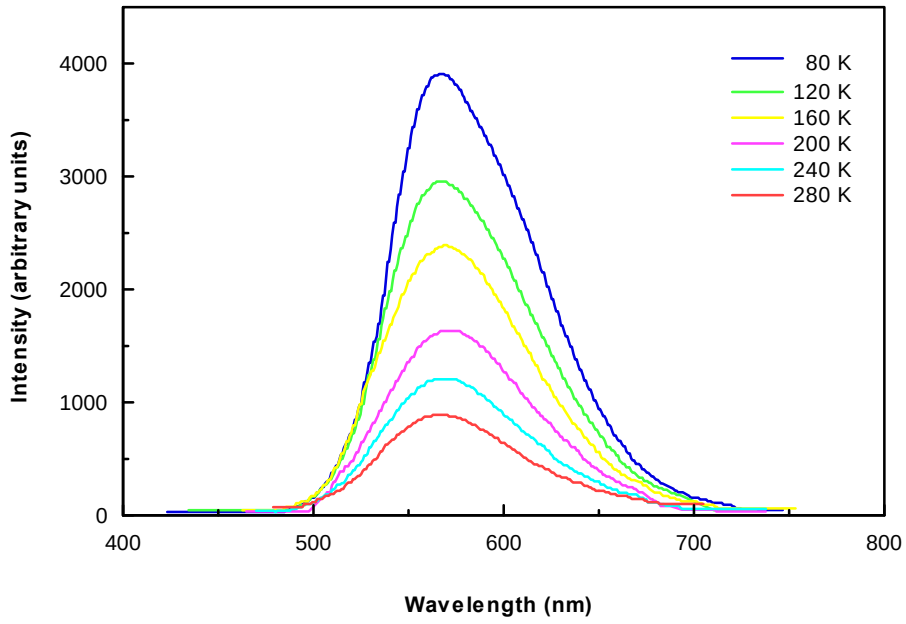

Figure 1.9 Solid state emission spectrum of [Pt{4'-(*o*-$CH_3C_6H_4$)trpy}Cl]BF_4 recorded at 40 K intervals from 80-280 K.[18]

As illustrated in Figure 1.8, successive cations in the stack adopt a head-to-tail conformation and are laterally displaced with respect to a line drawn through one platinum atom and perpendicular to the mean plane through the atoms comprising the trpy moiety. Thus, the offset π-stacked geometry predicted for favourable π(trpy)-π(trpy) interactions is adopted. Note too that the interplanar separations are ~ 3.4 Å, the value expected for net attractive π-σ electrostatic forces between two cations.[49,50]

Turning to the emission data in Figure 1.9, we see that the 280 K spectrum consists of a broad band that is asymmetric but devoid of any vibrational structure. On lowering the temperature of the sample there is the expected systematic increase in intensity, which is accompanied by a slight narrowing of the band, but no shift in the position of the emission maximum ($\lambda_{em}{}^{max}$). Before discussing how emission of this kind is obtained, it is important to note that the [Pt{4-(*o*-$CH_3C_6H_4$)trpy}Cl]$^+$ cation exhibits monomeric ^{3}MLCT emission in a dilute glass; moreover the ^{3}MLCT emission occurs at a considerably higher energy.[18]

There are a number of examples of complexes of platinum(II) with planar aromatic ligands that exhibit broad, unstructured and relatively low energy emission in the solid state.[12,15,16,18,23,24,34,52-57] Early examples are the yellow compound $[Pt(phen)Cl_2]\cdot 3H_2O$ (phen = 1,10-phenantroline) studied by Miskowski and Houlding;[52] and the orange (Cl^-, ClO_4^-, $CF_3SO_3^-$) and yellow (PF_6^-) salts of the $[Pt(trpy)Cl]^+$ cation studied by Gray and co-workers.[12] They assign the luminescence to an "excimeric intraligand transition resulting from π(trpy)-π(trpy) interactions", a quote from the Gray paper.[12] Their assignment, as well as those by subsequent workers,[12,15,16,18,23,24,34,52-55] follow from studies of the photoluminescence of planar, organic aromatic molecules in fluid solution.[56,57] These studies will now be discussed before returning to a discussion of excimer emission in the solid state by ionic platinum terpyridines.

When a solution of planar, organic aromatic molecules (X) is irradiated with ultraviolet radiation a π-π* absorption occurs and the molecule enters its excited form (X*). The excited molecule (X*) then associates with a molecule in its ground state to form an excited state dimer (X_2*); hence the name "excimer". It is important to note that there is no significant ground state interaction, but rather that the lowest energy excitation (π-π*) results in a new excited state which is overall bonding between the two aromatic systems. The organic excimer loses energy either by returning to the respective ground and excited state monomers or by emitting light to form a ground state dimer (X_2). The ground state dimer then dissociates back to the ground state monomers (X + X): see Scheme 1.2.

$$X^* + X \leftrightarrow X_2^* \xrightarrow{h\nu} X_2 \rightarrow X + X$$

Scheme 1.2 Molecular processes involved in excimer formation and dissociation.[53]

Of particular significance is that the equilibrium geometry in the excimer is very different to that of the ground state monomer, i.e. the potential energy surfaces for the ground and excited states are mismatched. It is this difference that produces the broad, poorly

structured and red-shifted emission that has been taken as an experimental manifestation of excimer formation.[12,52] For a more complete discussion of excimer emission, including plots of potential energy surfaces, the reader is referred to the work of Yip and Levy.[58]

Authors such as Miskowski and Gray have assumed that the above mechanism for organic excimer emission can be used to explain the broad, essentially featureless, red-shifted emission measured in the solid state for complexes of platinum(II) with planar organic aromatic ligands.[12,52] We examine here whether this is feasible, in particular with respect to terpyridyl ligand complexes of platinum(II), where π(trpy)-π(trpy) interactions are present in the solid state. Unlike for purely organic systems, the primary excitation must involve, as discussed above, the promotion of an electron from the atomic platinum d-orbital into the π*-LUMO of the organic ligand, i.e. the excitation is d(Pt)-π*(trpy). The reduced (formally negatively charged) trpy moiety should show a stronger π(trpy)-σ(trpy) electrostatic attraction than the trpy moiety in its ground state, assuming that adjacent cations are not excited simultaneously. Given the strong attraction, it can be argued that excited state dimers (excimers) do indeed form on excitation of the solid. Excimer emission will then be observed.

Thus we conclude: the emission recorded in the solid state for [Pt{4-(*o*-$CH_3C_6H_4$)trpy}Cl]BF_4 is correctly assigned as excimeric in origin. Note that excimer emission in the solid state is made possible precisely because, the cations (specifically the trpy moieties) are pre-assembled according to the geometrical constraints imposed by the need for stabilising π(trpy)-π(trpy) interactions. However, see the cautionary note in the next section.

1.3.3 Emission by monomers in the solid state

We start with an example. The emission spectra recorded at 40 K intervals from 80-280 K on the yellow compound [Pt{4'-(Ph)trpy}(CN)]CF_3SO_3 are shown in Figure 1.10. At 280 K the spectrum consists of a vibronically structured band with three components centered at 520 (0-0 transition), 555 (0-1 transition) and 600 nm (0-2 transition).

Lowering the temperature results in the expected increase in the peak intensities but with no shift in the position of the emission maximum.[24] The monotonic decrease in the intensities of the vibrational components with increasing wavelength is typical of monomeric ^{3}MLCT emission. Moreover, the vibrational spacings of ~ 1200 cm^{-1} are typical of the C─C and C─N stretching motions of the terpyridine framework. The spectrum is red-shifted by ~ 30 nm as compared to the ^{3}MLCT emission recorded for the [Pt{4'-(Ph)trpy}(CN)]$^+$ cation in dichloromethane.[24] In all respects the luminescence is typical of emission from an isolated monomer; the small red-shift is probably simply due to the change in environment in going from a dichloromethane solution to the solid state.

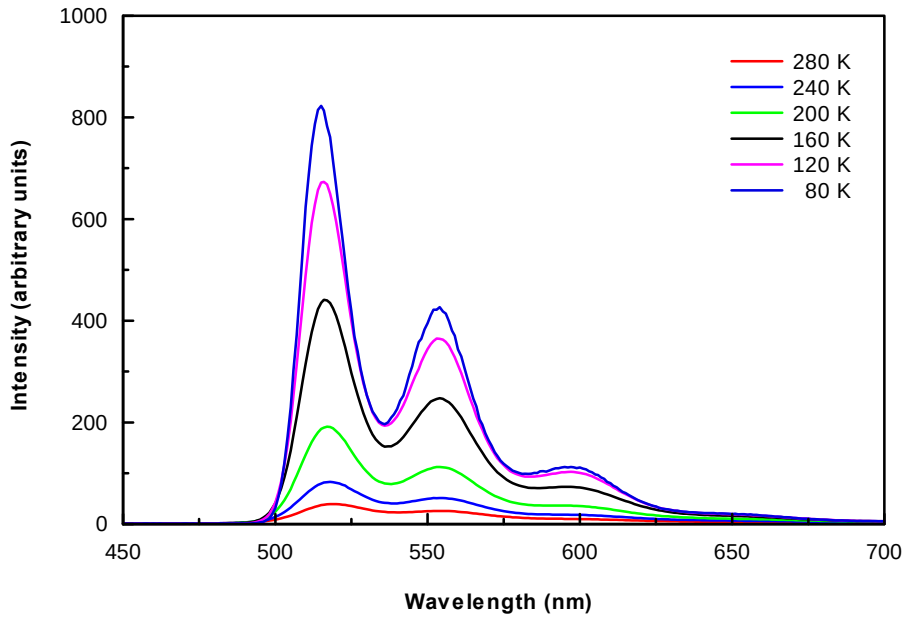

Figure 1.10 Solid state emission spectra of [Pt{4'-(Ph)trpy}(CN)]CF_3SO_3 recorded at 40 K intervals from 80-280 K.[24]

An X-ray crystal structure determination of [Pt{4'-(Ph)trpy}(CN)]CF_3SO_3 has not been done. However, given the yellow colour it would be extremely surprising if some form of stabilising π(trpy)-π(trpy) interactions were not present in the solid: this invites the question: "why do we not observe excimer emission for [Pt{4'-(Ph)trpy}(CN)]CF_3SO_3?". In the absence of structural data we do not have a definitive answer but the following explanation is plausible.

We need to return to the conditions required for excimer formation. A monomer (in this case a cation) in its excited state (X*) must combine with a monomer in its ground state (X) to form an excited state dimer (X_2*). As noted by Yip and Levy, this process involves surmounting a potential energy barrier.[58] Presumably the size of this barrier depends on the precise degree of pre-organisation of adjacent monomers in the solid state. It could be that in the case of [Pt{4'-(Ph)trpy}(CN)]CF_3SO_3, the juxtaposition of the cations is such that on irradiation of the sample insufficient internal energy is available to surmount the potential energy barrier: excimers do not form and monomer, rather than excimer, emission is observed. As previously noted, a number of relative orientations of the cations are possible for ionic platinum terpyridines. Perhaps not all of these predispose the cations to excimer formation. Other factors may also play a role such as the steric demands of the substituent in the 4'-position of the terpyridyl ligand.

In conclusion: monomer emission can and does occur in the solid state. Clearly, more work is required, especially in respect of crystal structure determinations, to establish the kind of emission expected in the solid state for an ionic platinum terpyridine.

2 Platinum terpyridines (and bipyridines) with the SCN^- ion as co-ligand

Only two previous reports address the photophysical properties of an ionic platinum terpyridine with the ambidentate SCN^- ion as the co-ligand. The first was by Che and co-workers in 1993 on the complex [Pt(trpy)(NCS)]PF_6.[23] The compound is red, non-emissive in acetonitrile, but reported as strongly emissive in the solid state with an emission lifetime of 0.4 μs; no further details are provided.[23] Subsequently, in 1994, McMillin and co-workers reported on the complex [Pt(trpy)(NCS)]$BF_4 \cdot H_2O$.[13,22] In this report the authors note that the complex emits weakly in acetonitrile (Φ = 0.000094) but more strongly in the non-coordinating solvent, dichloromethane (DCM). The emission maximises at ~ 590 nm in both solvents and is assigned to a ^{3}d-π* excited state, i.e.

^{3}MLCT emission is observed which is typical of ionic platinum terpyridines when a weak field co-ligand is bound to the platinum. Moreover, the MLCT absorption bands measured for $[Pt(trpy)(NCS)]BF_4 \cdot H_2O$ in acetonitrile occur at essentially the same wavelengths as those reported by McMillin for $[Pt(trpy)Cl]^+$ in the same solvent.[13,22] Thus the implication is that the SCN^- ion is bound to the platinum atom through the sulfur atom in fluid solution, at least for the $[Pt(trpy)(NCS)]^+$ cation. However, this has not been confirmed, e.g. by ^{15}N NMR spectroscopic studies. Nor has a single crystal structure determination been reported of an ionic platinum terpyridine with the SCN^- ion as the co-ligand, adding to the uncertainty with regard to its mode of coordination in compounds of this type.

In contrast there are examples in the literature of both the N- and S-bound SCN^- ion in bypyridyl ligand complexes of platinum(II).[48,55,59-64] A good example is the X-ray crystal structure determinations of the complexes $[Pt(bipy)(SCN)_2]$[64] and $[Pt(bipy)(NCS)_2]$[48,64] where bipy = 2,2'-bipyridine. In the former compound, the SCN^- ions are S-bound as the thiocyanate ligand and in the latter compound they are N-bound as the isothiocyanate ligand; note that the S-bound isomer is yellow while the N-bound isomer is red.[48,64] The crystal structure determination of $[Pt(bipy)(SCN)_2]$ shows that coordination through the S atom affords a bent geometry, i.e. the Pt─S─C bond angle is 103 ° and the thiocyanate ligands bend out of the Pt(bipy) plane.[64] On the other hand the isothiocyanate ligands in $[Pt(bipy)(NCS)_2]$ bond through the nitrogen atom with an essentially linear sequence of atoms, i.e. the Pt─N─C bond angle is ~ 180 °, as is the N─C─S angle.[48,64] The upshot of this is that the "rod-like" coordination of the isothiocyanate ligand allows the complexes to parallel stack in a manner which facilitates the formation of potentially stabilising intermolecular d_z^2(Pt)-d_z^2(Pt) orbital and/or π(trpy)- π(trpy) interactions in the solid state.[48] Thus, the N-bound isomer is expected to be the thermodynamically more stable form, at least in the solid state. Indeed both Connick and co-workers and Kato and co-workers, report that the S-bound complex $[Pt(bipy)(SCN)_2]$ isomerises in the solid state to the N-bound isomer, $[Pt(bipy)(NCS)_2]$, whilst the reverse process has never been observed.[48,64] Coyer and co-workers have also drawn the same conclusion, claiming that the N-bound isomer is the thermodynamically more stable form in the solid state

structures of bypyridyl ligand complexes of platinum(II).[63] Certainly, it is clear that if the SCN^- ion is S-bound and the ligand protrudes out of the plane of the Pt(bipy/trpy) moiety, stabilising Pt◦◦◦Pt interactions will not be possible because of steric repulsions between the thiocyanate ligands attached to adjacent complexes. The situation in solution is far less clear; whether the S- or N-bound linkage isomer is present will depend on the relative strengths of the Pt─SCN and Pt─NCS bonds; and this, in turn, will depend on the electron density or degree of hardness/softness at the Pt centre; which is determined in part, by the electronic effects of the ligands.[62,66] (A full description of the different bonding models for the S- and N-bound ligands is given in ref. 66.) In fact, previous reports on iso/thiocyanate ligand complexes in general, indicate that both isomers often co-exist in equilibrium in solution;[48,59-64] and that factors such as the polarity of the solvent play a role in determining the relative stabilities of the two linkage isomers in solution.[64,67-69]

Finally, we recognise that the SCN^- ion can act as a bridging ligand between two metal centres.[61,62,70] However, the most fundamental ligations for the SCN^- ion are the terminal M─SCN and M─NCS modes; and only these two possibilities are relevant to the work in this thesis.

3 Aims of the project

Previous research in our laboratories has focused on the development of ionic platinum terpyridines as optical sensor materials. For this reason we are mainly interested in the solid state photoluminescent properties of new ionic platinum terpyridines with isothiocyanate as the co-ligand; isothiocyanate rather than thiocyanate, since the SCN^- ion is shown in this work to invariably bind to the platinum atom through the N atom in the solid state.

Note: throughout the following chapters, the formula of the mononuclear complex containing the SCN^- ion as a ligand is always written with the ligand atoms in brackets in

the sequence "NCS". We do this for consistency reasons. Whether the ion is actually S-bound or N-bound will be apparent in the context of the discussion.

Given the above background the aims of the project were:

- To synthesise a salt of the $[Pt(trpy)(NCS)]^+$ cation that is different to those reported previously; in particular the hexafluoroantimonate salt $[Pt(trpy)(NCS)]SbF_6$ (**1**). Noting that changing the anion will have an effect on the crystal structure of the salt, we wished to investigate the solid state photophysical properties of the compound and to clarify, if possible, the mode of coordination of the ambidentate SCN^- ion, both in solution and in the solid state.

- To introduce a phenyl substituent in the 4'-position of the trpy ligand that will influence the energy of the π*-LUMO and, possibly, play a role in how the cations pack in the solid state. To this end, we planned to synthesise $[Pt\{4'\text{-}(Ph)trpy\}(NCS)]SbF_6$, (**2**) and to investigate its photophysical properties, in particular in the solid state. As for compound **1**, we also hoped to clarify the mode of coordination of the SCN^- ion, both in solution and in the solid state.

As it turns out, compounds **1** and **2** have been successfully synthesised, but not without complications that influence the photophysical properties of the material. Indeed, compounds **1** and **2** possess physical properties that one would not have predicted. What is consistent is that the SCN^- ion binds to the platinum atom through the N atom in the solid state. However the same is not true in fluid solution, as will be discussed.

2 Synthesis, characterisation and photophysical properties of $[Pt(trpy)(NCS)]SbF_6$ (compound 1)

1 Preliminary considerations

As will be shown later in this chapter $[Pt(trpy)(NCS)]SbF_6$ (**1**), which is maroon in colour, is both thermochromic and vapochromic, i.e. the compound changes colour on heating (or cooling) and on exposure to certain solvent vapours. This has prompted us to introduce the following labelling scheme for the various solids that have been isolated:

G – green
M – maroon
O – orange
R – red
Y – yellow

Thus:
1─R ≡ red $[Pt(trpy)(NCS)]SbF_6$
1·CH_3CN─Y ≡ yellow $[Pt(trpy)(NCS)]SbF_6 \cdot CH_3CN$.

An introduction to thermochromic and vapochromic materials is given in context, later in this chapter: see Sections 5.3.1 and 5.5.1 respectively.

2 Synthesis and characterisation

The key step of the synthesis follows a method slightly modified to that employed by Ledwaba and co-workers for the synthesis of cyanide ion derivatives of platinum terpyridines.[15,24,33] This is a metathesis reaction in which [Pt(trpy)Cl]SbF_6 is treated with a 10% molar excess of AgSCN in refluxing acetonitrile under an inert atmosphere of nitrogen for 24 hours: see Scheme 2.1.

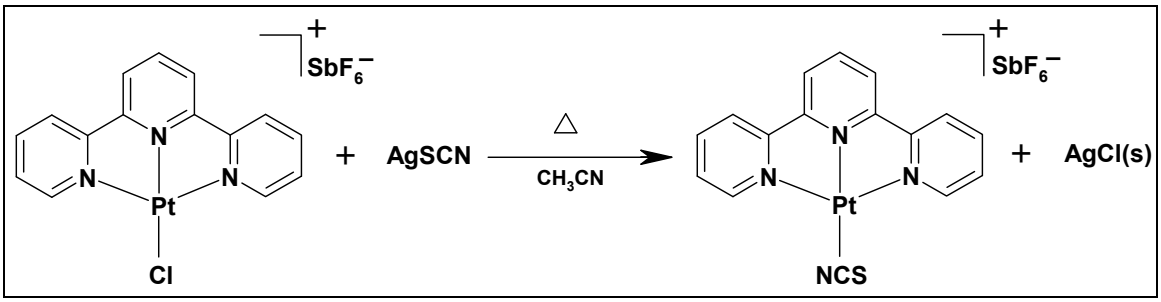

Scheme 2.1 Illustration of the method used for the synthesis of [Pt(trpy)(NCS)]SbF_6 (**1**).

The AgCl precipitate is removed by cannular filtration, and the solution of **1** is concentrated to near saturation by removal of the solvent *in vacuo*. Slow diffusion of diethyl ether into the above solution induces precipitation of yellow crystals of **1·CH$_3$CN─Y**, whose crystal structure has been determined by means of single crystal X-ray diffraction as described in Section 4 of this chapter; however, when the mother liquor (acetonitrile) is removed by decantation, **1·CH$_3$CN─Y** rapidly (< 2 min) transforms into a maroon desolvated form *viz.* **1─M**. This is obtained as a pure microcrystalline material after washing with ice-cold acetonitrile and diethyl ether and drying *in vacuo*.

The empirical formulation of [Pt(trpy)(NCS)]SbF_6, i.e. $C_{16}H_{11}N_4F_6PtSSb$ was confirmed by means of elemental analysis for %C, H and N. The infrared spectrum recorded as a KBr pellet exhibits a strong, sharp peak at 2097 cm^{-1} assigned to the ν(SC≡N) stretching mode and a weaker, somewhat broader peak at 874 cm^{-1}, due to the ν(NC−S) stretching mode. [The relevance of the ν(SC≡N) and ν(NC−S) stretching frequencies to the mode of

coordination of the SCN^- ion is well documented.[60-63] We simply note here that the values recorded for **1—M** are consistent with the N-bound isomer being present in solid state.] Other peaks in the infrared spectrum are common to platinum(II) terpyridines, in particular peaks between 1610 and 880 cm^{-1}, the "fingerprint" region for the trpy ligand.[34] The various infrared stretching frequencies and their assignments are listed in Section 3.1 of Chapter 4. A ^1H NMR spectrum of **1—M** was recorded in CD_3CN where the signals where sufficiently well resolved to assign the resonances: GHSQC and GHMQC NMR experiments where performed to aid in the assignment of the peaks. The various proton resonances and their assignments are also listed in Section 3.1 of Chapter 4. Note that these are listed only for the N-bound isomer that dominates in CD_3CN: see the discussion in the next section where we describe the ^{13}C and ^{15}N NMR spectra of the "$Pt^{15}N^{13}CS$" unit obtained by using a labelled ^{13}C and ^{15}N enriched sample of **1—M**, i.e. $[Pt(trpy)(^{15}N^{13}CS)]SbF_6$. The ^{13}C and ^{15}N resonances and their assignments listed in Section 3.2 of this chapter were obtained using this sample. Mass spectrometry has been performed on **1—M**, the results of which are in excellent agreement with the isotopic predictions, showing a $[Pt(trpy)(NCS)]^{2+}$ peak at m/z = 486.0365. Finally, we also list in Section 3.1 of Chapter 4 the UV/vis absorption data measured for $[Pt(trpy)(NCS)]SbF_6$ in acetonitrile; these data are in full agreement with the absorption spectral data reported previously for the $[Pt(trpy)(NCS)]^+$ cation in acetonitrile.[13,22,23]

3 Speciation of $[Pt(trpy)(NCS)]^+$ in fluid solution

3.1 Introduction

The SCN^- ion is one of the best documented examples of an ambidentate ligand. There have been numerous studies that show that it can either bind to a metal through the S atom as the thiocyanate ligand, or through the N atom as the isothiocyanate ligand.[48,59-64] These studies have been made both in solution and in the solid state but, of interest in this section, is the mode of coordination of the SCN^- ion in $[Pt(trpy)(NCS)]^+$ in fluid solution, specifically in an acetonitrile solution of $[Pt(trpy)(NCS)]SbF_6$ (**1**). Acetonitrile is the solvent of interest since the compound was synthesised in this solvent and the single

crystals of **1·CH$_3$CN─Y** used for the X-ray analysis were grown from acetonitrile: see Section 4 that follows for a description of the crystal structure of **1·CH$_3$CN─Y**. However, it is important to note that the mode of coordination of the SCN^- ion in solution has been shown to be dependent on the polarity of the solvent;[67-69] and that the results we describe below for acetonitrile cannot be automatically transferred to other solvents. Also true is that often *both* linkage isomers co-exist in equilibrium in solution; see, for example, the work by Burmeister.[61,62] In this regard we note that the ^{1}H NMR spectrum recorded for **1** in CD_3CN at room temperature shows a set of signals easily assigned to the protons of the trpy ligand; but that each (major) peak in the spectrum is "shadowed" by a less intense satellite peak: see Section 3.1 of Chapter 4 for a listing of the ^{1}H NMR resonances of the dominant species in solution and their assignments. Indeed, it was this observation that prompted us to investigate further the speciation of **1** in acetonitrile; our suspicion was that both the S-bound and N-bound isomer co-existed in acetonitrile, and that one isomer was dominant.

A literature search showed that by far the most useful technique for establishing the mode of coordination of the SCN^- ion in solution is NMR spectroscopy, in particular the ^{13}C and ^{15}N NMR spectroscopy of the coordinated SCN^- ion.[63,70-73] Both nuclei possess a nuclear spin of one-half, making the interpretation of the ^{13}C and ^{15}N NMR spectra of a SCN^- ion complex relatively simple – at least in principle. The problem is, of course, that carbon-13 and nitrogen-15 both have low natural abundances of 1.1 and 0.37% respectively. For this reason, we synthesised (and purified) the isotopically labelled compound, $[Pt(trpy)(^{15}N^{13}CS)]SbF_6$. The same methods were used as for the unlabelled compound, except that $AgS^{13}C^{15}N$ was used in the metathesis reaction; note that the $AgS^{13}C^{15}N$ was obtained from $KS^{13}C^{15}N$, and the latter was supplied by Isochem with the carbon-13 and nitrogen-15 present in > 99% abundance: see Section 1.2 of Chapter 4. An infrared spectrum of $[Pt(trpy)(^{15}N^{13}CS)]SbF_6$ has been recorded in a KBr pellet. The $\nu[S^{13}C{\equiv}^{15}N]$ stretching frequency of 2015 cm^{-1} shows the expected isotopic shift to lower frequency as compared to the ν[SC≡N] value of 2097 cm^{-1} recorded for the unlabelled compound. The expected isotopic shift is also manifest in a $\nu[S–^{13}C^{15}N]$ stretching frequency of 851 cm^{-1} that is ~ 20 cm^{-1} lower in energy than that recorded for the parent

compound: see Section 3.1 of Chapter 4. These infrared data served to confirm that a complex with the isotopically labelled $S^{13}C^{15}N^-$ ion as co-ligand had been successfully synthesised; indeed, a close inspection of the infrared spectrum showed no evidence for a peak at ~ 2100 cm^{-1} that could be assigned to a ν[SC≡N] stretching mode.

We finally note that the nitrogen-15 nucleus has a sensitivity that is about 15 fold less than that for carbon-13. This leads to problems in obtaining good signal-to-noise ratios in a ^{15}N NMR spectrum, problems that have compromised the quality of the ^{15}N NMR spectra that we have recorded using our in-house 500 MHz Bruker Avance III spectrometer. However, we were able to obtain one ^{15}N NMR spectrum with an exceptionally good signal-to-noise ratio that was measured with the quadnuclear cold probe and 600 MHz NMR spectrometer located at the Bruker R&D headquarters in Karlsruhe: see the up-field spectrum in Figure 2.2 below. Indeed, this is the definitive spectrum that allows for a reliable interpretation of the ^{13}C and ^{15}N NMR data, and a consequent conclusion regarding the speciation of $[Pt(trpy)(NCS)]^+$ in acetonitrile solution.

3.2 ^{13}C and ^{15}N NMR studies of the "$Pt^{15}N^{13}CS$" unit in $[Pt(trpy)(^{15}N^{13}CS)]^+$

We start with the ^{13}C NMR spectrum shown in Figure 2.1; the ^{13}C rather than the ^{15}N spectrum was chosen as the departure point for the discussion, because all the peaks expected in the spectrum can be observed experimentally; as a result of the relatively good signal-to-noise ratios obtained with our in-house spectrometer. As shown in Figure 2.1 two groups of signals are observed, both of which originate from the "$Pt^{15}N^{13}CS$" unit. One is downfield and centred at δ 135.2 and the other up-field and centred at δ 116.7; the former signal is much more intense than the latter. The overall splitting pattern for both signals is the same *viz.* a doublet together with a doublet of doublets. The ratio of the integrated intensity for the doublet to that for the doublet of doublets is also the same for both signals, i.e. ~ 2:1. Interpretation of the splitting pattern is as follows. The ^{13}C nucleus (I = ½) couples in the first instance to the ^{15}N (I = ½) nucleus to which it is

bonded, giving rise to the doublet. Further splitting of the doublet to give a doublet of doublets occurs if the $S^{13}C^{15}N^-$ ion is bonded to a NMR active ^{195}Pt nucleus with a nuclear spin of $I = ½$; note that this is ^2J coupling since the ^{13}C would be linked to the ^{195}Pt through two bonds. Also note that the natural abundance of the ^{195}Pt isotope is 33.8%, and thus only about one-third of the $S^{13}C^{15}N^-$ ions experience spin-spin coupling to the ^{195}Pt nucleus; hence the intensity ratio of ~ 2:1 for the doublet to the doublet of doublets.

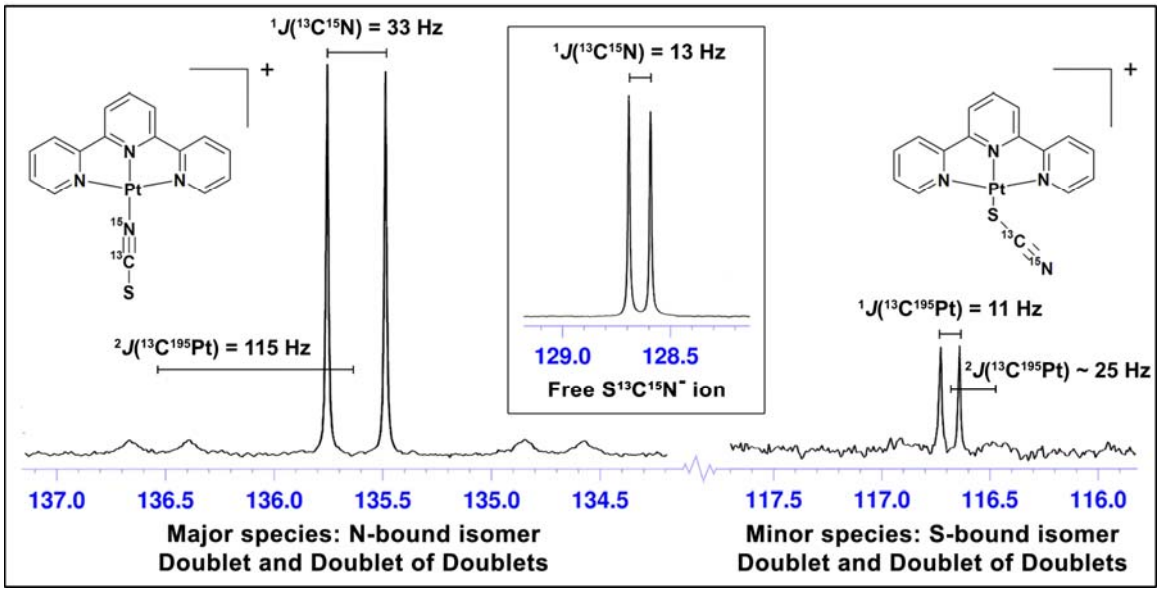

Figure 2.1 ^{13}C NMR signals showing the chemical shifts (ppm) and coupling constants (Hz) of the "$Pt^{15}N^{13}CS$" unit of $[Pt(trpy)(^{15}N^{13}CS)]^+$ recorded in CD_3CN. Also shown (in the insert) is the ^{13}C NMR signal of the free SCN^- ion recorded in CD_3CN doped with ammonia: see text. The spectra where recorded at 303 K and referenced to CD_3CN.

One immediate conclusion can be drawn: the $S^{13}C^{15}N^-$ ion must be bonded to a Pt atom in order for coupling to ^{195}Pt to occur, i.e. in an acetonitrile solution of $[Pt(trpy)(NCS)]SbF_6$ (**1**) the SCN^- ion is not free, but genuinely bonded as a ligand to the Pt atom. A second conclusion that follows from the ^{13}C NMR spectrum shown in Figure 2.1 is that *two* SCN^- ion bonded species must be present in solution, and that one species dominates over the other. A comparison of the integrated intensities of the signals at

δ 135.2 and δ 116.7 suggests that ~ 95 % of the $[Pt(trpy)(NCS)]^+$ is present as the major species and ~ 5 % as the minor species.

Clearly, the implication of the analysis so far is that that the two species present in acetonitrile solutions of **1** are the S-bound and N-bound isomers of the SCN^- ion. We now examine to what extent the ^{13}C NMR data can help decide which of these two isomers is dominant. The overall splitting patterns do not help since they will be the same for both isomers. However, the chemical shifts are sufficiently different for the two signals to allow for a tentative conclusion. To aid interpretations based on chemical shifts we have recorded the ^{13}C NMR spectrum of the labelled silver salt, $AgS^{13}C^{15}N$: see the insert to Figure 2.1. This salt is not soluble in acetonitrile, but does dissolve when a few drops of ammonia solution are added to the NMR sample tube. Of course, dissolution of the salt proceeds due to the formation of the $Ag(NH_3)_2^+$ complex cation: more important is that the SCN^- ion is now present in solution as the free ion, i.e. it is not bonded to the Ag^+ cation. The ^{13}C spectrum in the insert is, as expected, a doublet; however the chemical shift of δ 128.6 constitutes new information, in particular it provides a useful value to which the chemical shifts of the two species can be referenced. (We note in parentheses that other workers have used the same approach when using ^{13}C and ^{15}N NMR spectroscopy to deduce the mode of coordination of the SCN^- ion in fluid solution: see refs 63,70-73.) There is a downfield shift to δ 135.2 of the chemical shift for the major isomer and an upfield shift to δ 116.7 for the chemical shift of the minor isomer. Clearly, the carbon-13 nucleus of the major isomer is *de-shielded* relative to the free SCN^- ion; on the other hand the carbon-13 nucleus of the minor isomer is *shielded* relative to the free SCN^- ion. This observation is consistent with the major isomer being N-bound. We say this because it is well established that π-lone pair donation through the N atom into a metal orbital is stronger than the π-lone pair donation of a bonded S atom: indeed, that is why N is classified as a hard donor and S as a soft donor atom.[65,66] Strong lone pair donation by the N atom will inevitably lead to a significant de-shielding of the carbon-13 nucleus of the coordinated $S^{13}C^{15}N^-$ ion, and this effect will be more marked than when the S atom is directly linked to the metal atom. In fact, the S-bound thiocyanate ligand is classified not only as a weak π-donor, but also as a *strong*

π-acceptor ligand.[66] This being the case, coordination *via* the S atom should result in increased *shielding* of the carbon-13 nucleus and an *upfield* shift of the carbon-13 resonance relative to that of the free ion – exactly as is observed. Thus, evidence based on chemical shifts suggests (but does not prove) that the dominant linkage isomer present in acetonitrile solutions of **1** is the N-bound isothiocyanate ligand.

Before proceeding we extract further information from the ^{13}C spectrum shown in Figure 2.1 that will aid in the interpretation of the ^{15}N NMR spectrum discussed next. These are the values of the $^1J(^{13}C^{15}N)$ coupling constants *viz.* 33 Hz for the major isomer and 11 Hz for the minor isomer. Note that the difference in the same coupling constant for the two isomers is not unexpected: this has to do with the different use of orbitals and strength of binding to platinum of the thiocyanate and isothiocyanate ligands.[66] (We note in parentheses that coupling constants can be calculated using density functional theory; this is planned with a view to determining how the $^1J(^{13}C^{15}N)$ coupling constant depends on the mode of coordination of the SCN^- ion.) Of course, the expectation is that similar values for the $^1J(^{13}C^{15}N)$ coupling constants should be obtained from the analysis of the ^{15}N NMR spectrum, i.e. we should expect that the $^1J(^{13}C^{15}N)$ coupling constant is ~ 33 Hz for the major isomer and ~ 11 Hz for the minor isomer; preferably, where the identification of the isomers is made independently of the ^{13}C NMR analysis.

The ^{15}N NMR spectra are shown in Figure 2.2. The upfield spectrum centred at δ 101.6 was recorded using the Bruker quadnuclear cold probe 600 MHz NMR spectrometer; as shown in the figure it comprises a relatively intense doublet together with a much weaker doublet of doublets. The same spectrum was also recorded on our in-house spectrometer but the signal-to-noise ratio was not high enough to discern the four small peaks belonging to the doublet of doublets. The downfield spectrum centred at δ 250.8 was recorded using our in-house spectrometer. The signal appears simply as a doublet whereas, as discussed below, it should comprise not only this doublet but also a doublet of doublets; that the doublet of doublets is not seen, is simply a problem of a poor signal-to-noise ratio. The first interpretative point we wish to make is that the upfield signal is far more intense than the downfield signal; and that the upfield signal must,

therefore, originate in the major isomer and that the downfield signal derives from the minor isomer. Clearly, the starting point for distinguishing between the 2 isomer signals is the upfield spectrum; after all it is only this spectrum that exhibits the full splitting pattern.

As already noted, the upfield ^{15}N NMR spectrum centred at δ 101.6 comprises a doublet and a doublet of doublets. With this information the interpretation of the splitting pattern is straightforward. The ^{15}N nucleus of the $S^{13}C^{15}N^-$ ion couples in the first instance to the carbon-13 nucleus to which it is bonded, giving rise to the doublet. Further coupling of the ^{15}N nucleus then occurs with the NMR active ^{195}Pt nucleus to give a doublet of doublets; of course this only applies if the $S^{13}C^{15}N^-$ ion is bonded to ^{195}Pt (rather than an NMR inactive Pt) in the first place. Given the natural abundance of the ^{195}Pt, the ratio of the integrated intensity for the doublet to that of the doublet of doublets should be ~ 2:1 – the observed ratio of 1:2.3 is in close agreement with the expected ratio.

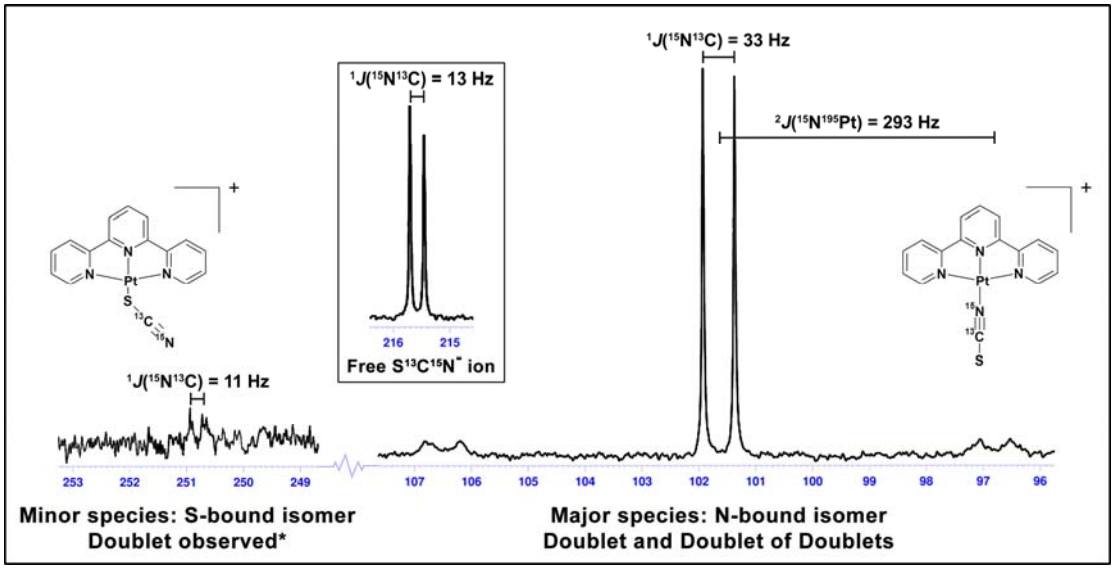

Figure 2.2 ^{15}N NMR signals showing the chemical shifts (ppm) and coupling constants (Hz) of the "$Pt^{15}N^{13}CS$" unit of $[Pt(trpy)(^{15}N^{13}CS)]^+$ recorded in CD_3CN. Also shown (in the insert) is the ^{15}N NMR signal of the free SCN^- ion recorded in CD_3CN doped with ammonia: see text. The ^{15}N NMR signal shown for the major species was recorded using a QNP cold probe and 600 MHz Bruker spectrometer, whilst that of the free $S^{13}C^{15}N^-$ ion and minor species where recorded using a standard 500 MHz Bruker Avance III spectrometer. The spectra where recorded at 303 K and referenced to ammonia (NH_3).

We now address the question of which isomer is the major one. In this regard, the key parameter is the coupling constant that quantifies the magnetic interaction between the ^{15}N nucleus and the ^{195}Pt nucleus. If the $S^{13}C^{15}N^-$ ion is N-bound the coupling is through one bond only, i.e. $^1J(^{15}N^{195}Pt)$. On the other hand, if it is S-bound the coupling interaction is through 3 bonds, i.e. $^3J(^{15}N^{195}Pt)$. The coupling constant is a measure of the strength of the magnetic interaction and, in general, is expected to be considerably greater for ^1J as compared to ^3J coupling. Thus, we should be able to distinguish between the 2 isomers on the basis of the coupling constant determined from the upfield spectrum shown in Figure 2.2: the value is 293 Hz. In fact, this is the most widely used method for establishing the mode of coordination of the SCN^- ion to a metal in fluid solution. The work of Pregosin and co-workers is most relevant in this regard.[72] They have used ^{15}N NMR spectroscopy to study the speciation of a wide range of complexes of platinum(II) that include the SCN^- ion as a ligand: the $^1J(^{15}N^{195}Pt)$ coupling constants that they report fall in the range 117-617 Hz, while the $^3J(^{15}N^{195}Pt)$ values fall in a narrower range of 12-22 Hz.[70-73] Their results make sense in that the ^1J coupling constants are large while the ^3J coupling constants are small. The conclusion that we must now draw is unequivocal: given a relatively large coupling constant of nearly 300 Hz the coupling of the ^{15}N to the ^{195}Pt nucleus must be through one bond only, i.e. $^1J(^{15}N^{195}Pt)$ coupling; and, therefore, the dominant isomer of $[Pt(trpy)(NCS)]^+$ present in acetonitrile must be the N-bound isomer. We now compare the $^1J(^{13}C^{15}N)$ coupling constants extracted from the ^{13}C and ^{15}N NMR signals for the major isomer; both are measured as 33 Hz. Such a good fit strongly supports the tentative assignment of the ^{13}C NMR signal at δ 135.2 to the dominant N-bound isomer.

We now turn our attention to the downfield signal observed at δ 250.8 in the ^{15}N NMR spectrum: see Figure 2.2. The signal comprises a doublet for which the coupling constant is measured as 11 Hz; again, note the fit with the $^1J(^{13}C^{15}N)$ coupling constant measured for the minor isomer in the ^{13}C NMR spectrum. Clearly, the doublet arises from the ^1J coupling of the nitrogen-15 to the carbon-13 nucleus. Further coupling to the ^{195}Pt is not observed because of the poor signal-to-noise ratio achievable with our in-house

spectrometer. More significant is that this signal is shifted downfield as compared to the upfield signal centred at δ 101.6. This is exactly the direction of shift that would be expected if the SCN^- ion changes from N-bound (where the bonded N atom will be heavily shielded by the Pt atom) to S-bound (where the N atom is pendant and experiences little of the magnetic field exerted by the Pt atom). For the sake of completeness we have included in the insert to Figure 2.2 the ^{15}N NMR spectrum of the free $S^{13}C^{15}N^-$ ion obtained as described above; a doublet is observed that is centred at δ 215.6. As expected the ^{15}N chemical shift of the free $S^{13}C^{15}N^-$ ion is closer to that for the S-bound isomer of δ 250.8 than to that for the N-bound isomer of δ 101.6. However, the downfield shift from δ 215.6 to δ 250.8 that occurs when the free ion binds to the Pt atom *via* the S atom is significant, and worthy of comment. The downfield shift implies that the pendant N atom is deshielded when the S atom binds to the metal atom *via* a lone pair in a π-orbital; in fact deshielding is anticipated if π-donation dominates. However, the S-bound thiocyanate ligand is classified as a weak π-donor and a *strong π-acceptor* ligand[66] and, this being the case, deshielding of the pendant N atom might *not* be anticipated. Clearly, we do not have a proper explanation; quantitative calculations are required of just how the electron density at the N atom changes when the SCN^- binds *via* the S atom to the metal centre in a terpyridyl ligand complex of platinum(II).

Finally, we report the results of a Heteronuclear Multiple Bond Coherence (HMBC) experiment that shows coupling between a proton on the trpy moiety and the ^{15}N atom of the "$Pt^{15}N^{13}CS$" unit. We assume that the proton is the hydrogen ($H_{6/6''}$) bonded to the C atom itself bonded to the N atom of an outer pyridine ring. Should this be the case, then the coupling to the ^{15}N would be through 4 bonds, i.e. $^4J(^1H^{15}N)$ for the major (N-bound) isomer. Were the major isomer S-bound, then the coupling would be through 6 bonds – a very unlikely scenario. Thus the HMBC experiment supports the above conclusion that the major isomer of $[Pt(trpy)(NCS)]^+$ is with the SCN^- ion N-bound as the isothiocyanate ligand – at least in acetonitrile solution.

In summary, the cumulative NMR evidence shows that the dominant linkage isomer present in acetonitrile solutions of $[Pt(trpy)(NCS)]SbF_6$ (**1**) is the N-bound isothiocyanate

ligand; but that a small amount (~ 5%) of the S-bound isomer co-exists in equilibrium with the N-bound isomer. We address the question of why this is the case in Section 3.3 of Chapter 3, i.e. once the mode of coordination of the SCN^- ion in acetonitrile solutions of [Pt{4'-(Ph)trpy}(NCS)]SbF_6 (**2**) has been discussed. Suffice to say at this stage is that the crystals of **1·CH_3CN–Y** that precipitate from acetonitrile solutions of compound **1** contain the SCN^- ion bonded to the Pt atom exclusively through the N-atom as the isothiocyanate ligand: see the description of the crystal structure of **1·CH_3CN–Y** in the next section.

4 Crystal structure of [Pt(trpy)(NCS)]SbF_6·CH_3CN (1·CH_3CN–Y)

Yellow plate-shaped single crystals of **1·CH_3CN–Y**, suitable for single crystal X-ray diffraction studies, were grown by slow diffusion of diethyl ether into a concentrated solution of **1** in acetonitrile. Since the crystals rapidly lose solvent (CH_3CN) to become a microcrystalline maroon powder, a single crystal was transferred within seconds from the mother liquor into an epoxy resin "ball" glued to the end of a glass capillary. Details of the X-ray crystallography are given in Section 8.2 and Table 4.1 of Chapter 4. Note that crystal structure determinations of **1·CH_3CN–Y** were made at room temperature (295 K) and at 100 K. However, we only discuss here the results of the crystal structure analysis performed using the 100 K intensity data. In this respect we note that the solid state emission spectrum for **1·CH_3CN–Y** was recorded at 77 K, since this solvate is non-emissive at room temperature; and thus the best interpretation of the emission spectrum will be in terms of the crystallographic information obtained at the lower temperature of 100 K. However, the structural details obtained at 295 K are not significantly different to those obtained at 100 K. There is no phase change when a single crystal of **1·CH_3CN–Y** is cooled from room temperature to 100 K, just the normal contraction of the unit cell dimensions: compare the data in **1MeCN295K.cif** and **1MeCN100K.cif** in the Supporting Information on the CD attached to the inside back cover of the thesis.

Figure 2.3 provides a perspective view of the cation as well as the atom labelling scheme. A list of the important interatomic distances and angles in the cation is given in Table 2.1. The coordination geometry of the central platinum atom is irregular square planar, as evident in N1─Pt─N2 and N2─Pt─N3 bond angles of 81.1(1) and 80.8(1)° respectively, as well as by a '*trans*' N1─Pt─N3 angle of 161.8(1)°. This is typical of terpyridyl ligand complexes of platinum(II) and arises from geometric constraints imposed by the tridentate ligand.[3,6,9,10,12,15,16,18,19,22-24,28,29,33-35] Also typical of such complexes is the shorter platinum to bridgehead nitrogen (N2) distance of 1.993(3) Å, as compared to the distances to the outer nitrogen atoms of 2.017(3) (N1) and 2.017(3) Å (N3).[3,6,9,10,12,15,16,18,19,22-24,28,29,33-35]

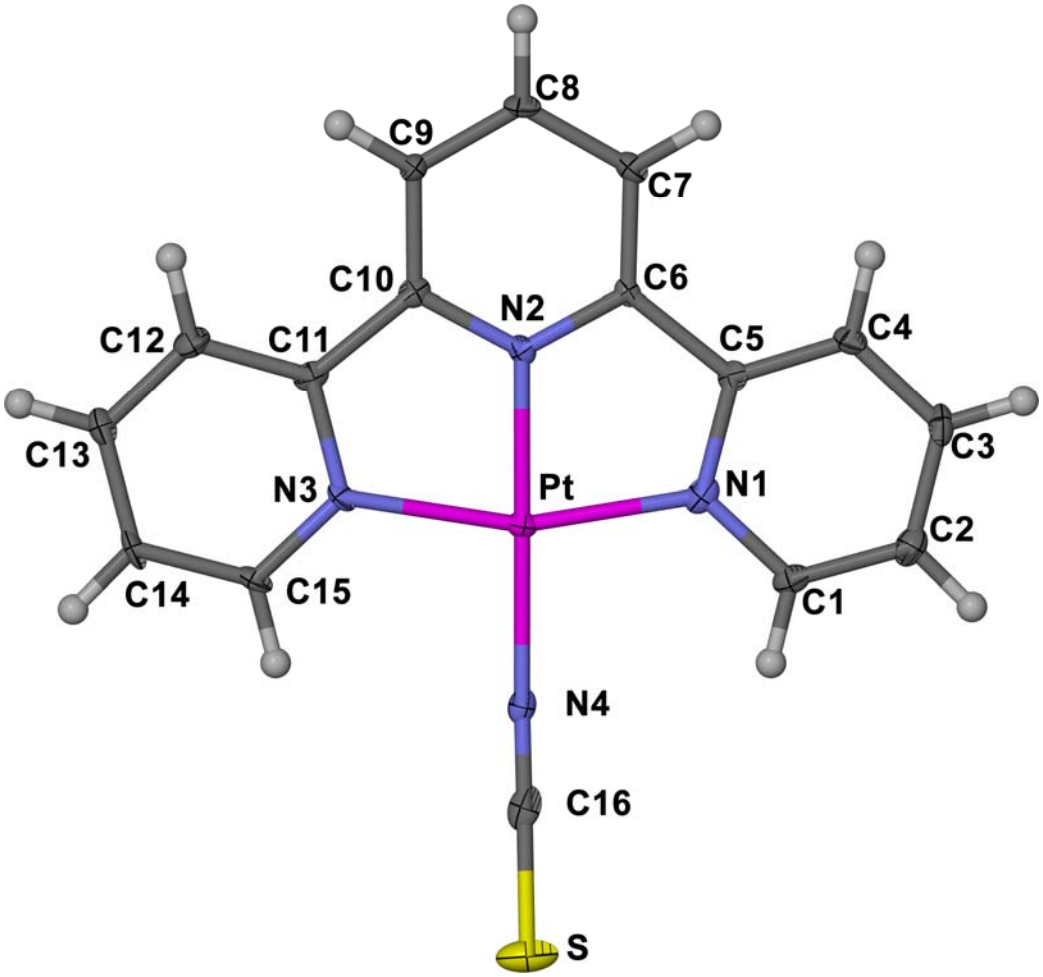

Figure 2.3 Frontal view of the cation in **1·CH_3CN─Y,** drawn using the 100 K intensity data. Thermal ellipsoids (50 %) are shown for all atoms except hydrogens which are shown as spheres of arbitrary radius.

Table 2.1 Selected interatomic distances and angles for the cation in **1·CH_3CN–Y** at 100 K

Distances (Å)		Angles (°)	
Pt─N1	2.017(3)	N1─Pt─N2	81.1(1)
Pt─N2	1.993(3)	N1─Pt─N3	161.8(1)
Pt─N3	2.017(2)	N1─Pt─N4	98.8(1)
Pt─N4	1.998(3)	N2─Pt─N3	80.8(1)
N4─C16	1.132(4)	N2─Pt─N4	179.9(1)
C16─S	1.627(4)	N3─Pt─N4	99.3(1)
		Pt─N4─C16	176.8(3)
		N4─C16─S	179.5(4)

The terpyridyl moiety is essentially planar with bond lengths and angles similar to those reported for other platinum terpyridine complexes.[3,6,9,10,12,15,16,18,19,22-24,28,29,33-35] The SCN^- ligand is N-bound as isothiocyanate and nearly linear with a Pt─N4─C16 angle of 176.8(3)° and a N4─C16─S angle of 179.5(4)°. Noteworthy is the fact that this is the first reported crystal structure of an ionic platinum terpyridine with the SCN^- ion as the co-ligand. Analysis of the crystal structures of other transition metal complexes containing the isothiocyanate ligand reveals that there is some variation in the M─N─C bond angle, with angles between 147 and 177° being reported; whilst the N─C─S bond angle is linear (or nearly linear) for the structures considered.[74-83] The N─C and C─S bond distances are similar to those reported for other transition metal compounds containing the isothiocyanate ion as co-ligand.[64,74-83] The Pt─N4 bond length of 1.998(3) Å is very similar to the Pt─NCS distances of 1.989(7) and 1.985(8) Å reported for [Pt(bipy)$(NCS)_2$].[64] The trpy moiety is slightly ruffled in the sense that with respect to a mean plane though the central pyridine ring, one of the outer pyridine rings lies slightly above this plane (C3 deviates by 0.20 Å from the plane) while the other outer pyridine ring lies slightly below this plane (C13 deviates by 0.36 Å from the same plane). However, these are small deviations as, indeed, are atom deviations from a mean plane drawn through all the non-hydrogen atoms comprising the cation. Thus, the cation as a whole is planar, at least to a first approximation. That this is the case has important

implications for the photophysical properties of the material that are discussed in subsequent sections.

We now address the question of how the $[Pt(trpy)(NCS)]^+$ cations, SbF_6^- anions and CH_3CN solvent molecules are arranged in the crystal, i.e. the crystal packing. A view down the [a]-axis of the contents of unit cell is given in Figure 2.4. Crystals of **1·CH_3CN─Y** contain discrete columns of cations that are stacked one on top of the next, i.e. parallel to each other. The spaces between the cation columns are filled by anions and solvent molecules that form separate columns of their own: see Figure 2.4.

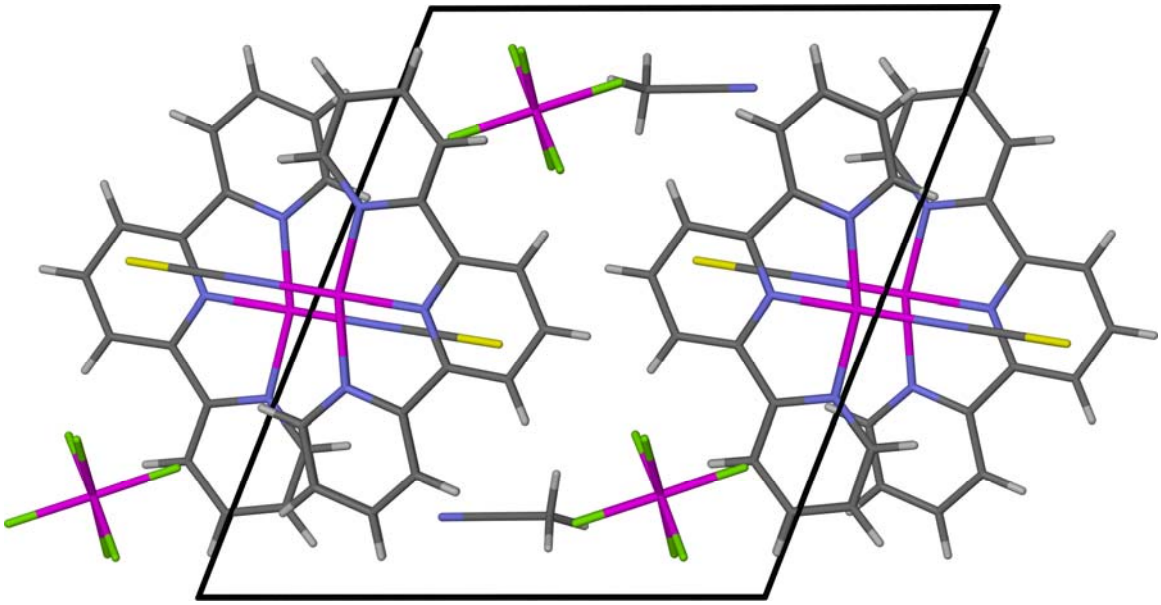

Figure 2.4 View of the unit cell contents projected down the [a]-axis that illustrates the cation, anion and solvent columns in **1·CH_3CN─Y.**

A side-on view of one stack of cations is given in Figure 2.5. Note that successive cations in the stack are linked through centres of inversion situated on the [a]-axis of the unit cell; thus successive cations in a stack lie perfectly head-to-tail. However, the cations are positioned with respect to the [a]-axis such that there are: (i) alternating short and long Pt∘∘∘Pt distances of 3.293 and 4.246 Å and (ii) a Pt∘∘∘Pt∘∘∘Pt "bond" angle of 146.3° that deviates substantially from 180°, resulting in a zig-zag arrangement of cations along a

stack. The Pt◦◦◦Pt distance of 3.293 Å is short enough to support effective d_{z^2}(Pt)-d_{z^2}(Pt) orbital overlap, but the value of 4.246 Å is longer than the upper distance limit of ~ 3.5 Å usually taken to indicate a d_{z^2}(Pt)-d_{z^2}(Pt) stabilising interaction.[47] Thus, the cation stack can be described as a series of well separated and offset dimers.

A more subtle structural feature of the cation stack is also evident from Figure 2.5. This is the direction of bending of the N4─C16─S bond angle. As shown in Figure 2.5, the S atom bends away from the intradimer space but (inevitably) into the interdimer space. Presumably the isothiocyanate ligand bends so as to minimise steric repulsions involving the large S atom and atoms of an adjacent cation. Certainly the shortest intermolecular non-bonded contacts involving the S atom and a carbon atom of a neighbouring trpy ligand (shown as the green dotted lines in Figure 2.5) are smaller than the sum of the van der Waals radii for a S and C atom of 3.5 Å.[84] There is also a nice correlation between the direction of bending and the area of overlap of adjacent cations, i.e. the isothiocyanate ligand bends towards the interdimer space for which there is less cation overlap, and thus less net steric repulsions: see Figure 2.5.

We now turn our attention to the extent and nature of the π(trpy)-π(trpy) stacking interactions along a cation stack. In this respect, the discussion in Section 1.3.2 of Chapter 1 refers. Figure 2.6 shows views perpendicular to the trpy mean planes for (A) the cation pair where the platinum atoms are linked by the shorter Pt◦◦◦Pt distance of 3.293 Å and (B) the cation pair where the platinum atoms are linked by the longer Pt◦◦◦Pt distance of 4.246 Å. The first parameters relevant to the existence of π(trpy)-π(trpy) stacking interactions are the interplanar spacings. As shown in Figure 2.4 these are ~ 3.3 Å, values well within the limit of 3.8 Å usually set for finite π-π interactions in organic species.[49,50] Of course the geometry of the trpy-trpy overlap is important to whether the π(trpy)-π(trpy) stacking interactions are net stabilising or not. As shown in Figure 2.6(B) the trpy ligands of the cations linked by the longer Pt◦◦◦Pt distance simply do not overlap at all: clearly π(trpy)-π(trpy) stacking interactions do not exist between these two cations.

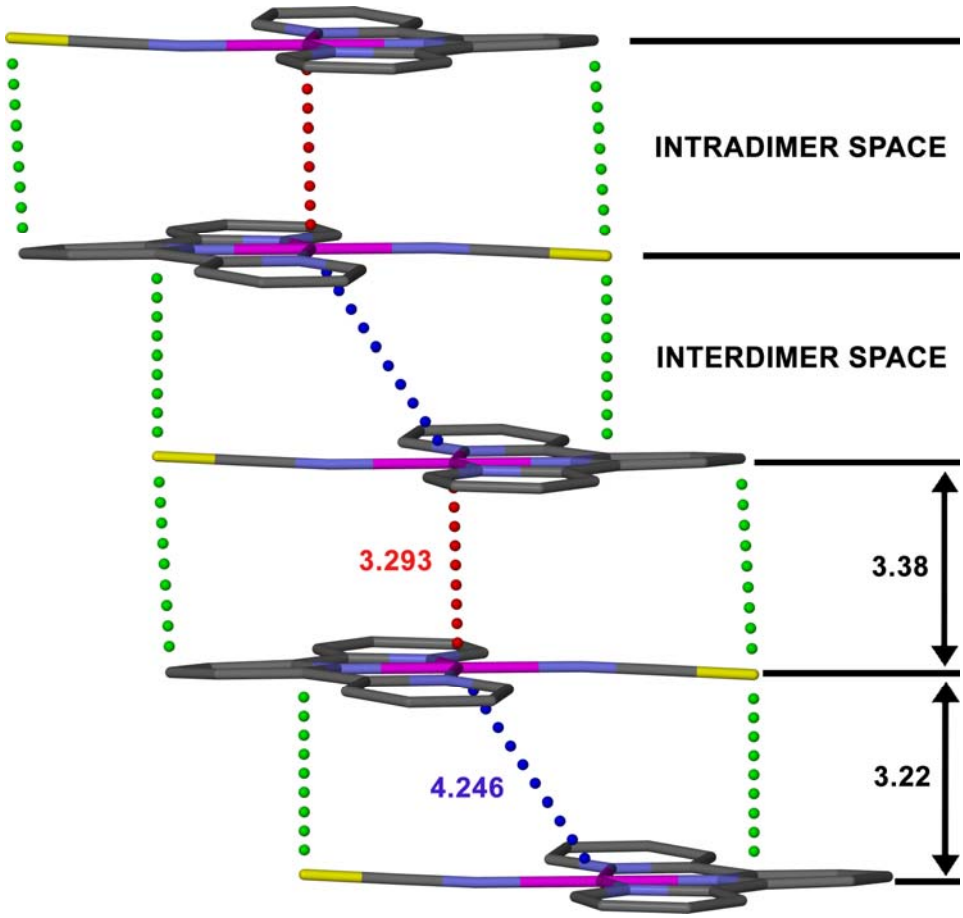

Figure 2.5 Diagram showing the head-to-tail zig-zag cation arrangement in **1·CH_3CN—Y**. Hydrogen atoms have been omitted for clarity. Dotted red and blue lines show the Pt∘∘∘Pt contacts. Dotted green lines represent the shortest S∘∘∘C(trpy) contacts. The interplanar separations were measured between mean planes taken through all the non-hydrogen atoms of the trpy ligand. All distances are in Å.

On the other hand, Figure 2.6(A) shows that the trpy ligands of the cations linked by the shorter Pt∘∘∘Pt distance are only slightly offset from an eclipsed overlap geometry of the platinum atoms. This is not what would be predicted from the rules developed by Hunter and Saunders (and later Janiak) for favourable stacking interactions between heteroatom aromatic systems;[49,50] this is because the electron rich nitrogen atoms of the outer pyridine rings are sufficiently close (~ 3.4 Å for N1 and N3) that electronic repulsions between them will dominate (rather than σ-π electrostatic interactions). The net result will be a destabilising π(trpy)-π(trpy) stacking interaction. However, this is compensated for by the energetically favourable d_{z^2}(Pt)-d_{z^2}(Pt) interaction that follows from the near

eclipsed (or conformeric) overlap geometry and the very short Pt◦◦◦Pt distance of 3.293 Å. Precisely this kind of overlap geometry [Figure 2.6(A)] has been observed for [Pt{4'-(Ph)trpy}Cl]BF_4;[10] and explained by Janiak using the same argument.[50]

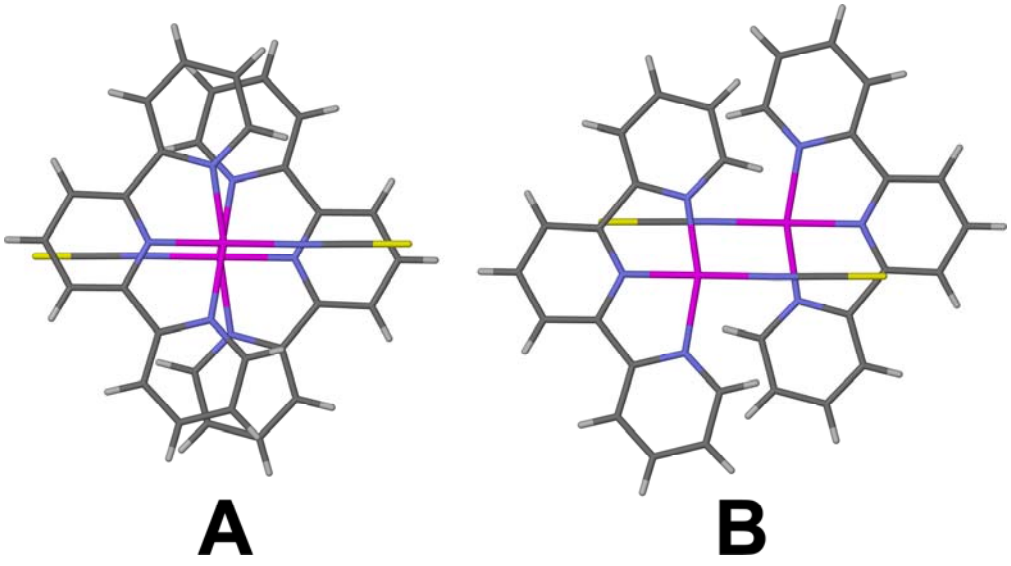

Figure 2.6 Diagram showing views perpendicular to the trpy mean planes of (A) the cations that are separated by the shorter Pt◦◦◦Pt distance, and (B) the cations that are separated by the longer Pt◦◦◦Pt distance: see text.

We conclude with an attempt to understand and explain the radical change in colour as solvent is lost from **1·CH_3CN─Y** to form **1─M**. As discussed in Section 1.3.1 of Chapter 1, the colour maroon is a reliable indication that there are d_{z^2}(Pt)-d_{z^2}(Pt) stabilising interactions that extend throughout the crystal. The question then becomes: "How do the cations in **1·CH_3CN─Y** change their position when solvent molecules are lost from the lattice?" As a starting point consider the diagrams shown in Figure 2.7. These show the relative juxtapositions of the cation stacks in **1·CH_3CN─Y** with the anions and solvent molecules included [Figure 2.7(A)] and with the solvent molecules artificially removed [Figure 2.7(B)]. We include on the diagrams short S◦◦◦H"─C"(trpy) contacts between stacks, specifically contacts that are shorter than the sum of the van der Waals radii for S and H atoms of 3.0 Å.[84] With these S◦◦◦H"─C"(trpy) non-bonded contacts as reference lines (or "links") it is possible to deduce by simple inspection of Figure 2.7, that the trpy ligands from adjacent stacks are not co-planar, but rather displaced by a distance of about

one third along a perpendicular line joining the cation planes. It is also important to note that there is a "zig-zag channel" of alternating anions and solvent molecules on either side of "linked" cation stacks; this can also be seen in Figure 2.4. For clarity an anion and solvent molecule pair 'in front' of the page have been coloured green, and an anion and solvent molecule pair behind the page have been coloured in orange. We postulate that the non co-planarity of adjacent cation stacks allows cations to shift laterally as solvent is lost, such that an extended chain structure of the platinum atoms in a stack is formed. Exactly how they shift is, of course, the subject of speculation but we expect that intact dimers, i.e. two cations linked by the very short Pt∘∘∘Pt distance of 3.293 Å, will move in unison into new positions. In this way, the stabilising d_{z^2}(Pt)-d_{z^2}(Pt) interaction would be retained. A proposed direction of shift of adjacent dimers is illustrated by the arrows in Figure 2.7(B) and the extended chain structure that would result is shown in Figure 2.7(C). Note that this model has the dimers moving into spaces previously occupied by solvent molecules and that there must also be a concomitant shift in the relative positions of the SbF_6^- anions; *cf* Figures 2.7(B) and 2.7(C). This is a very simple model that takes no account of any π(trpy)-π(trpy) stacking interactions that could influence the relative positions and orientations of cations in a stack; nor are ionic forces considered in any way. Nevertheless, it has the advantage of predicting extended d_{z^2}(Pt)-d_{z^2}(Pt) interactions in **1—M** that will be net stabilising. What does seem certain is that rather large shifts in atom positions will be required to achieve an extended chain structure and, therefore, it is not surprising that single crystals of **1·CH_3CN—Y** lose their single crystallinity when the solvent is lost and the maroon desolvated compound **1—M** forms. The above model implies that there must be a contraction of the lattice when solvent molecules are lost from **1·CH_3CN—Y** to give **1—M.** This has been checked by comparing the powder XRD spectrum measured for a microcrystalline sample of **1—M** with that calculated from the room temperature single crystal structure determination of **1·CH_3CN—Y**. The spectra are shown in Figure S1 of the Supporting Information on the CD attached to the inside back over of the thesis. The evidence from the comparison is clear: there is a consistent shift to higher 2θ values for the peaks (common to both spectra) in the spectrum of **1—M**. Thus a lattice contraction is, indeed, observed when crystals of **1·CH_3CN—Y** lose solvent to give a crystalline powder of **1—M**.

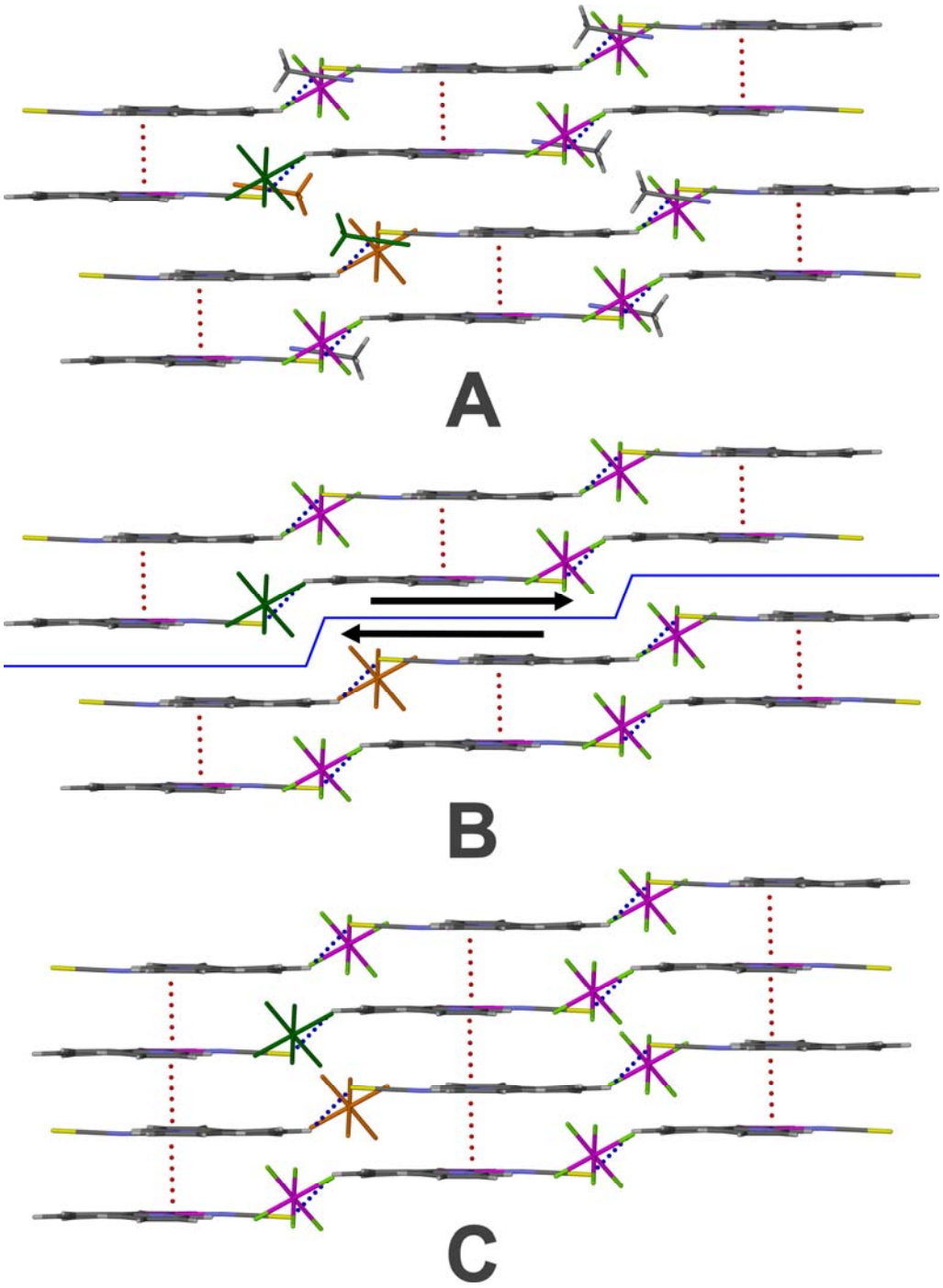

Figure 2.7 View parallel to the cation planes in **1·CH_3CN—Y** illustrating the relative juxtaposition of cation stacks with (A) anions and solvent molecules included and (B) solvent molecules artificially removed. A modified structure with an extended chain arrangement of interacting platinum atoms is shown in (C). The dotted purple lines represent the S∘∘∘H"—C"(trpy) non-bonded contacts. The dotted red lines represent Pt∘∘∘Pt distances less than 3.5 Å. The arrows in (B) indicate the possible direction of movement of adjacent dimers to give the extended chain structure in (C)

5 Solid state spectral properties of [Pt(trpy)(NCS)]SbF_6 (1—M)

5.1 Introduction

The maroon compound [Pt(trpy)(NCS)]SbF_6, labelled **1—M**, exhibits a range of intriguing photophysical properties in the solid state that we briefly introduce here. We first give the IUPAC definition of *thermochromism viz.* "a thermally induced transformation of a molecular structure or of a system, thermally *reversible,* that produces a spectral change, typically, but not necessarily, of visible colour."[85] There is no formal IUPAC definition of vapochromism, but *vapochromic* materials are characterised by a significant and *reversible* change of colour and/or emission upon exposure to the vapours of volatile organic compounds (VOCs).[9,86-91] As will be shown in the sections which follow:

- *Photoluminescence* by **1—M** is *temperature dependent*; the wavelength of the emission maximum changes systematically and reversibly with temperature over the range 80 to 473 K. As will be shown, the temperature dependence of the *intensity* of the emission is complicated at lower temperatures because of the presence of trap sites in the material.

- **1—M** is *thermochromic*; exhibiting colours that range from green (at 80 K = **1—G**) to maroon at room temperature (**1—M**) and orange (**1—O**) at 473 K. The changes in colour are fully reversible, and have been monitored by photographs that complement the above luminescence measurements.

- Above 473 K, starting at about 480 K, an irreversible change occurs in that the orange material, though retaining its orange colour, now does not return to the original maroon colour of **1—M** on cooling to room temperature; rather it stays orange. Thus, a new stable orange coloured phase is formed at ± 480 K that we

label **1—O^{HTP}** (HTP = high temperature phase) so as to distinguish it from the **1—O** compound that forms part of the thermochromic cycle of **1—M**. Interestingly, **1—O^{HTP}** itself is thermochromic, becoming yellow (**1—Y**) when heated to ± 520 K. However, heating **1—O^{HTP}** above ± 520 K affords a red material whose colour cannot be reversed by cooling; as such, it too, is a new high temperature phase, labelled as **1—R^{HTP}**. The changes in colour have been monitored by photographs; also, variable temperature solid state emission measurements have been recorded for **1—O^{HTP}** and **1—R^{HTP}**.

- **1—M** is *vapochromic*. As such, it changes colour reversibly upon exposure to the vapours of certain organic solvents, a process that has been monitored by photography. Corresponding changes in the emission spectra have also been recorded.

We follow the above sequence in the sections which follow, where we describe and discuss the details of each of the above properties of **1—M**; note that the starting material for all the investigations is a pure, dry and microcrystalline sample of **1—M**. However, for certain experiments, this material is crushed to a fine powder in a KBr matrix for reasons that will be given.

5.2 Variable temperature emission studies of 1—M

The solid state emission spectra of **1—M** have been recorded at 40 K intervals over the range 80-440 K with a further measurement at 473 K, as shown in Figure 2.8. The photophysical data that characterise the emission maximum recorded at each temperature are summarised in Table 2.2. At 473 K the spectrum consists of an asymmetric band centered at 654 nm, with a fwhm (full-width-at-half-maximum) value of 2 250 cm^{-1}. On reducing the temperature this band systematically shifts to longer wavelengths and, at the same time, becomes narrower: see the data in Table 2.2.

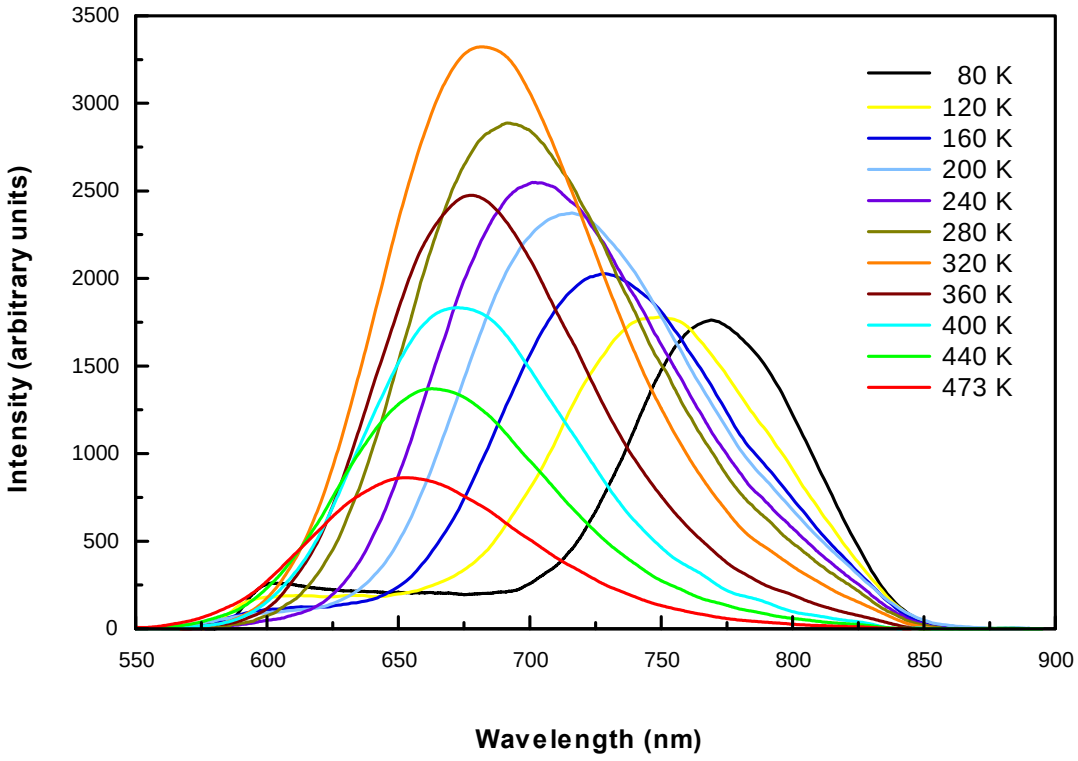

Figure 2.8 Solid state emission spectra of a microcrystalline sample of [Pt(trpy)(NCS)]SbF_6 (**1—M**) measured at 40 K intervals, with a final measurement at 473 K.

The variable temperature emission exhibited by **1—M** is typical of ^{3}MMLCT emission in a number of respects. Firstly, are the asymmetric profile and the lack of vibrational structure in the emission band. Secondly, and more importantly, are the red-shift of the emission maximum and narrowing of the band profile upon cooling of the sample. Indeed, analogous emissive characteristics have been observed for many other complexes, whose emissive behaviour has been attributed to radiative decay from a ^{3}MMLCT excited state.[1,6,9,10,12,15,16,18,19,23,24,48,86,92-94] The red-shift in the emission maximum on cooling can be explained as follows. Upon cooling, the unit cell dimensions of **1—M** are expected to contract resulting in a concomitant shortening of the Pt∘∘∘Pt separation. This allows for greater d_{z^2}(Pt)-d_{z^2}(Pt) orbital interactions, thereby reducing the HOMO-LUMO energy gap; and closing this gap leads to a lowering of the energy of the emission. That this process applies to **1—M** follows from its intense maroon colour. As discussed in Section

1.3.1 of Chapter 1, the colour maroon is indicative of extended metallophilic Pt∘∘∘Pt interactions in the solid state.[1,6,9,10,12,15,16,18,19,23,24,48,86,92-94] Moreover, we have already speculated that an extended chain structure for **1—M**, i.e. where the metallophilic interactions extend throughout the cation stack, would likely form when **1·CH_3CN—Y** is desolvated: see Figure 2.7 and the discussion in Section 4 of this chapter.

Table 2.2 Variable temperature photophysical data recorded on a pure microcrystalline sample of **1—M** [a]

Temperature (K)	λ_{em}^{max} (nm)	Intensity relative to 80 K spectrum	fwhm (cm^{-1})	τ (μs) [b]
80	769 [762]	1 [1]	1331 [1424]	1.1
120	750 [744]	1.01 [0.99]	1721 [1729]	0.9
160	729 [726]	1.15 [0.96]	1881 [1918]	0.7
200	716 [710]	1.35 [0.76]	2011 [1995]	-
240	701 [700]	1.45 [0.44]	2069 [2046]	-
280	692 [692]	1.64 [0.20]	2152 [2105]	-
320	682	1.89	2105	-
360	677	1.40	1982	-
400	672	1.04	2055	-
440	663	0.78	2111	-
473	652	0.49	2223	-

[a] Values in square brackets indicate those recorded on **1—M** ground in a matrix of KBr: see text. [b] Due to instrumental limitations only lifetimes longer than 0.5 μs could be recorded; for this reason the shorter lifetimes at T > 160 K are not shown.

For comparison purposes we report here the details of the ^{3}MMLCT emission exhibited by red [Pt{4'-(*o*-$CH_3C_6H_4$)trpy}Cl]SbF_6 between 280 and 80 K.[18] In this case, λ_{em}^{max} red-shifts from 616 nm at 280 K to 673 nm at 80 K. The $\Delta\lambda_{em}^{max}$ of 57 nm is significantly less than that recorded for **1—M** over the same temperature range; as shown by the data in Table 2.3, the corresponding $\Delta\lambda_{em}^{max}$ value for **1—M** is 77 nm. Indeed this $\Delta\lambda_{em}^{max}$ value is, to the best of our knowledge, the largest value recorded for an ionic platinum

terpyridine that exhibits ^{3}MMLCT emission. Connick and co-workers quantified the dependence of the energy of the ^{3}MMLCT emission on the Pt∘∘∘Pt distance in $[Pt(bipy)Cl_2]$, a compound that contains platinum atoms that are uniformly separated in an extended stack.[92] They found that the emission peak energy decreases linearly with the inverse cube of the Pt∘∘∘Pt distance.[92] Clearly, this is a relationship that we cannot test on **1—M**, since we have not been able to grow single crystals of **1—M** to determine its crystal structure. Nevertheless, we are in a position to make two important points at this juncture. Firstly, the largest values for $\Delta\lambda_{em}^{max}$ are observed for complexes of platinum(II) with extended chain structures and a uniform Pt∘∘∘Pt separation: the compounds $[Pt\{o\text{-}CH_3C_6H_4(trpy)\}Cl]SbF_6$,[18] and $[Pt(bipy)Cl_2]$,[92] are good examples. Second, bipyridyl and terpyridyl ligand complexes of platinum(II) that have extended chains of interacting platinum atoms are invariably red (or dark red = maroon) in colour.[9,16,18,22,24,29,48,92] We therefore conclude, albeit by inference, that **1—M** has an extended chain structure of uniformly separated platinum atoms, i.e. there is endless d_{z^2}(Pt)-d_{z^2}(Pt) orbital overlap along the stack .

We now examine more closely the variation in intensity of the ^{3}MMLCT band as the temperature of the sample is dropped from 473 to 80 K. As shown by the data in Table 2.2 (and by inspection of Figure 2.8) there is a systematic increase in intensity of the band on cooling from 473 to 320 K. This is expected: when the solid is cooled the mean vibrational displacement of the atoms decreases, resulting in a decrease in the amount of energy lost from the emitting state *via* atom vibrations, i.e. the non-radiative decay rate constant decreases. What is unexpected is that, at temperatures below 320 K, the intensity of the emission actually decreases! A clue to understanding this apparent anomalous intensity variation comes from a closer examination of the emission spectra recorded at the lower temperatures. At 80 K, it is particularly evident that there is an additional small peak centered at ~ 600 nm: we have highlighted the variation in intensity of this peak with temperature in Figure 2.9. As shown in Figure 2.9, its intensity increases with a decrease in temperature; nevertheless it makes only a small contribution to the overall (integrated) intensity of the emission.

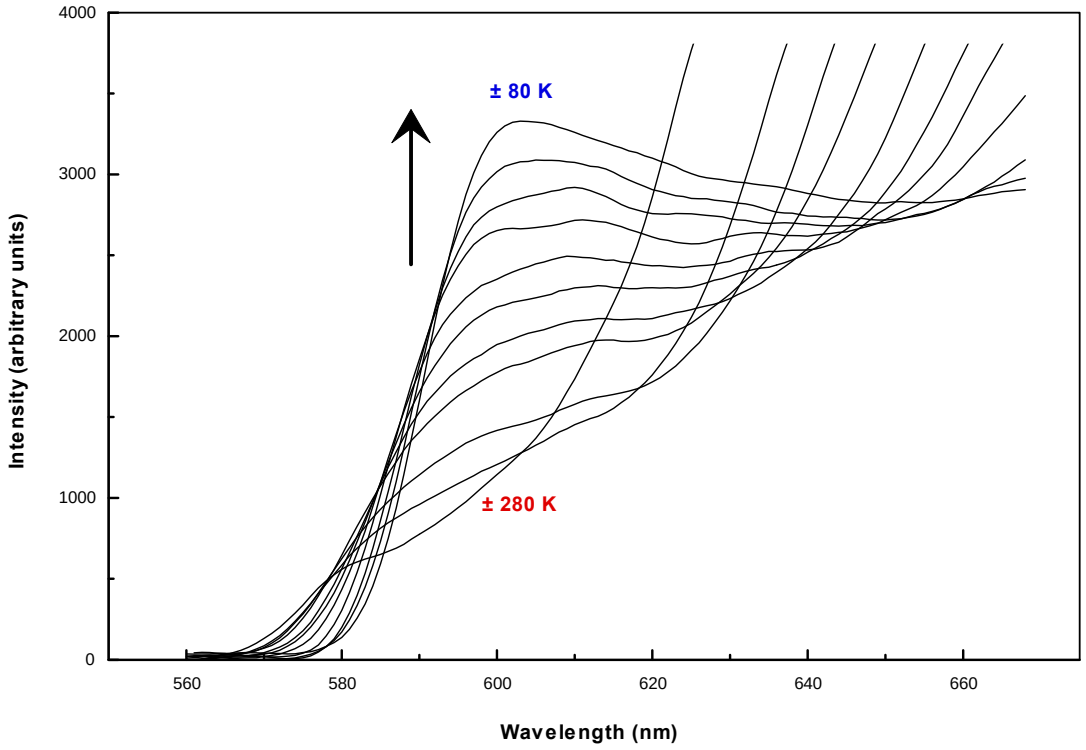

Figure 2.9 Variable temperature emission from the trap sites (centered at ~ 600 nm) in [Pt(trpy)(NCS)]SbF6 (**1—M**). The diagrams show how the trap site emission band increases in intensity as the temperature decreases.

In explaining the origin of the 600 nm peak we firmly believe that it is not due to an impurity in the sample; as already noted the purity of the sample has been checked by, *inter alia*, elemental analysis for %C, H and N, using the professional services of Galbraith Labs, in Knoxville, Tennessee: see Section 3.1 of Chapter 4. It is also clear that the ^{3}MMLCT emission at much longer wavelengths dominates and is, therefore, representative of the bulk material, i.e. not the peak at 600 nm, which is relatively small. The most likely explanation for the 600 nm peak follows when we consider how a microcrystalline sample of **1—M** is obtained in the first place; this was by desolvation of **1·CH$_3$CN—Y**. We propose that when **1·CH$_3$CN—Y** desolvates, the metal-organic framework collapses resulting in the formation of **1—M** with a crystal lattice that is not fully ordered, i.e. it contains defect sites, in particular lattice sites that have an environment which is different to that of the bulk lattice sites.[10,34,95] These defect sites are

spatially distinct from the regular lattice sites.[95] Thus, when the sample is irradiated (with 420 nm light) not only are the species that comprise the bulk material excited but also the species at the defect sites.[95] We speculate below as to the nature of these defect sites but, for the moment, we note that emission by a defect site is at a higher energy (λ_{em}^{max} = 600 nm) than the ^{3}MMLCT emission by the bulk material. At relatively high temperatures of > 320 K, the excited state energy of the defect site is rapidly transferred *via* atom vibrations to the lower energy ^{3}MMLCT state; and we only observe ^{3}MMLCT emission in the spectrum.[10,95] However, as the temperature is lowered below 320 K, the thermally-mediated energy migration is slowed down because the atoms vibrate more slowly, and not only is emission by the defect site no longer fully dissipated, but actually observed; moreover, the intensity of the ^{3}MMLCT emission inevitably decreases.[10,34,95] Note that the emission measurements were made by the steady state method, i.e. the sample is continuously irradiated with ultraviolet light of 420 nm wavelength while monitoring the emission: see Section 2.3 of Chapter 4 for the experimental details. Thus the above argument that depends on the rate of transfer of the excited state energy of the defect site to the bulk material applies. As to the nature of the defect sites we speculate that they are sites where the SCN^- is bonded to the platinum atom through the S atom, i.e. as the thiocyanate ion. There is no way of proving this since the defect sites make-up a tiny fraction of the crystal lattice; indeed bulk properties of the material (such as its maroon colour) are determined only by the crystal packing of the isothiocyanate ligand complexes.[95] On the other hand, the energy of the emission by such a defect site (S-bound isomer of **1**) is expected to be at a higher energy than the ^{3}MMLCT emission; this is because the stabilising d_{z^2}(Pt)-d_{z^2}(Pt) orbital interactions that that lead to the low energy of the ^{3}MMLCT emission are not possible when the linkage isomer is the S-bound one; see the discussion in Section 2 of Chapter 1.

For the purposes of the studies of the vapochromism of **1—M** the macrocrystalline sample was ground to a finely-divided powder in a 1:5 KBr matrix for 10 minutes: see Section 5.5 below. At the same time, the temperature dependence of the emission by this sample was recorded: the results are shown in Figure 2.10 while a listing of the photophysical data is given in Table 2.2.

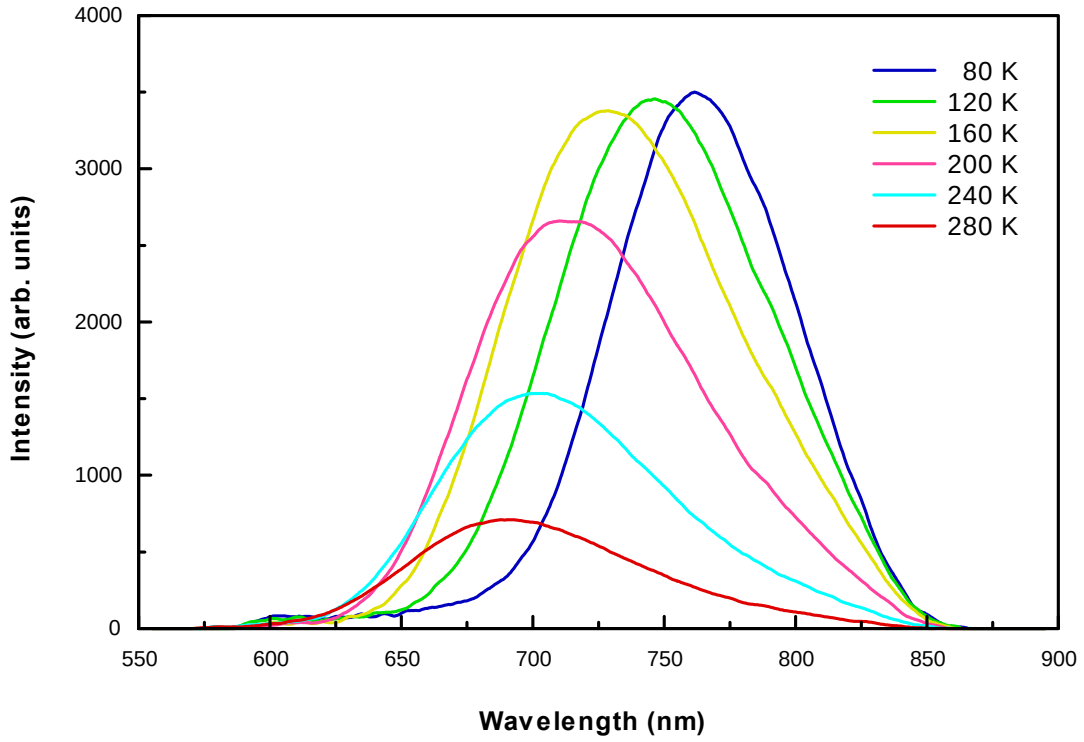

Figure 2.10 The solid state emission spectra of [Pt(trpy)(NCS)]SbF_6 (**1—M**) ground in a KBr matrix, recorded at 40 K intervals from 80-280 K.

Examination of Figure 2.10 and the data in Table 2.2 shows that all the essential features of the ^{3}MMLCT emission remain the same, e.g. the wavelengths of the peak maxima and band profiles are virtually identical to those recorded on the original pure macrocrystalline sample: see Figure 2.8 and Table 2.2. However there is now the expected systematic increase in the intensity of the emission as the temperature is lowered, at least as far as 160 K. Below 160 K the intensity of the bulk material emission only increases slightly: see Figure 2.10. Also noteworthy is that the peak at ~ 600 nm (due to defect site emission) is relatively small as compared to its contribution to the emission from the pure macrocrystalline sample of **1—M** at low temperatures: compare Figures 2.8 and 2.10. We do not have an exact explanation of why, through grinding the sample in KBr, the defect sites are apparently "ironed-out" – to coin a phrase. It may be linked to the fact that when the SCN^- is bonded to the platinum atom through the S atom,

the ligand protrudes out of the plane of the Pt(trpy) moiety; and crushing simply forces it into the plane by converting from the S-bound to the N-bound isomer. Also true is that crushing is, in general, expected to give the thermodynamically more stable form in the solid state, in this case the complex where the SCN^- ion is N-bound in a "rod-like" fashion.[64]

5.3 Thermochromic properties of 1—M

5.3.1 Introduction

The majority of commercially available thermochromic materials are organic compounds of two types – liquid crystals or leucodyes.[96] In cholesteric type liquid crystals the colour of the reflected light (colour) is controlled by the refractive index of the liquid crystal and pitch of the helical arrangement of adjacent molecules.[97] Since the pitch and length of this helical arrangement varies with temperature, so does the wavelength of the reflected light – thereby resulting in colour changes.[97] Liquid crystal materials are used in aquarium and forehead thermometers, but are limited by their very narrow temperature range (1 K or less) and comparatively high expense.[98] Leucodyes exhibit colour changes in response to temperature *via* the rearrangement of molecular structure – known as molecular switches. These are molecules that change colour in solution due to the making/breaking of covalent bonds and/or changes in the conformation of the molecule.[99,100] Well documented examples are the overcrowded bistricyclic aromatic enes (BAEs) reported by Biedermann and co-workers, where a reversible colour change from colourless-yellow at room temperature to a green thermochromic form is observed.[99] Colour changes associated with the processes discussed above typically experience a relatively abrupt transition point, as opposed to a gradual change in colour as the temperature changes.[96-100]

Lippard and co-workers have reported a series of platinum(II) complexes of the ethidium cation (Etd) which, in solution, show reversible optical spectroscopic changes that are dependent on temperature.[100] For example, a methanol solution of the acetate salt of

cis-$[Pt(NH_3)_2(N3\text{-}Etd)Cl]^{2+}$ gradually changes from orange to deep blue upon warming from -20 to 50 ºC. The colour change is induced by deprotonation of the ethidium ligand by the acetate ion at elevated temperatures, and is reversed when protonation occurs on cooling; at room temperature the protonated and deprotonated forms are in equilibrium with each other.[100]

The potential downfall of many thermochromic compounds (including those discussed above) is that since they are liquids and/or multiple component mixtures, they have to be encapsulated in small polymer spheres.[96,98] These spheres often have poor thermal stability and are not conducive to extensive further processing.[96] The abrupt colour changes, (which result in small operation "windows") and weak contrasts between colours and poor response times at the thermochromic transition temperature can also be limiting factors.[96]

There are very few examples in the literature of ***solid*** materials that exhibit thermochromic behaviour; one example is the transition metal/mercury cyanide coordination polymer comprising $Hg(CN)_2$ and MX_2 (X^- = Cl^-, Br^- and I^-).[101] The migration of labile halides of the MX_2 salts through the polymer to the Hg(II) centres (which act as a soft Lewis base) accounts for the thermochromic properties of the coordination polymer.[101]

We gave in Section 5.1 the IUPAC definition of the term "*thermochromism*". In terms of this definition we have already shown in Section 5.2 that **1—M** is thermochromic: after all, the compound undergoes a "spectral" change, specifically in its emission spectrum that is "thermally induced" and fully reversible. However a simpler interpretation of "*thermochromic*" is that a compound changes colour, i.e. the wavelength of the transmitted light changes, in a way that is easily observed by the naked eye. As will be shown in the next section, **1—M** does exhibit this kind of thermochromic behaviour.

5.3.2 Thermally induced reversible colour changes exhibited by 1—M

As already noted the compound $[Pt(trpy)(NCS)]SbF_6$ is maroon in colour at room temperature (298 K); hence the label **1—M**. Upon cooling of **1—M** to ~ 77 K (using liquid nitrogen) a dark green solid is obtained, which rapidly returns to the maroon colour once removed from the liquid nitrogen. If heated to 473 K, **1—M** acquires an orange colour, which also reverts to the maroon coloured form when cooled to room temperature. The colour changes described above are illustrated in Figure 2.11.

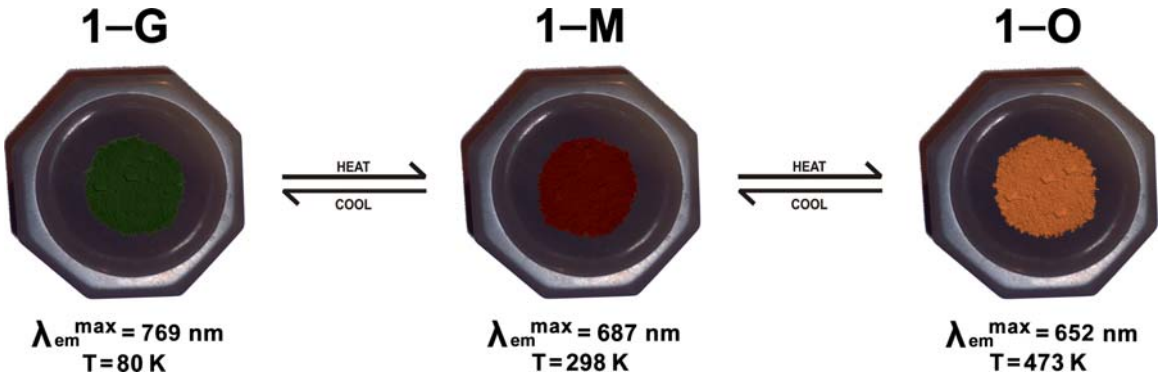

Figure 2.11 Thermally induced colour changes of $[Pt(trpy)(NCS)]SbF_6$ (**1**).

It should be noted that the colour changes do not occur abruptly (as is often the case with many other thermochromic materials); rather there is a gradual colour change, e.g. the green solid when heated turns blue, maroon, red, light red and then finally orange at 473 K. Also important to note is that the colour changes are fully reversible, and can be cycled through indefinitely without any degradation of the sample, provided the temperature of 473 K is not exceeded: see the discussion in Section 5.4.1 below. Thus, **1—M** is correctly described as *thermochromic*. Finally, we note that the colour changes should be reflected in changes in the excitation spectrum obtained in the normal way by monitoring the intensity of the emission maximum as a function of the excitation wavelength. Accordingly, we have recorded excitation spectra over the full temperature range but, surprisingly, there are no obvious differences, i.e. they all appear to be essentially the same as the spectrum recorded at 77 K; this spectrum is shown in Figure

2.12. We have no clear explanation for this, except that excitation spectra are generally poorly resolved and that the (small) differences in the electronic structure of the solid that lead to the colour changes, may not be detectable as changes in the excitation spectra.

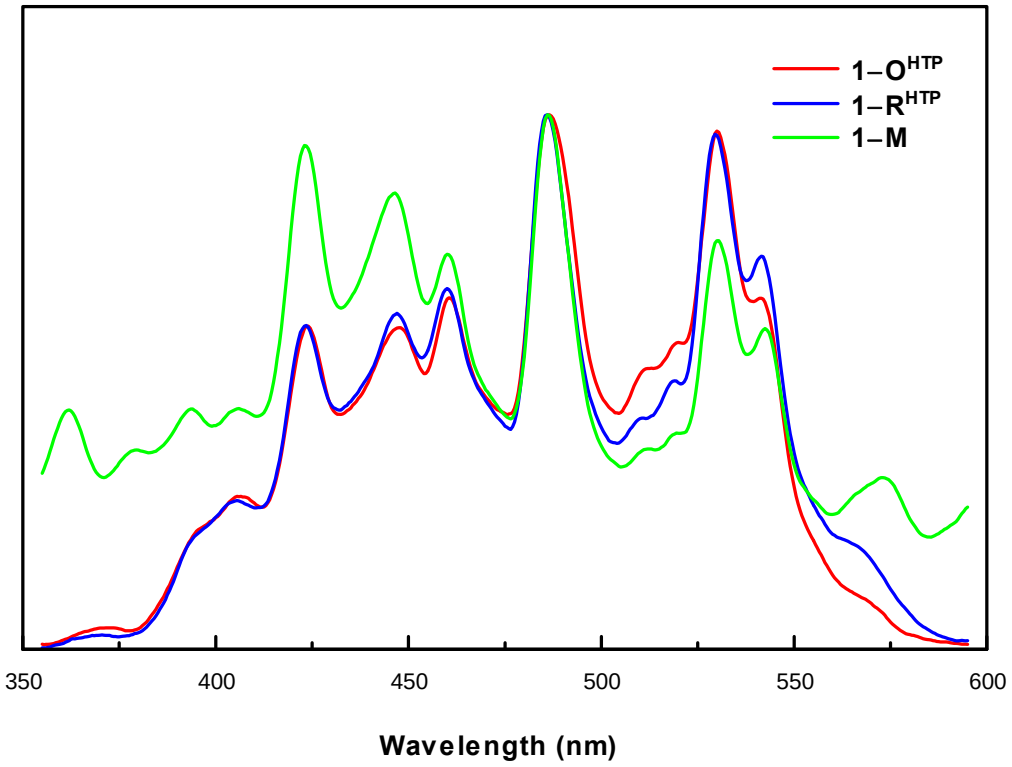

Figure 2.12 Excitation spectra of **1—M**, **1—O^{HTP}** and **1—R^{HTP}** recorded at 77 K.

We now address the question of why the material undergoes the above colour changes. There is a wealth of literature that shows that the colours of materials containing stacked terpyridyl ligand complexes of platinum(II) are dependent on the extent of the d_{z^2}(Pt)-d_{z^2}(Pt) orbital interactions in the stack: the discussion in Section 1.3.1 of Chapter 1 refers. As already noted a maroon (or deep red) colour indicates the presence of extended d_{z^2}(Pt)-d_{z^2}(Pt) orbital interactions throughout the stack.[9,16,18,22,24,29,48,51,64,92] An orange (or deep yellow) colour indicates that the cation stack comprises a series of well separated Pt_2 dimers;[3,12,15] precisely the structural motif observed in the crystal structure of **1·CH$_3$CN—Y**. We are aware of only one other terpyridyl ligand complex of platinum(II) that is green in colour. This is the dark-green polymorph of the dynyl

complex [Pt(trpy)(C=C—C≡CH)]OTf (where OTf = triflate) with a crystal structure that comprises an extended linear chain of interacting platinum atoms; the red form of the same compound displays a zig-zag arrangement of Pt_2 dimers.[51] Thus we conclude: the thermally induced colour changes of [Pt(trpy)(NCS)]SbF_6 derive from the planar $[Pt(trpy)(NCS)]^+$ cations moving in and out of the different positions with respect to each other in the stack as the temperature is changed. In so doing, the d_{z^2}(Pt)-d_{z^2}(Pt) orbital interactions are modified and the colour of the material changes. Of course, the link between colour and the extent of d_{z^2}(Pt)-d_{z^2}(Pt) orbital interactions is well-established in ionic platinum terpyridines, so we have made the obvious conclusion. What *is* unusual is that by simply changing the temperature, the cations in [Pt(trpy)(NCS)]SbF_6 move into new positions; given the planarity of the cation we presume they *slide* into new positions: see also the crystal structure discussion in Section 4 of this Chapter. The pity is that we have not been able to grow single crystals of [Pt(trpy)(NCS)]SbF_6, at least not to date. (A near successful attempt involved the slow diffusion of diethyl ether into a concentrated solution of the compound in *benzonitrile*). Were a single crystal structure determination available, we would be in a much better position to explain the fascinating and unusual thermochromic behaviour of [Pt(trpy)(NCS)]SbF_6; especially as it is an unusual form of thermochromism, since the mechanism that underpins the colour changes is very different to anything that has been reported previously: see the discussion in Section 5.3.1 above.

5.4 Preparation, characterisation and photophysical properties of 1—O^{HTP} and 1—R^{HTP} (HTP = high temperature phase)

5.4.1 Preparation

The high temperature phase, **1—O^{HTP}**, is formed when **1—M** is heated beyond its thermochromic range (80-473 K) to a temperature of ± 480 K. There is an irreversible phase change at ± 480 K, as evidenced by the fact that when **1—O^{HTP}** is cooled to room temperature it retains its orange colour, i.e. maroon **1—M** does not reform. As discussed below, **1—O^{HTP}** has thermochromic properties but, here we note that when **1—O^{HTP}** is heated beyond 518 K an abrupt and irreversible change to a second high temperature

phase occurs *viz*. **1—R^{HTP}**; this is illustrated in Figure 2.13. [The formation of the intermediate bright orange-yellow compound (**1—Y**) shown in Figure 2.13 is discussed in Section 5.4.3 below.]

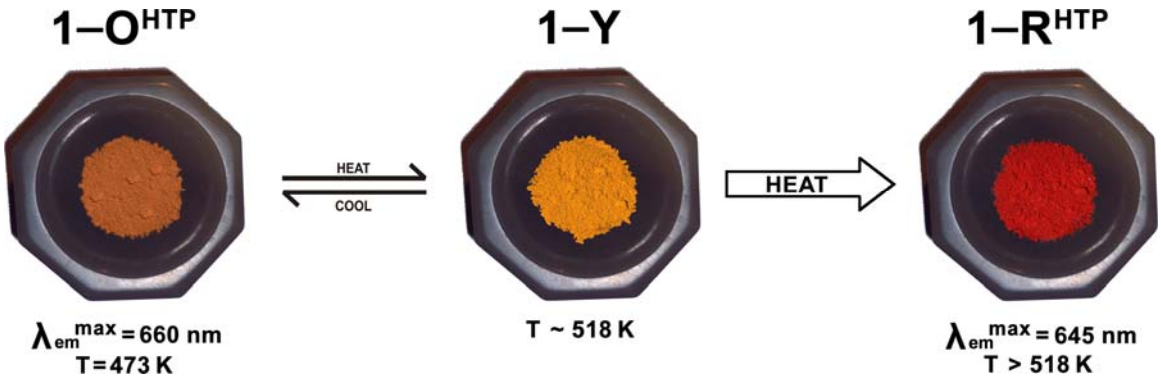

Figure 2.13 Thermal transformation of **1—O^{HTP}** to give **1—R^{HTP}**, and thermochromism displayed by **1—O^{HTP}**.

5.4.2 Characterisation

Infrared spectra have been recorded as KBr discs of **1—O^{HTP}** and **1—R^{HTP}**. The peaks observed are almost identical in all respects to those recorded for **1—M**: see Section 3.1 of Chapter 4. The ν[SC≡N] stretching frequency decreases slightly to 2089 cm^{-1} and the ν[S–CN] stretching frequency remains at ~ 870 cm^{-1}. The infrared data serve to confirm the SCN^- ion remains N-bound throughout all the colour and phase changes.[60-63]

We have also recorded powder XRD spectra for **1—O^{HTP}** and **1—R^{HTP}**; these are shown in Figure 2.14(A) and (B) together with the powder pattern obtained for **1—M.** We first note that there are significant differences in the peak positions and intensities for **1—M** on one hand, and for **1—O^{HTP}** and **1—R^{HTP}** on the other. This confirms that a phase change occurs when **1—M** is transformed into **1—O^{HTP}** (and subsequently into **1—R^{HTP}**) on heating; moreover the phase changes are irreversible. More specifically, the general shift to higher angles of 2θ of the peaks for **1—O^{HTP}** and **1—R^{HTP}** show that there is a decrease in the size of the unit cell for the two high temperature phases. It is apparent from the

high angle powder XRD spectra in Figure 2.14(B) that there are small shifts to higher 2θ values upon formation of **1—R^{HTP}** from **1—O^{HTP}**, indicating that a phase change does take place; and moreover that the transformation is accompanied by a very small decrease in the unit cell volume – a feature which will hold greater significance at a later stage.

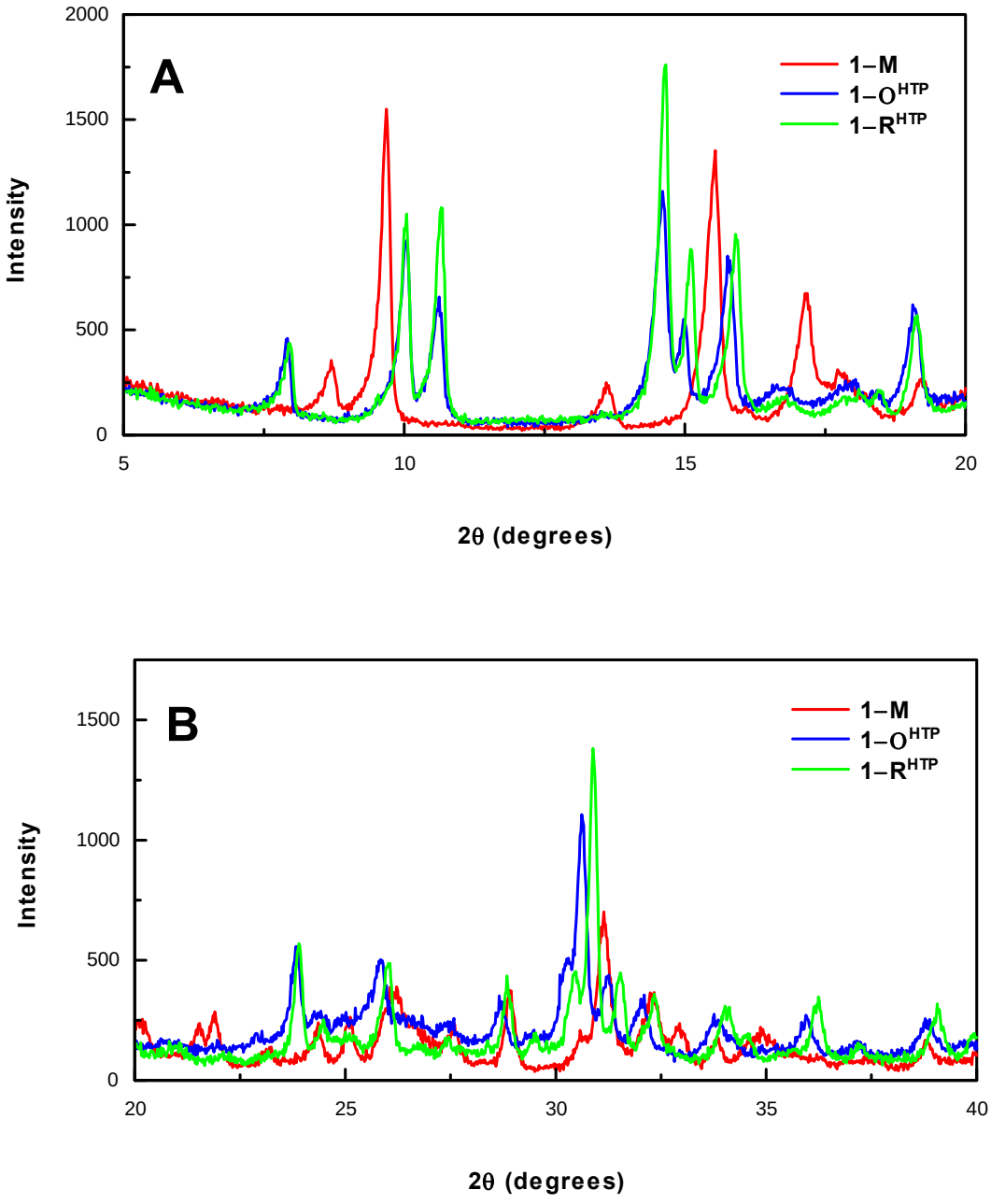

Figure 2.14 Comparison of the experimentally measured powder XRD patterns recorded of **1—M**, **1—O^{HTP}** and **1—R^{HTP}** at 295 K; in the (A) lower 2θ range of 5-20° and (B) the higher 2θ range of 20-40°.

5.4.3 Photophysical properties of 1—O^{HTP} and1—R^{HTP}

We start with the emission spectra that have been recorded on the solid samples of **1—O^{HTP}** and **1—R^{HTP}**. For **1—O^{HTP}**, emission spectra were recorded at 480, (i.e. just after **1—O^{HTP}** has formed) 298 and 77 K: see Figure 2.15. At 480 K an unstructured, but asymmetric and relatively broad band that maximises at 645 nm is observed. Dropping the temperature to 298 and 77 K causes the emission maximum to systematically red-shift to 660 and 700 nm respectively; at the same time the band narrows. As previously discussed, this pattern for the dependence on the temperature of the emission is entirely typical of ^{3}MMLCT emission:[1,6,9,10,12,15,16,18,19,23,24,33,48,64,86,92-94] there must be d_{z^2}(Pt)-d_{z^2}(Pt) orbital interactions present in the solid state that strengthen due to lattice contraction as the temperature is lowered.[1,6,9,10,12,15,16,18,19,23,24,33,48,64,86,92-94] However, the red-shift on cooling is not as marked as for **1—M**. By comparing the spectra in Figure 2.15 with those in Figure 2.8 it is apparent that the $\Delta\lambda_{em}{}^{max}$ (280–80 K) value for **1—M** of 77 nm is much larger than the $\Delta\lambda_{em}{}^{max}$ (298–77 K) value for **1—O^{HTP}** of only 40 nm. This difference is expected given the different colours for the two materials of maroon for **1—M,** and orange for **1—O^{HTP}**. As noted in Section 1.3.1 of Chapter 1 the colour orange is indicative of stacked Pt_2 dimers in the solid state whereas a maroon colour suggests strongly that d_{z^2}(Pt)-d_{z^2}(Pt) orbital interactions extend throughout the cation stack. And, the red-shift in the emission maximum for a stacked dimer structure is invariably less than that of an extended chain structure with uniform Pt∘∘∘Pt distances.[1,6,9,10,12,15,16,18,19,23,24,33,48,64,86,92-94] Changes in the extent and strength of the d_{z^2}(Pt)-d_{z^2}(Pt) orbital interactions also explain why lower energy emission ($\lambda_{em}{}^{max}$) is observed **1—M** than **1 —O^{HTP}**. Finally, with regard to the emission spectrum recorded for **1—O^{HTP}** at 77 K, we note the appearance of a new peak at about 590 nm: see Figure 2.15. This peak we assign as arising from defect site emission, by analogy with the arguments used to explain the peak at 600 nm observed in the low temperature emission spectra of **1—M**: see Figure 2.8. Interestingly, the presence of the trap site has no apparent effect on the intensity of the emission by **1—O^{HTP}**; as expected it increases as the temperature decreases: see Figure 2.15. However this apparent observation is almost certainly misleading; were we to have measured emission spectra at smaller intervals between

298 and 77 K it is most probable that the anomalous variation in the intensity of the emission would have been observed.

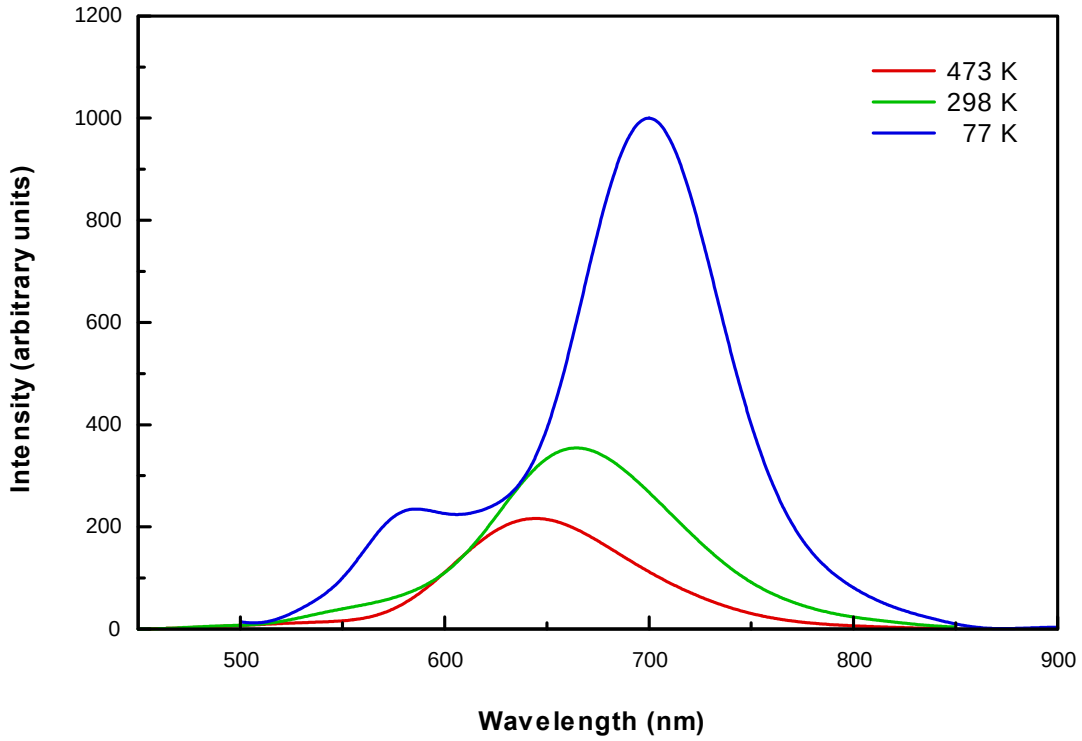

Figure 2.15 Solid state emission spectra of **1—O**^{HTP} recorded at 473, 298 and 77 K.

Emission spectra for the other high temperature phase, **1—R**^{HTP}, have been recorded at room temperature (298 K) and 77 K: see Figure 2.16. At 298 K the band is weak, very broad and centered at about 645 nm; at 77 K it is much narrower and centered at 718 nm. Again, and for the same reasons, we assign the emission as ^{3}MMLCT. For **1—R**^{HTP}, the red-shift on cooling from room temperature to 77 K is 73 nm. Thus, the trend in $\Delta\lambda_{em}{}^{max}$ and $\lambda_{em}{}^{max}$ values follows the order: **1—O**^{HTP} < **1—R**^{HTP} < **1—M**, a trend that is entirely consistent with the colours and powder patterns of the three phases.[3,9,12,15,16,18,22,24,48,64,92] Also note the absence of a defect site emission band (at ~ 600 nm) in the 77 K spectrum of **1—R**^{HTP}. This is consistent with further compaction of the crystals as evidenced by the comparatively smaller unit cell for **1—R**^{HTP} as compared to that for **1—O**^{HTP}: compare the powder XRD spectra in Figure 2.14. Further compaction is facilitated when the defect

sites are transformed into regular sites by converting the thiocyanate ligand into an isothiocyanate ligand.

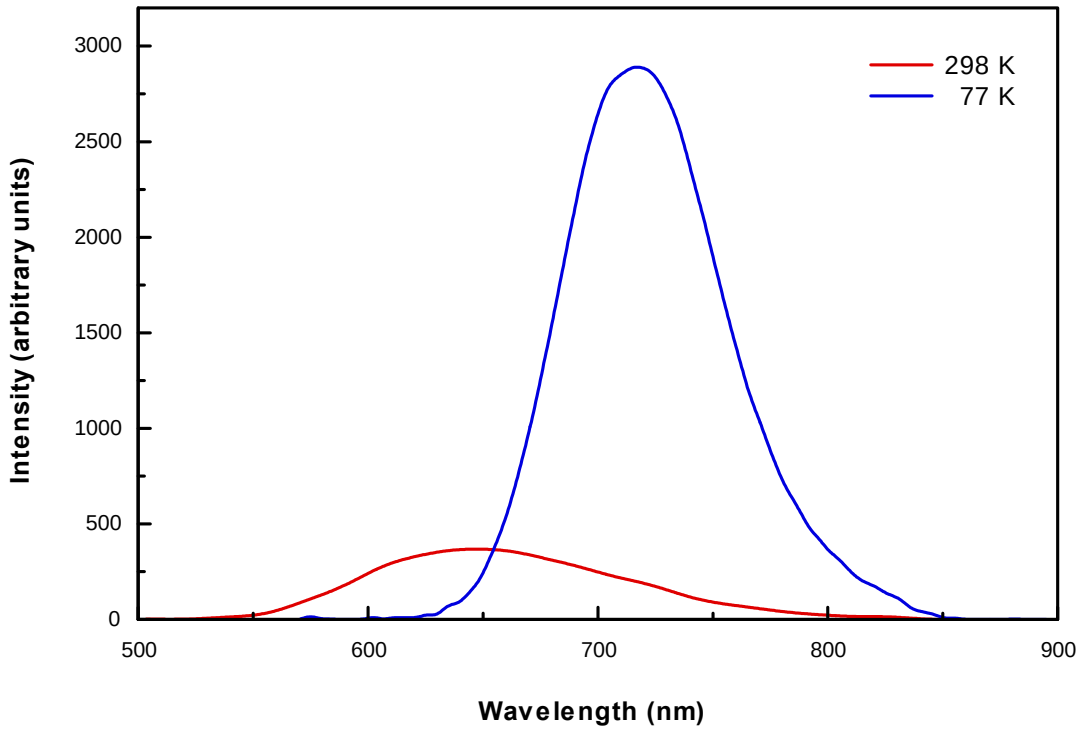

Figure 2.16 Solid state emission spectra of **1—R^{HTP}** recorded at 298 and 77 K.

We next address the thermally induced colour changes that **1—O^{HTP}** undergoes: see Figure 2.13. Interestingly, the orange **1—O^{HTP}** phase gradually changes colour to bright orange-yellow when heated and, provided a temperature of 518 K is not exceeded, cooling affords the original orange material again: thus **1—O^{HTP}** is thermochromic over the temperature range of 298-518 K. Using the same reasoning applied to **1—M**, we conclude that the colour change from orange to yellow is a consequence of the platinum atoms shifting their positions such that the d_{z^2}(Pt)-d_{z^2}(Pt) orbital interactions are modified. A more dramatic and irreversible colour change to the red **1—R^{HTP}** phase is observed at temperatures above 518 K: see Figure 2.13. Thus, at T > 518 K, the platinum atoms appear to be "locked-in" to new positions in the red **1—R^{HTP}** phase.

We finally address the question of the different colours observed for **1—M**, **1—O^{HTP}** and **1—R^{HTP}**. The different colours are most likely to do with the different relative positions and separations of the platinum atoms within the $[Pt(trpy)(NCS)]^+$ cation stacks in **1—M**, **1—O^{HTP}** and **1—R^{HTP}**: see earlier arguments and similar explanations offered by other authors for differently coloured ionic platinum terpyridines.[9,15,16,24,28,51] Though we do not have a single crystal structure determination to support our conclusions, the powder XRD spectra in Figure 2.14 do, at least, confirm that there are significant differences in the unit cell dimensions for **1—M**, **1—O^{HTP}** and **1—R^{HTP}**; and changes in the unit cell dimensions imply differences in the dimensions of the platinum atom stacks. The implication is that there are small but detectable differences in the crystal structures of **1—O^{HTP}** and **1—R^{HTP}** that account for the differences in colour. Excitation spectra of **1—O^{HTP}** and **1—R^{HTP}** have been recorded at 77 K: these are shown in Figure 2.12 along with the excitation spectrum recorded for **1—M** at 77 K. (The excitation spectra were recorded at 77 K in order to improve the signal to noise ratio.) Interestingly, the excitation spectra of **1—O^{HTP}** and **1—R^{HTP}** are very similar, but significantly different to that of **1—M**; an observation that is consistent with the powder XRD spectra for **1—O^{HTP}** and **1—R^{HTP}** being similar, but quite different to that recorded for **1—M**.

5.5 Vapochromic properties of 1—M

5.5.1 Introduction

Studies of vapochromic complexes of platinum(II) have been stimulated by the quest for materials that function as optical sensors, i.e. materials whose optical properties change according to their environment.[9,86-91]

The first reported examples of platinum(II) salts that exhibit a vapochromic response were the compounds [Pt(Me_2bzimpy)Cl]X {where Me_2bzimpy = 2,6-bis(1-methylbenzimidazol-2-yl)pyridine, and X^- = Cl^- or PF_6^-}.[86] The chloride derivative shows an indiscriminate vapochromic response when exposed to a wide variety of

volatile organic compounds (VOCs). However, the hexafluorophosphate salt is selective towards vapours of acetonitrile.[86]

Probably the best studied systems are the double salts, typified by $[Pt(CNR)_4][Pt(CN)_4]$ (R = $C_{12}H_{23}$ or $C_{14}H_{29}$) that have been investigated by Mann and co-workers.[87] Vapochromic behaviour by these systems is believed to be a result of changes to the intermolecular Pt∘∘∘Pt distances caused when solvent molecules are included in the lattice causing it to expand.[87] However, although these double salts of platinum(II) show promise as optical sensors, they do suffer from several disadvantages.[9] In particular, there are difficulties associated with tuning the vapochromic response to specific VOCs – obviously, a desirable property for an application-based optical sensor.[9]

In so far as vapochromic ionic platinum terpyridines are concerned, the best characterised example is the complex $[Pt(Nttpy)Cl](PF_6)_2$ where Nttpy = 4'-(*p*-nicotamide-N-methylphenyl)-2,2':6',2''-terpyridine.[9] The compound is red, but when exposed to vapours of methanol it turns orange. Eisenberg and co-workers have determined the single crystal structures of both the red and (solvated) orange forms, and conclude that sorption of methanol vapours disrupts the metallophilic Pt∘∘∘Pt interactions and so the colour (and emission spectrum) of the material changes.[9] As noted by Eisenberg and co-workers, the $[Pt(Nttpy)Cl](PF_6)_2$ complex demonstrates a much more selective vapochromic response than Mann's double salts; because only pyridine and acetonitrile, in addition to methanol, cause the complex to change from red to orange in colour. However there is no evidence in the report by Eisenberg and co-workers that they have investigated the change in the *emission* spectrum when the complex is exposed to pyridine and acetonitrile.[9] It is, therefore, not clear whether the vapochromic response of $[Pt(Nttpy)Cl](PF_6)_2$ can discriminate between vapours of methanol, pyridine and acetonitrile.

As will be shown, **1—M** exhibits a vapochromic response that takes the form of a colour change to yellow for three solvents *viz.* acetonitrile, DMF and pyridine. A colour change to yellow is also observed when **1—M** is in contact with vapours of DMSO but, in this case, the response is irreversible and so is, strictly speaking, not a vapochromic one.

Nevertheless we include DMSO in the following discussion. Other solvent vapours that have been tested but which cause no visible change in colour are: methanol, acetone, tetrahydrofuran, chloroform, hexane, dichloromethane, diethyl ether, acetic acid, octan-1-ol, benzonitrile, nitrobenzene, formamide and toluene. Important to note, however, is that though these solvent vapours do not cause a change in colour on contact with **1—M**, their contact does not affect the intrinsic vapochromic properties of **1—M** in any way; provided, of course, the sample is dried *in vacuo* after exposure to the vapours. Furthermore, we note that VOCs which did not induce a colour change in **1—M** were not investigated further in respect of potential changes in their luminescent properties, i.e. emission spectra were only recorded for the acetonitrile, DMF, pyridine and DMSO solvates.

Two further points of clarity are made at this juncture:

The first is that the sample of **1—M** that we used for the vapochromic studies was obtained by grinding the original microcrystalline material in a matrix of KBr; to be precise to give a 1:5 w/w mixture of **1—M** in KBr. Eisenberg and co-workers applied the same procedure, simply because by grinding the average crystallite size is reduced, and hence the overall surface area is increased; this facilitates solvent vapour uptake and loss.[9] However, we wish to emphasise that the results obtained with the ground powder sample described in the following sections are duplicated when a microcrystalline, uncrushed sample of **1—M** is used, except in one respect: the response time is slower. Of course, the slower vapochromic response of the microcrystalline sample relative to that of the dispersed powder merely reflects the differences in the exposed surface area and the time taken for the vapours to penetrate the larger crystalline samples.

The second point of clarity is that in the following two sections we distinguish between *vapochromism* that is manifested by (i) changes in colour, i.e. in the wavelength of the transmitted light and (ii) changes in the emission spectrum. The latter is more accurately labelled as *vapoluminescence*. Of course, both kinds of the spectral change meet the requirements of an optical sensor.

5.5.2 Vapochromism

When a sample of **1—M** is exposed to vapours of acetonitrile, pyridine, DMF and DMSO, there is a dramatic change in colour from maroon to yellow: see Figure 2.17. Details with respect to the kinetics of the colour change are summarised in Table 2.3. Also given in the table are the approximate vapour pressures of each solvent at 298 K.

We first note that the colour change from maroon to yellow occurs very rapidly (< 10 s) when a sample of **1—M** is exposed to vapours of acetonitrile, pyridine and DMF; with DMSO the colour change is irreversible, which means that when **1—M** is exposed to DMSO its vapochromism is essentially destroyed. The time taken for the yellow solvated compounds of acetonitrile, pyridine and DMF to desolvate back to **1—M** varies from < 1 minute (for acetonitrile) to 15 days (for pyridine) under ambient conditions: see Table 2.3. However these desolvation times can be speeded up considerably by gently heating the (yellow) sample under vacuum. For example, the desolvation time for pyridine can be reduced from 15 to 4 days by using this procedure. Finally, note that the vapochromic response to acetonitrile, pyridine and DMF can be cycled endlessly, (at least ten times) without any chemical degradation of the sample.

Table 2.3 Volatile organic compounds that change the colour of **1—M** to yellow. Kinetic data are given as well as the approximate vapour pressure of each solvent at 298 K.

Volatile organic compound	Response time	Time taken to desolvate [a]	Vapour pressure at 298 K (torr) [b]
CH_3CN	< 10 seconds	< 1 minute	43
DMF	< 10 seconds	7 days (2 days)	2.7
C_6H_5N	< 10 seconds	15 days (4 days)	2.1
DMSO	< 10 seconds	irreversible	0.6

[a] This is the time taken when the solvated species is exposed to ambient conditions of temperature and pressure. If the sample of **1·solvent** is gently heated under vacuum the times are much reduced: see the values in brackets. [b] Vapour pressures taken from: S. Ohe, "*Computer-Aided Data Book of Vapour Pressures"*, Elsevier, New York, 1976.

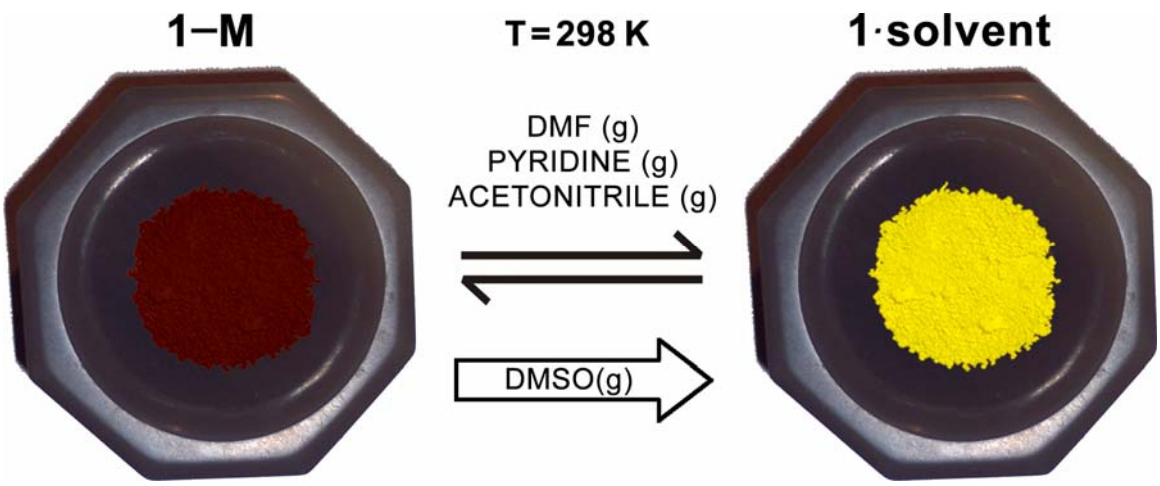

Figure 2.17 Photographs showing the transition from maroon to yellow when **1—M** is exposed to vapours of CH_3CN, C_6H_5N, DMF and DMSO.

5.5.3 Vapoluminescence

Figure 2.18 shows the room temperature solid state emission spectra recorded for **1—M** and each of the (yellow) pyridine, DMF and DMSO solvates. (We recognise that the DMSO solvate does not form part of the vapochromic cycle for **1—M** but show it for comparison purposes.) Also shown in the insert to Figure 2.18 is the emission spectrum of the acetonitrile solvate recorded at 77 K. As it turns out the acetonitrile solvate is non-emissive at room temperature.

As can be seen from Figure 2.18, the emission maxima for the solvated compounds are significantly blue-shifted to that of 687 nm for **1—M** itself. These energy differences are accompanied by significant differences in the emission intensities as well: see Table 2.4. We discuss the relevance of the emission data to the use of **1-M** as a thermochromic sensor in the next section. Here we discuss the reproducibility and reversibility of the emission responses shown in Figure 2.18. Obviously the response to DMSO is not reversible, as already discussed. On the other hand, the vapochromic response to acetonitrile, pyridine and DMF is fully reversible, i.e. exactly the same room temperature

spectra (non-emissive for the acetonitrile solvated compound) as those shown in Figure 2.18 are observed if the solvent exposure/ solvent removal cycle is repeated indefinitely.

Table 2.4 Photophysical data for **1—M** and the yellow solvated compounds.

Compound [a]	λ_{em}^{max} (nm)	Relative Intensity at 298 K [b]
1—M	687	1000
1·CH_3CN—Y	675 [c]	zero
1·DMF—Y	~ 625	~ 100
1·C_6H_5N—Y	550, 545sh	1300
1·DMSO—Y	600, 650sh	900

[a] We assume a 1:1 stoichiometry for the solvates because of the crystal structure determination of **1·CH_3CN-Y**; see Section 4 of this chapter. [b] The units of intensity are arbitrary. [c] Measured at 77 K.

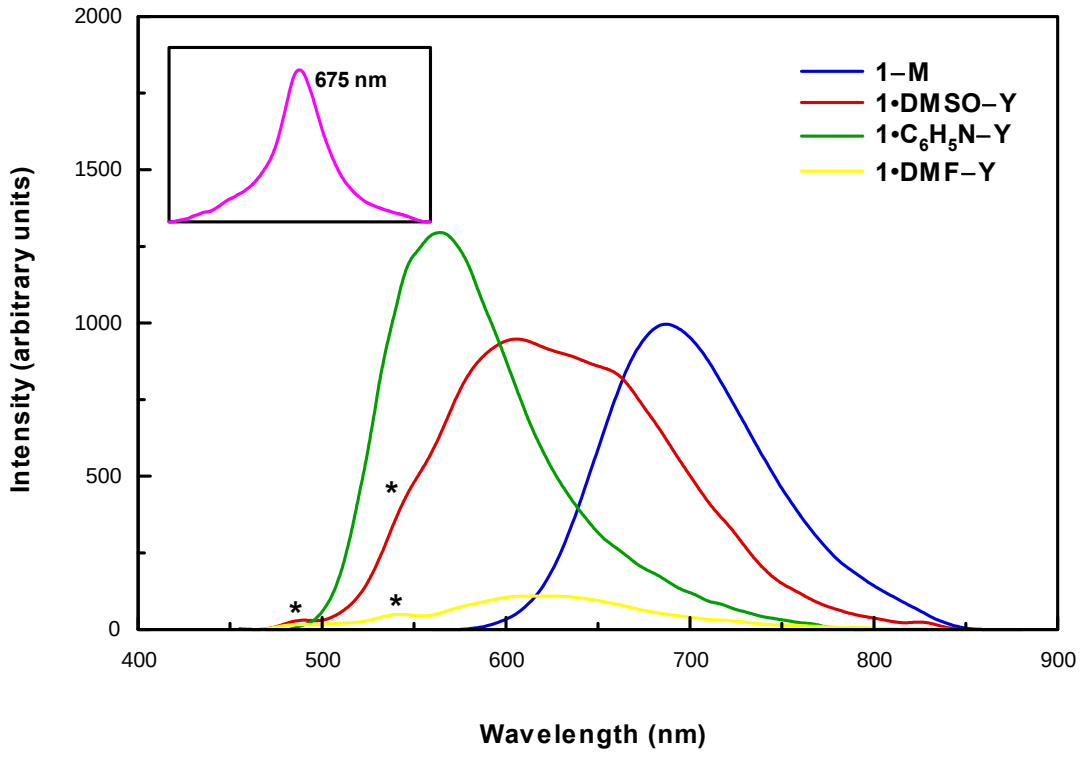

Figure 2.18 Solid state emission spectra recorded for **1—M,** and the yellow solvated forms with DMF, C_6H_5N and DMSO (all at 298 K). The insert shows the emission spectrum of the CH_3CN solvate recorded at 77 K: see text. The asterisks denote instrumental artifacts.

5.5.4 Concluding remarks

We assess first the effectiveness of **1—M** as a vapochromic sensor material. A major advantage is that the colour change from maroon to yellow is visually dramatic: see Figure 2.17. A major disadvantage is that **1—M** is rendered ineffective as a vapochromic sensor if exposed to vapours of DMSO. On the other hand, if DMSO is sorbed by the material, the colour does change from maroon to yellow and, more importantly, the emission spectrum is significantly different to that of **1—M** and the other solvates as shown in Figure 2.18. Thus DMSO would be detected and identified, albeit with a concomitant annihilation of the vapochromic properties of the material.

Setting to one side the problem with DMSO sorption, it is true to say that **1—M** exhibits a selective vapochromic response to just three of many solvents investigated, these being acetonitrile, pyridine and DMF; all of which are considered toxic. Moreover, though the colours of these three solvates are all yellow, their emission spectra are quite different, both in terms of $\lambda_{em}{}^{max}$ and the emission intensity: see Figure 2.18 and the data in Table 2.4. In fact, the emission response to acetonitrile acts as an "on-off" switch, given that **1—M** is a strong emitter whereas **1·CH_3CN—Y** does not emit at all at room temperature. In summary, **1—M** displays many of the requirements for an effective vapochromic optical sensor material.

We finally address the question of why there is a vapochromic response by **1—M** to certain VOCs but not to others. The problem in answering the question is that, unless a solvent vapour is sorbed in the first place, it cannot cause a change in colour. Thus, it is difficult to separate the issue of whether the vapour molecules are sorbed into the lattice or not, from whether, if they are sorbed, there is a concomitant colour change. Methanol is a case in point. Based on Eisenberg's work with the [Pt(Nttpy)Cl]$(PF_6)_2$ system,[9] it seems highly likely that the vapours of methanol are easily sorbed by **1—M**; after all methanol has a high vapour pressure and the molecule is small. But, there is no accompanying colour change, the implication being that the sorption of methanol

molecules into the lattice does not cause the kind of structural change that leads to a change in colour. In this respect, the introduction in Section 5.5.1 refers: previous studies of vapochromic platinum(II) compounds suggest that it is when the sorbed solvent molecules influence the metallophilic Pt◦◦◦Pt interactions that changes in colour occur. Clearly, this does not happen with methanol. With acetonitrile, pyridine and DMF it does happen, and reversibly. For these three solvents the colour change from maroon to yellow strongly implies that the extended chain motif of the platinum atoms in **1—M** is disrupted: how else would one explain the yellow colour? Indeed other workers have provided the same explanation for similar observations.[9,86-88]

We can be somewhat more quantitative with regard to rate of solvent loss as reflected by the data in Table 2.3. Acetonitrile is the most volatile solvent and has the smallest molecule; thus it comes as no surprise that the vapochromism of **1—M** towards acetonitrile is so facile. Also, as shown by the X-ray crystal structure of **1·CH_3CN—Y**, there is no obvious barrier to solvent molecule loss. Indeed, as discussed in Section 4 of this chapter and illustrated in Figure 2.7, when acetonitrile molecules are lost from the lattice, the formation of stabilising Pt◦◦◦Pt interactions is facilitated. Pyridine is more volatile than DMF, yet pyridine desolvation occurs more slowly than DMF desolvation. Perhaps this has to do with the fact that pyridine is a planar heteroatomic molecule that could intercalate between the π-stacked trpy ligands of **1—M;** if the binding constant for this type if interaction is quite high, then pyridine will not escape from the lattice easily. DMF, on the other hand, will not π-stack, thus precluding a stabilising π-π interaction. (We note in parentheses that DMF could, in principle, hydrogen bond to a fluorine atom of the hexafluoroantimonate anion.) However, without single crystal structure determinations, the above arguments must be regarded as speculation. Clearly, further studies are required to determine the factors that influence and control the vapochromic response in **1—M**.

3 Synthesis, characterisation, and solid state properties of [Pt{4'-(Ph)trpy}(NCS)]SbF_6 (compound 2)

1 Introduction

Unlike [Pt(trpy)(NCS)]SbF_6 (**1**), compound **2** does not change colour upon change in temperature or solvent loss/gain; in fact **2** and all of its solvates are yellow in colour. For this reason, the colour labelling scheme used in Chapter 2 does not apply in this chapter.

Previous work in our laboratories has focused on ionic platinum terpyridines with either the CN^- or Cl^- ion as the co-ligand; and where the terpyridyl ligand is substituted in the 4'-position by a phenyl group that is, itself, substituted in the *ortho*-position.[10,15,16,18,19,24,33] Thus complexes with ligands such as 4'-(*o*-$CH_3C_6H_4$)trpy, 4'-(*o*-$CF_3C_6H_4$)trpy and 4'-(*o*-ClC_6H_4)trpy were synthesised and structurally characterised.[10,15,16,18,19,24,33] It was believed that the loss of planarity of the trpy ligand due to the twist about the interannular bond (the bond between the central pyridine ring and 4'-phenyl ring) creates a lock-and-key mechanism between head-to-tail cations in the solid state; a mechanism which promotes the formation of single crystals. However crystallographic results from Chapter 2 suggest that the greater length of the SCN^- ion (as compared to the CN^- and Cl^- ions) and larger size of the non-bonded S atom would prevent such a mechanism, and therefore hinder single crystal formation. For this reason it was decided that a complex with the 4'-(Ph)trpy ligand (where the phenyl group is not substituted) would be investigated *viz.* [Pt{4'-(Ph)trpy}(NCS)]SbF_6. Interestingly, the 4'-(Ph)trpy ligand displays a wide range of interannular bond angles, with values ranging from 1.8 to 35.2° determined from crystal structures of ionic platinum terpyridines with the ligand.[10,16,24,33] It appears that the exact value of the interannular torsion angle depends on crystal packing effects.[10,16,24,33] As it turns out the choice of the 4'-(Ph)trpy ligand was fortuitous, not only in terms of obtaining single crystals, but also because

[Pt{4'-(Ph)trpy}(NCS)]SbF_6 (**2**) possesses an unusual crystal structure with open channels, i.e. the material is porous. We now briefly introduce the topic of metal-organic framework (MOF) crystal structures; these materials are important because, being porous, they can sorb gas phase molecules.

Decreasing international oil reserves, increasing pollution problems and a need for a more efficient energy production has resulted in the onset of the so-called "hydrogen economy".[102] With this, interest in materials viable for storage of gases has blossomed. Viable materials have been defined as those materials able to reversibly store 6 and 35 % by weight of hydrogen and methane respectively.[103] Prior to the pioneering work of Yaghi and Kitagawa,[104-107] discussions about so-called 'microporous' materials involved mainly traditional zeolite type materials.[105,106] Their more recent research is directed towards the development of materials that comprise the assembly of discrete units of inorganic metal clusters, coordination compounds or organic compounds into rigid framework structures, i.e. MOFs.[106(see references within)] Yaghi and co-workers showed that more success in terms of designed pore structure (size, shape and function) and porosity is possible if the material is constructed from numerous smaller molecules.[105,106] The discrete units (known as building blocks) assemble to give materials with well defined functions (modular materials).[106] The main difficulty with this approach is that it is very difficult to control or predict the way in which discrete units (building blocks) will pack so that a material with the desired packing characteristics is obtained.[105,106] A second difficulty is associated with the method typically used to ensure the generation of a *porous* material: this involves the synthesis of a solvated material and the subsequent removal of the solvent.[105,106] The premise is that, if the solvent can be removed without significantly disrupting the host lattice then, in all likelihood, solvent accessible space will be present in the lattice.[108] However, removal of solvent more often than not leads to a rearrangement to achieve close-packing, i.e. the pores are lost.[9,106,108-113] In fact, this is exactly what was observed when compound **1─M** was obtained by desolvation of **1·CH_3CN─Y**: as described in Chapter 2. Thus, in summary, **Metal-Organic Frameworks** (MOFs) are <u>crystalline</u> compounds consisting of assembled metal ions or clusters coordinated to often rigid organic molecules to form one-, two-, or three-

dimensional structures that can be porous. In some cases, the pores are stable to elimination of the guest molecules (often solvents) and can be used for the storage of gases such as hydrogen and carbon dioxide.

We now introduce a different kind of porous metal-organic material in particular one that is not formally described as a MOF material but which, nevertheless, is obtained through a desolvation process that does not lead to a loss of single crysallinity. The example is $[Ag_2\{1,4\text{-bis}(2\text{-methylimidazol-1-ylmethyl})\text{benzene}\}_2](BF_4)_2$, a compound that has been described by Barbour and co-workers as "A discrete metallocyclic complex that retains its solvent-templated channel structure on guest removal to yield a porous gas sorbing material";[108] in this instance the guest is a solvent (CH_3CN) of crystallisation. The solvent-templated channels possess van der Waals dimensions of ~ 4.9 x 7.5 Å, filling 22% of the total volume. Barbour proposes that the use of rigid exo-bidentate metal-ligand-metal bridges and rigid molecular rings favours the formation of porous materials as they confer rigidity to the crystal structure and pack inefficiently, and so promote the inclusion of a guest species within the crystal structure.[108]

In this chapter we report that when acetonitrile solvent of crystallisation is lost from single crystals of $[Pt\{4'\text{-(Ph)trpy}\}(NCS)]SbF_6\cdot CH_3CN$ (**2·CH$_3$CN**), single crystals of $[Pt\{4'\text{-(Ph)trpy}\}(NCS)]SbF_6$ (**2**) are obtained; and that **2** has an open, porous crystal structure. We also show, *via* single crystal X-ray diffraction studies, that compound **2** reversibly sorbs acetonitrile vapours without loss of single crystallinity. Compound **2** also sorbs methanol and acetone molecules without severe disruption of its open crystal structure. Of particular interest is that, though compound **2** and all of its solvates are yellow, there are differences in their emission spectra recorded at 80 K on microcrystalline powder samples. These differences are discussed with reference to the single crystal determinations of **2**, **2·CH$_3$CN**, **2·CH$_3$OH** and **2·(CH$_3$)$_2$CO**.

2 Synthesis and characterisation

The synthesis of [Pt{4'-(Ph)trpy}(NCS)]SbF_6 (**2**) follows the same procedure as that used for the synthesis of [Pt(trpy)(NCS)]SbF_6 (**1**). Thus, treatment of a solution of [Pt{4'-(Ph)trpy}Cl]SbF_6 in refluxing acetonitrile, with a 10% molar excess of silver thiocyanate affords *via* a metathesis reaction a precipitate of silver chloride and a solution of [Pt{4'-(Ph)trpy}(NCS)]SbF_6 (**2**). After removal of the AgCl by cannular filtration, the solution of **2** is concentrated to near saturation by removal of solvent *in vacuo*. Recrystallisation by diffusion of diethyl ether into the above concentrated solution of the yellow solid in acetonitrile affords a bright-yellow, polycrystalline material; in fact the material contains single crystals of the acetonitrile solvate, [Pt{4'-(Ph)trpy}(NCS)]$SbF_6 \cdot CH_3CN$ (**2·CH₃CN**) as confirmed by a single crystal X-ray structure determination: see the CIF file, **2MeCN_1st.cif**, in the Supporting Information on the CD attached to the back inside cover of the thesis. These crystals slowly (7-10 days) lose their acetonitrile solvent of crystallisation when exposed to air, finally affording yellow crystals of [Pt{4'-(Ph)trpy}(NCS)]SbF_6 (**2**). (Note that, unlike **1·CH₃CN─Y**, single crystals of **2·CH₃CN** transform into single crystals of **2** that have the same indistinguishable yellow colour.)

The empirical formulation of [Pt{4'-(Ph)trpy}(NCS)]SbF_6, i.e. $C_{22}H_{15}N_4F_6PtSb$ was confirmed by microanalysis for %C, H and N. The infrared spectrum recorded as a KBr pellet exhibits a strong sharp peak at 2 102 cm^{-1} assigned to the ν(SC≡N) stretching mode and a weaker, somewhat broader peak at 866 cm^{-1}, due to the ν(S−CN) stretching mode. These stretching frequencies both occur at similar energies to those recorded for compound **1** of 2097 and 874 cm^{-1} respectively, and are consistent with an N-bound SCN^- ion.[60-63] Other peaks in the spectrum are common to platinum terpyridines, in particular the peaks between 1 610 and 880 cm^{-1}, the fingerprint region for the 4'-(Ph)trpy

ligand.[10,16,24,33] The various infrared stretching frequencies and their assignments are listed in Section 3.3 of Chapter 4. A ^{1}H NMR spectrum of **2** was recorded in CD_3CN where the signals where sufficiently well resolved to assign resonances: GHSQC and GHMQC NMR experiments were performed to aid in the assignment of the peaks. The various resonances and their assignments are also listed in Section 3.3 of Chapter 4. Note that these are listed only for the N-bound isomer that dominates in CD_3CN: see the discussion in the next section where we describe the ^{13}C and ^{15}N spectra of the "Pt^{15}N^{13}CS" unit obtained by using a ^{13}C and ^{15}N enriched sample of **2**, i.e. [Pt{4-(Ph)trpy}(^{15}N^{13}CS)]SbF_6. Mass spectrometry has also been performed on **2**, the results of which are in excellent agreement with the isotopic predications showing a [Pt{4'-(Ph)trpy}(NCS)]$^{2+}$ peak at m/z= 562.0670. Finally, we also list in Section 3.3 of Chapter 4 the UV/vis absorption data measured for [Pt{4'-(Ph)trpy}(NCS)]SbF_6 in acetonitrile; the absorption spectrum is shown in Figure S2 in the Supporting Information on the CD attached to the inside back cover of the thesis.

3 Speciation of [Pt{4'-(Ph)trpy}(NCS)]$^+$ in fluid solution

3.1 Introduction

The [Pt{4'-(Ph)trpy}(NCS)]$^+$ cation is distinguished from the [Pt(trpy)(NCS)]$^+$ cation by the substitution of a phenyl group in the 4'-position of the trpy moiety. This will extend the delocalisation of π-electron density from the trpy moiety to the phenyl group assuming, of course, that the phenyl group and the trpy moiety are approximately co-planar. (They are in the solid state: see the crystal structure determinations described in the next section.) This extended π-delocalisation will have an effect on the electron density on the Pt atom; in the language of Pearson's Hard and Soft Acid and Base theory the hardness/softness of the platinum in the +2 oxidation state will be modified.[65] The point is that the deductions made in Section 3 of Chapter 2 regarding the mode of coordination of the SCN^- ion in [Pt(trpy)(NCS)]$^+$ cannot be automatically transferred to the [Pt{4'-(Ph)trpy}(NCS)]$^+$ cation. Thus, we have carried-out ^{13}C and ^{15}N NMR studies of the speciation of [Pt{4'-(Ph)trpy}(NCS)]$^+$ in acetonitrile as well; these are described in

Section 3.2 below. In fact, a ^{1}H NMR spectrum recorded at room temperature in CD_3CN of [Pt{4'-(Ph)trpy}(NCS)]SbF_6 (**2**) shows a set of signals easily assigned to the protons of the trpy ligand, but with each (major) peak in the spectrum being "shadowed" by a far less intense satellite peak. Thus, as for the [Pt(trpy)(NCS)]$^+$ cation, we suspected that both the N-bound and S-bound isomers of the SCN^- ion co-exist in equilibrium in acetonitrile solutions of **2**. The question is of course: "What is the relative proportion of the two isomers and is it the same as for the [Pt(trpy)(NCS)]$^+$ cation?"

For reasons already given in Section 3.1 of Chapter 2 and using the same approach, we have synthesised and purified the isotopically enriched compound, [Pt{4'-(Ph)trpy}(^{15}N^{13}CS)]SbF_6. An infrared spectrum of the compound, recorded as a KBr disc, shows peak positions for the ν[S^{13}C≡^{15}N] and ν[S–^{13}C^{15}N] stretching frequencies that are exactly as expected if isotopic substitution has occurred: see Section 3.4 of Chapter 4.

Finally, note that the ^{13}C and ^{15}N NMR spectra discussed in the following section were all recorded using our in-house 500 MHz Bruker Avance III spectrometer. As previously discussed, this has implications for the quality of the ^{15}N NMR spectra, especially in respect of a poor signal-to-noise ratio. Nevertheless, an analysis of the ^{13}C and ^{15}N NMR spectra allows for reliable conclusions to be drawn regarding the mode of coordination of the S^{13}C^{15}N$^-$ ion in [Pt{4'-(Ph)trpy}(^{15}N^{13}CS)]$^+$; especially as the conclusions are supported by the NMR data recorded for [Pt(trpy)(NCS)]$^+$ that are discussed in Section 3.2 of Chapter 2.

3.2 ^{13}C and ^{15}N NMR studies of the "Pt^{15}N^{13}CS" unit in [Pt{4'-(Ph)trpy}(NCS)]$^+$

The ^{13}C NMR spectrum recorded in CD_3CN at room temperature of [Pt{4'-(Ph)trpy}(^{15}N^{13}CS)]SbF_6 is shown in Figure S3 in the Supporting Information on the CD attached to the inside back cover of the thesis; the spectrum is essentially the same as the ^{13}C NMR spectrum recorded for [Pt(trpy)(^{15}N^{13}CS)]SbF_6 that is shown in Figure 2.1 in Chapter 2. Thus, exactly the same analysis applies. Of particular interest

is the ratio of the integrated intensity of the more intense downfield signal to the less intense upfield signal: again this is within experimental error the same as for the parent [Pt(trpy)(NCS)]$^+$ cation and, therefore, we conclude that ~ 95% of the [Pt{4'-(Ph)trpy}(NCS)]$^+$ cation exists in acetonitrile as the N-bound isomer, with about 5% of the S-bound isomer in equilibrium with it.

The ^{15}N NMR spectrum recorded in CD_3CN at room temperature of [Pt{4'-(Ph)trpy}(^{15}N^{13}CS)]SbF_6 is shown in Figure S4 in the Supporting Information on the CD attached to the inside back cover of the thesis. The signal-to-noise ratio is not high enough for coupling of ^{15}N to ^{195}Pt to be observed, i.e. the doublet of doublets discernable in the signal for the major (N-bound) isomer of [Pt(trpy)(^{15}N^{13}CS)]$^+$ is hidden in the background. Nevertheless, the spectrum is in all other respects the same as that shown in Figure 2.2 of Chapter 2 and, therefore, we draw the conclusion: the N-bound and S-bound isomers of the SCN$^-$ ion co-exist in acetonitrile solutions of the [Pt{4' (Ph)trpy}(NCS)]$^+$ cation, but the N-bound isomer is dominant with only a small percentage of the S-bound isomer being present.

3.3 Concluding remarks

We summarise in Tables 3.1 and 3.2 below all the parameters that define the ^{13}C and ^{15}N NMR spectra, respectively, recorded in CD_3CN for compounds **1** and **2**. As already discussed, these lead to the conclusion that the speciation of the [Pt(trpy)(NCS)]$^+$ and [Pt{4'-(Ph)trpy}(NCS)]$^+$ cations is the same in acetonitrile solution, i.e. ~ 95% of the cations has the SCN$^-$ ion N-bound as the isothiocyanate ligand, and ~ 5% of the cations are present with the SCN$^-$ ion bound through the S atom as the thiocyanate ligand. Obviously, there is a dynamic equilibrium between the two isomers that could be investigated *via* variable temperature NMR studies; but such an investigation will have to form part of further work. (We also note in parentheses that the NMR parameters in Tables 3.1 and 3.2 are only consistent with the two possible *terminal* ligations of the SCN$^-$ ion; were the ion to bridge two Pt atoms a more complicated set of parameters would be obtained.)

Table 3.1 ^{13}C NMR spectroscopic data of the "Pt^{15}N^{13}CS" unit for [Pt{4'-(Ph)trpy}(^{15}N^{13}CS)]$^+$ and [Pt(trpy)(^{15}N^{13}CS)]$^+$ recorded in CD_3CN at 303 K; and for S^{13}C^{15}N$^-$ in an acetonitrile solution doped with ammonia also at 303 K. Chemical shifts are referenced to the solvent, CD_3CN.

Compound in solution	Signal	^{13}C spectral data		
		ppm	$^1J(^{13}C^{15}N)$ [Hz]	$^2J(^{13}C^{195}Pt)$ [Hz]
[Pt(trpy)(NCS)]$^+$	Major	135.2	33	115
	Minor	116.1	11	~ 25[a]
[Pt{4'-(Ph)trpy}(^{15}N^{13}CS)]$^+$	Major	135.6	33	116
	Minor	116.7	11	n/a[b]
S^{13}C^{15}N$^-$	-	128.6	13	-

[a] The value is an approximation, as the doublet of doublets is poorly resolved for the minor species: see Figure 2.1 in Section 3.1 of Chapter 2.[b] relevant data is *not available*.

Table 3.2 ^{15}N NMR spectroscopic data of the "Pt^{15}N^{13}CS" unit for [Pt{4'-(Ph)trpy}(^{15}N^{13}CS)]$^+$ and [Pt(trpy)(^{15}N^{13}CS)]$^+$ recorded in CD_3CN at 303 K; and for S^{13}C^{15}N$^-$ in an acetonitrile solution doped with ammonia also at 303 K. Chemical shifts are referenced to ammonia.

Compound in solution	Signal	^{15}N spectral data		
		ppm	$1J(^{13}C^{15}N)$ [Hz]	$^nJ(^{15}N^{195}Pt)$ [Hz]
[Pt(trpy)(NCS)]$^+$	Major	101.6	33	293 (n = 1)
	Minor	250.8	11	n/a
[Pt{4'-(Ph)trpy}(^{15}N^{13}CS)]$^+$	Major	102.2	33	n/a
	Minor	250.7	11	n/a
S^{13}C^{15}N$^-$	-	215.6	12.6	-

We now address the question of why the N-bound isomer dominates in acetonitrile solution. The N-bound isothiocynanate ligand is a strong π-donor and a weak π-acceptor ligand.[66] The S-bound thiocyanate ligand is a weak π-donor and a strong π-acceptor ligand.[66] Clearly, the N-bound ligand will most strongly bind to a metal atom that is low on electron density whereas the opposite will be true for the S-bound ligand; the latter needs high electron density on the metal to stabilise the M─SCN bond *via* π-back donation. The electron density on a platinum atom in the +2 oxidation state is inevitably

lowered if the Pt atom is bonded to a terpyridyl ligand: because the trpy ligand acts as a strong π-acceptor ligand *via* back donation of electron density on the metal into the low energy π*-orbitals that are delocalised over the three linked pyridine rings. Thus, if the SCN^- ion binds through the S-atom it would have to compete with the trpy ligand for electron density on the metal atom. On the other hand, since the N-bound ligand is a π-donor, the presence of the trpy ligand would actually reinforce the strength of the M─NCS bond. The expectation must therefore be that for the complexes studied, the thermodynamically favoured isomer will be the N-bound isothiocyanate ligand. Thus, we have the expected result. Indeed, other workers have shown that the mode of coordination of the SCN^- ion to a Pt(II) centre is critically dependent on the donor/acceptor abilities of the other ligands bonded to the Pt atom.[60-62,72,114] If these other ligands are strong donors then the S-bound isomer is favoured, whereas if the other ligands (like trpy) are π-acceptor ligands then the N-bound isomer is favoured.[60,62,66] Other workers have also shown that the ratio of linkage isomers present in solution is dependent on the polarity of the solvent.[67-69] In this context we note that during the course of the characterisation of compounds **1** and **2**, their ^{1}H NMR spectra were also recorded in DMSO-d_6; interestingly the same pattern of strong signals, each accompanied by a much smaller satellite peak is observed. Thus, it would appear that both linkage isomers also co-exist in DMSO solutions of the [Pt(trpy)(NCS)]$^+$ and [Pt{4'-(Ph)trpy}(NCS)]$^+$ cations.

The fact that the [Pt{4'-(Ph)trpy}(NCS)]$^+$ cation exists in solution as two different linkage isomers in equilibrium with each other presents a dilemma in so far as the proposed work on complex **2** is concerned. In the normal course of events we would continue with a study of the photophysics in fluid solution of the [Pt{4'-(Ph)trpy}(NCS)]$^+$ cation; after all it is new. However, with two species in solution, each with a different excited state manifold, such an investigation would not be useful. To illustrate the point consider the absorption spectrum of the cation shown in Figure S2 in the Supporting Information on the CD attached to the inside back cover of the thesis. Close examination of the long wavelength region of 350-450 nm suggests the presence of at least 3 peaks. These are all

^{1}MLCT absorptions that can only be understood if there is more than one species in solution. We have also recorded the emission spectrum of $[Pt\{4'\text{-(Ph)trpy}\}(NCS)]^+$ cation in acetonitrile and dichloromethane; it is quenched in the former solvent and in DCM there is clear evidence for overlapping emission from two different species.

Fortunately there is no problem in the solid state in so far as the mode of coordination of the SCN^- ion is concerned. It is invariably and exclusively bound to the Pt atom through the N atom in the crystal structures described in this thesis. It is important to note that this is entirely as expected. After all, if the thermodynamically favoured isomer in solution is the N-bound one, the thermodynamically stable product in the solid state must be where the SCN^- ion is bound to the Pt atom through the N atom; as discussed in Section 2 of Chapter 1.

4 Crystal structures of $[Pt\{4'\text{-(Ph)trpy}\}(NCS)]SbF_6$ (2) and of $[Pt\{4'\text{-(Ph)trpy}\}(NCS)]SbF_6$·solvent (2·solvent, where solvent = acetonitrile, methanol or acetone)

Single crystals of **2**, **2·CH_3CN**, **2·CH_3OH** and **2·$(CH_3)_2CO$** are all yellow, needle-shaped and belong to the space group $P2_1/n$, with four formula units in the unit cell. The X-ray crystallography is described in Section 8.1 of Chapter 4 and the crystal data are summarised in Table 4.1 at the end of Chapter 4. How these single crystals were obtained will first be described, along with an explanation of the choice of temperature for the intensity data collections.

The crystal of **2** was selected from the batch of crystals first isolated from the crystal growth chamber as the solvate (**2·CH_3CN**) but then allowed to lose their solvent of crystallisation, as described in Section 2 earlier in this chapter. The X-ray intensity data for **2** were collected at 200 K, for reasons given below.

The single crystal of **2·CH_3CN** was obtained using the *same single crystal* of **2**, and exposing it to vapours of acetonitrile using the technique described in Section 6.1 of Chapter 4. For the purposes of the intensity data collection, this crystal was cooled in order to slow down the potential loss of solvent. (At this point we note that the crystal was not coated in a protective layer such as paratone, because our intention was to check whether this crystal of **2·CH_3CN** would lose solvent without loss of its single crystallinity: see Section 4.3 later in this chapter.) A temperature of 200 K was used for the data collection. This temperature is a compromise; we wished to lower the temperature as far as possible so as to slow down solvent loss and maximise the quality of the intensity data, but we discovered that cooling a single crystal of **2·CH_3CN** below 200 K caused the crystal to crack under the mechanical stress. In fact, when a single crystal of the desolvated compound, **2**, is cooled below 200 K it also cracks; an unsurprising result given the presence of open solvent channels within a rigid crystal packing arrangement: see Sections 4.1 and 4.2 below.

The single crystal of **2·CH_3OH** was obtained by taking a *different* single crystal of **2** from the original batch, and exposing it to methanol vapours using the technique described in Section 6.1 of Chapter 4. In this case the crystal could be safely cooled to 180 K – the temperature used for the data collection.

Exposure of a single crystal of **2** to vapours of acetone does not proceed without some loss of single crystallinity: see Section 6.1 of Chapter 4 for the details of the experiment. For this reason, the single crystal of **2·$(CH_3)_2CO$** was obtained directly by vapour diffusion of diethyl ether into a concentrated solution of **2** in acetone. This "good quality" crystal could be safely cooled to 200 K – the temperature used for the data collection. (We note in parentheses that the crystal of **2·$(CH_3)_2CO$** obtained by exposure of a single crystal of **2** to vapours of acetone was of sufficient quality to allow for a structure solution, albeit an inaccurate one; and that the atom positions determined match those obtained with the "good quality" crystal: see Section 4.3 below for further discussion in this regard.)

4.1 Crystal structure of [Pt{4'-(Ph)trpy}(NCS)]SbF_6 (2) at 200 K

Figure 3.1 shows a perspective view of the cation as well as the atom labelling scheme. A list of important interatomic distances and angles of the cation is given in Table 3.3. The coordination geometry of the central Pt atom is irregular square planar as evident in N1─Pt─N2 and N2─Pt─N3 bond angles of 80.7(1) and 81.3(1)° respectively, as well as in a "trans" N1─Pt─N3 angle of 162.1(1)°. This is typical of terpyridyl ligand complexes of platinum(II) and arises from geometric constraints imposed by the tridentate ligand.[3,6,9,10,12,15,16,18,19,22-24,28,29,33-35] Also typical of such complexes (and enforced by the geometry about Pt) is a shorter Pt to bridgehead nitrogen (N2) distance of 1.925(3) Å, as compared to the distances to the outer nitrogen distances of 2.022(4) (N1) and 2.019(4) Å (N3). The bond lengths and angles reported above are similar to those reported for [Pt{4'-(Ph)trpy}(CN)]BF_4·CH_3CN,[33] [Pt(trpy)(NCS)]SbF_6·CH_3CN (Section 4 of Chapter 2), [Pt{4'-(Ph)trpy}Cl]SbF_6·CH_3CN[10], [Pt(trpy)(CH_3CN)](SbF_6)$_2$[34] and both polymorphs of [Pt{4'-(Ph)trpy}(CN)]SbF_6·CH_3CN.[24] The terpyridyl moiety is essentially planar with a maximum deviation of any one atom from the mean plane through the non-hydrogen atoms of 0.13 Å (for C20).

Table 3.3 Selected interatomic distances and angles for the cation in **2** at 200 K.

Distances (Å)		Angles (°)	
Pt─N1	2.022(4)	N1─Pt─N2	80.7(1)
Pt─N2	1.925(3)	N1─Pt─N3	162.1(1)
Pt─N3	2.019(4)	N1─Pt─N4	98.9(1)
Pt─N4	2.023(4)	N2─Pt─N3	81.3(1)
N4─C22	1.098(6)	N2─Pt─N4	179.6(2)
C22─S	1.629(5)	N3─Pt─N4	99.0(2)
		Pt─N4─C22	173.1(4)
		N4─C22─S	179.5(5)

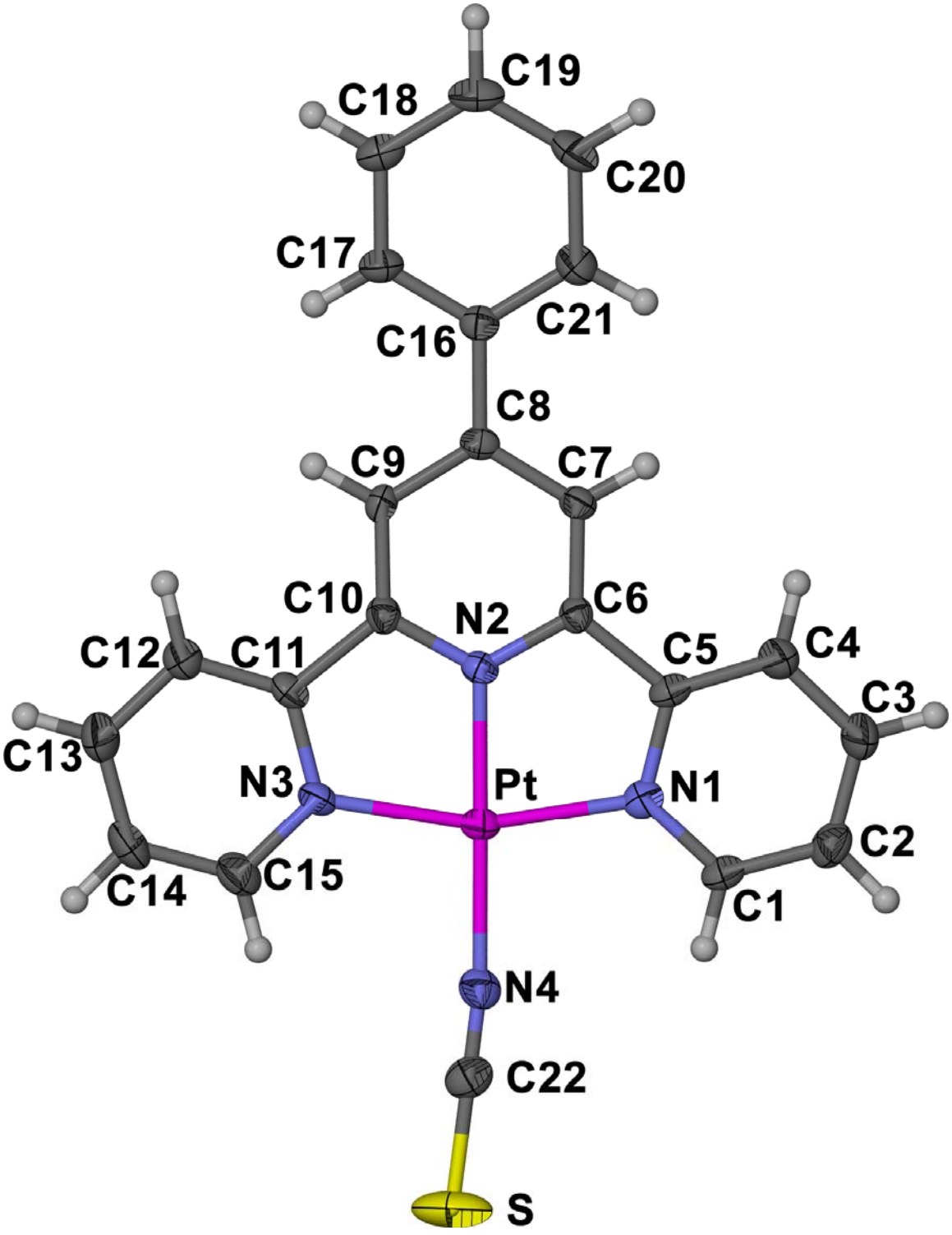

Figure 3.1 Frontal view of the cation in **2** drawn using the 200 K intensity data. Thermal ellipsoids (50%) are shown for all atoms except the hydrogens, which are shown as spheres of arbitrary radius.

There is only a small twist about the C8─C16 interannular bond as reflected in a C7─C8─C16─C17 torsion angle of 2.5°. This value is much smaller than those reported for the free ligand, (10.9°)[116] *red* [Pt{4'-(Ph)trpy}CN]SbF_6·CH_3CN (21.8 and 35.2°)[24] and [Pt{4'-(Ph)trpy}Cl]SbF_6·CH_3CN (33.4 and 33.3°)[10]; but similar to that measured for the *yellow* polymorph of [Pt{4'-(Ph)trpy}CN]SbF_6·CH_3CN (2.0 and 1.8°)[24] and [Pt{4'-(Ph)trpy}(CN)]BF_4·CH_3CN (2.1 and 1.9°)[33]. As a result the *cation as a whole is approximately planar*, which has implications for how the cations stack in the crystal structure: see the discussion later in this section.

The SCN^- ion is N-bound as the isothiocyanate ligand and nearly linear with Pt─N4─C22 and N4─C22─S bond angles of 173.1(4) and 179.5(5)° respectively. Interestingly the bend at N4 is such that the S atom is positioned close (< 0.08 Å) to the mean plane drawn through all the non-hydrogen atoms of the cation; consistent with our description of the cation as nearly planar. Analysis of the crystal structures of other isothiocyanate complexes reveals that there is a considerable variation in the angle formed by the M─N─CS bond angle; with values ranging from ~ 138°(in bis(2,2':6',2"-terpyridine)-tris(isothiocyanato)-praseodymium)[78] to ~ 177° (in bis(2,2':6',2"-terpyridine)-tris(isothiocyanato)-neodymium·ethanol solvate).[78] Changes in this bond angle are most likely a result of crystal packing effects; and is illustrated by comparing the Pt─N─CS bond angles determined for compounds **1·CH_3CN─Y** and **2** which are ~ 3° different. In contrast the N─C─S linkages are always linear (or very nearly linear) for the same set of complexes, e.g. the N─C─S bond angles for compounds **1·CH_3CN─Y** and **2** are the same within experimental error: compare the data in Tables 2.1 and 3.3. The N4─C22 and C22─S1 bond lengths are similar to those reported for other complexes containing the isothiocyanate ligand and terpyridine type ligand.[74-83] The Pt─N4 bond length of 2.023(4) Å is somewhat longer than the equivalent Pt─NCS distance of 1.998(3) Å measured for **1·CH_3CN─Y**, and 1.989(7) and 1.985(8) Å reported for [Pt(bipy)(NCS)2].[64] Interestingly in contrast to **1·CH_3CN─Y**, the Pt─N4 distance is longer than the Pt─$N_{bridgehead}$ distance but similar to the distances of the Pt atom to the outer N atoms: see data in Table 3.3

We now address the question of how the $[Pt\{4'\text{-}(Ph)trpy\}(NCS)]^+$ cations and SbF_6^- anions are arranged in the crystal, i.e. the crystal packing. A view down the [c]-axis of the unit cell contents is given in Figure 3.2; note by taking a view down the [c]-axis we are viewing the cations along a line that is near perpendicular to the mean plane through the non-hydrogen atoms comprising each cation; this plane will be referred to as the "cation plane". The first observation is that (unlike for **1·CH$_3$CN—Y**, see Figure 2.4) the cations do *not* stack in separate columns. Thus, in order to understand the crystal packing we have to take a different view of the arrangement of cations. To this end, we show in Figure 3.3, a view closely parallel to the cation planes, i.e. *perpendicular* to the [c]-axis and, specifically along the (long) [b]-axis. A second view of the crystal packing is provided in Figure 3.4 where a view perpendicular to the [c]-axis is again shown but, in this case, along the (shorter) [a]-axis.

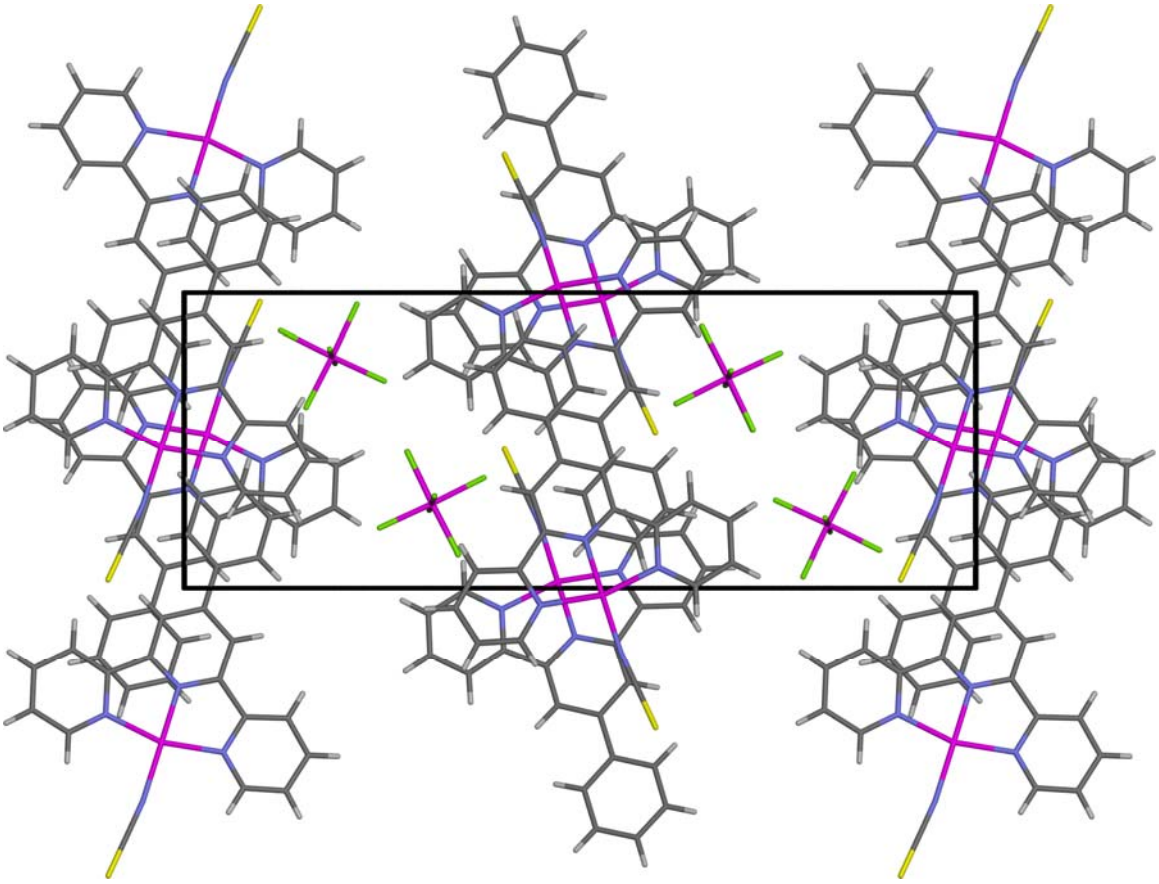

Figure 3.2 View down the [c]-axis showing the unit cell contents of **2**. The [b]-axis points downwards.

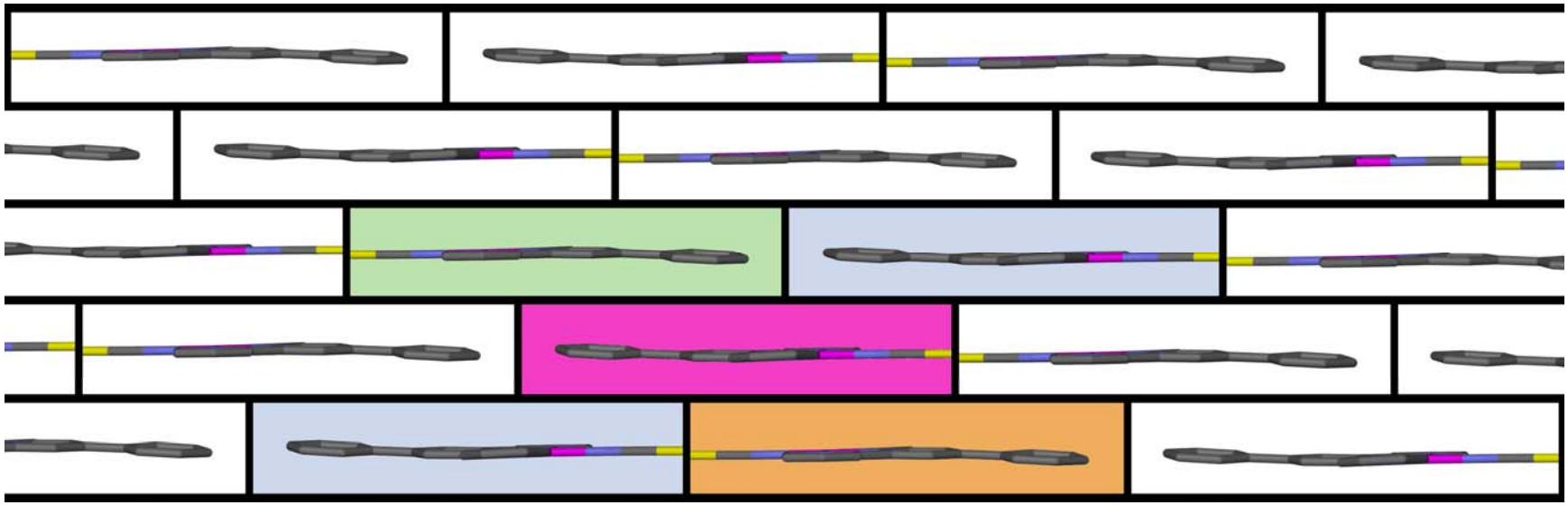

Figure 3.3 Diagram showing the "brick in wall" packing arrangement of the cations in **2**. Hydrogen atoms and hexafluoroantimonate anions have been omitted for clarity. Consider the central pink coloured cation "brick". Note how this cation overlaps with four other cations, two above and two below the cation plane. Of the two above, one is a co-directional and the other anti-directional; similarly one of the cations in the layer below is orientated in the same direction as the "pink" cation while the other points in the opposite direction. (Clearly the above distribution is true of any one cation in the above arrangement.) Those cations that overlap with the "pink" cation are colour coded according to the Pt∘∘∘Pt distance that links them to the "pink" cation. Orange indicates the short Pt∘∘∘Pt distance of 3.553 Å; green indicates that the overlapping cation is separated by the longest Pt∘∘∘Pt distance of 11.757 Å; and light blue indicates overlapping cations that point in the same direction with a Pt∘∘∘Pt separation of 9.616 Å.

Examination of Figure 3.3 leads to the following description of the arrangement of cations in crystals of **2**. Each cation (specifically its van der Waals envelope) can be seen as a "flat brick", and these bricks slot together to give a "wall", whose thickness corresponds to the width of a cation; essentially the diagram shown in Figure 3.3 represents part of near infinite number of overlapping cations that comprise such a wall. These walls repeat at half intervals along the [b]-axis with the hexafluoroantimonate anions between them: see Figure 3.2.

In describing the pattern of bricks in the wall we focus initially on one brick, in particular the cation "brick" that is coloured pink in Figure 3.3. This brick has adjacent cations on either side that are near co-planar; to be specific the cation on the left has its cation plane about 0.50 Å above that of the pink cation; while the cation on the right has its plane about 0.33 Å below that of the central pink cation. This "slightly above and slightly below" sequence extends throughout wall along the layer of bricks defined by the pink cation. Next, we examine the disposition of the bricks above and below the pink one. Altogether four cations overlap with this central pink cation: there are two above in the next layer, coloured green and blue; and two below, coloured blue and orange. The colours are chosen to emphasise the nature of the various overlaps that are discussed in detail below. Continuing with the description of the overall crystal packing we now refer to Figure 3.4. Unlike the cations within a wall, the cations of adjacent walls are not co-planar with each other. Rather there are alternating angles of +9.3 and −9.3° formed by the intersection of the cations planes leading to a "wave like" pattern when the walls are viewed in cross-section.

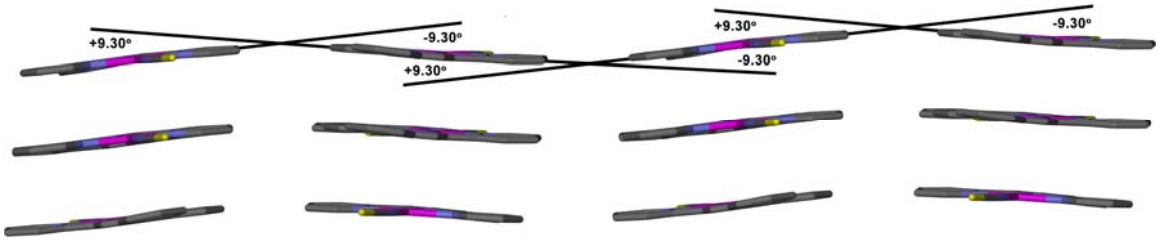

Figure 3.4 Cross-section of four cation "walls" illustrating the wave-like arrangement of adjacent walls. This view is perpendicular to the [c]-axis and taken along the [a]-axis.

We now examine the various intercation overlaps in some detail, first with respect to Figure 3.3. The Pt∘∘∘Pt distances that link the pink-to-orange and pink-to-blue cations (where the orange and blue cations are in the layer below) are 3.553 and 9.616 Å. The Pt∘∘∘Pt distances that link the pink-to-green and pink-to-blue cations (where the green and blue cations are in the layer above) are 11.757 and 9.616 Å. Note that the way in which the upper blue cation overlaps with the pink cation is identical to the way in which the pink cation overlaps with blue cation in the lower layer, i.e. the Pt∘∘∘Pt distances are the same; thus there are two cations coloured blue in Figure 3.3. None of these distances is less than the upper distance limit of 3.5 Å for finite d_{z^2}(Pt)-d_{z^2}(Pt) orbital interactions.[47] However, the three Pt∘∘∘Pt distances help define three distinct types of π(trpy)-π(trpy) interactions: these are labelled "A", "B" and "C" in Figure 3.5, shown on a separate page. The colours used to illustrate the nature of the various overlaps in Figures 3.3 correspond to the coloured lines used to border the same overlaps when viewed perpendicular to the cation planes in Figure 3.5, i.e. the green line which borders the overlapping cations in Figure 3.5(A), indicates that these are the green and pink cations shown in Figure 3.3. Note that the pink cation is not highlighted in Figure 3.5(A), (B) or (C) since it is presence is implied by its selection as the central reference point for the description of the other four overlapping cations: see Figure 3.3.

With regard to Figure 3.5(A) we see that the cations are orientated head-to-tail, exactly, so that there is a crystallographic centre of inversion midway between them. There is also a centre of inversion midway between the two cations shown in Figure 3.5(B); but the cations shown in Figure 3.5(C) are orientated head-to-head and are linked by a crystallographic *n*-glide. All three kinds of π(trpy)-π(trpy) overlap are of the parallel offset type that was discussed in Section 1.3.2 of Chapter 1 as net stabilising. In particular, the electron rich nitrogen atoms of adjacent cations are far apart; and trpy and/or phenyl carbon atoms are positioned opposite "holes" roughly in the middle of adjacent aromatic rings. This concludes a simple description of the crystal structure of **2**. Later, in Section 4.3, we describe the location of the open solvent channels (320 $Å^3$ per unit cell at 200 K) in crystals of **2**; also we assess further the porous crystal structure of **2**. We use this approach since it allows us to first discuss the crystal structures of the solvated species.

However, we note at this stage that there are no previous reports of a crystal structure of an ionic platinum terpyridine compound with the cations arranged as they are in crystals of **2**. In fact, whatever the choice of co-ligand and substituent in the 4'-position of the trpy ligand, it is far more common to find discrete stacks of cations and anions in crystals of an ionic platinum terpyridine: see refs 3,6,9,10,12,15,16,18,19,22-24,28,29,33,35 and 51.

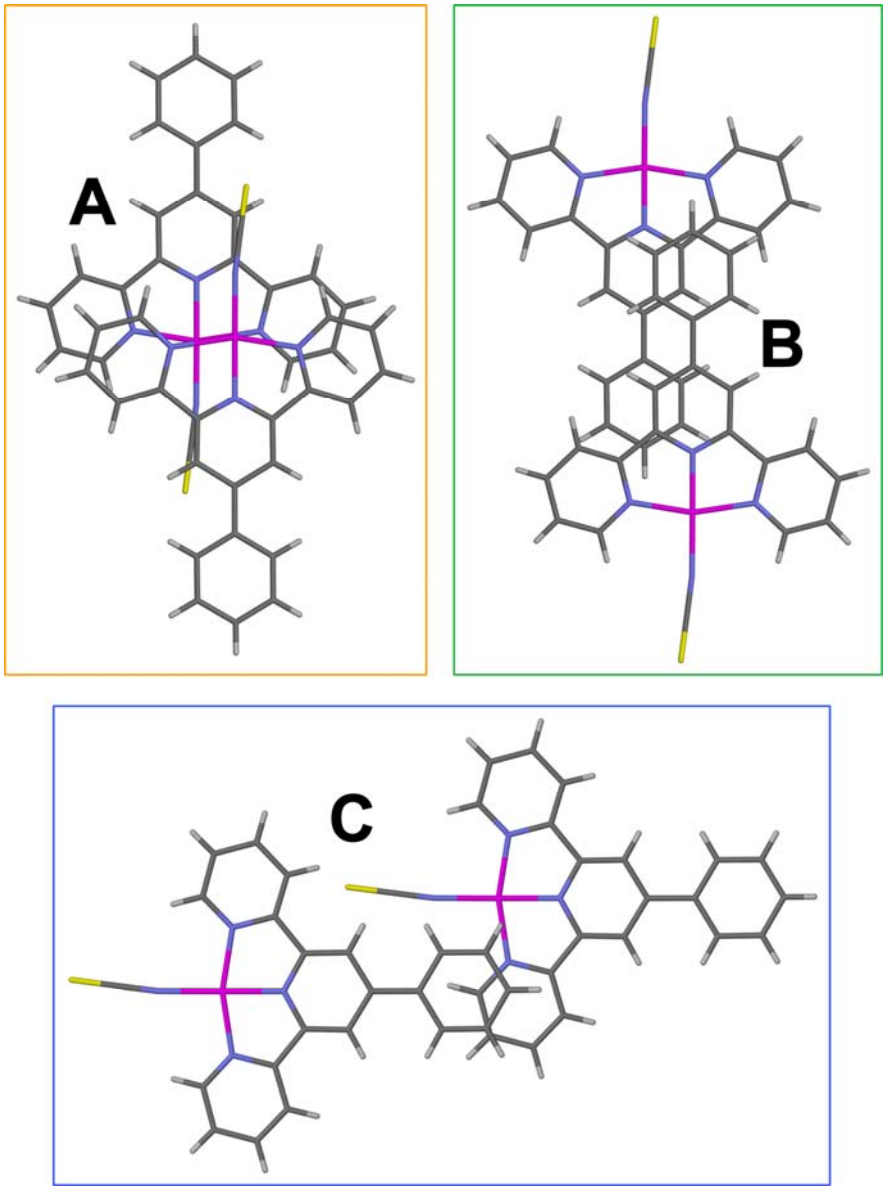

Figure 3.5 Views perpendicular to the mean plane of cations: separated by the (A) short and (B) long Pt◦◦◦Pt distances; illustrating the cation-cation overlap. Figure 3.5(C) is a view perpendicular to the mean plane of the overlapping cations which point in the same direction.

4.2 Crystal structures of 2·CH_3CN (at 200 K), 2·CH_3OH (at 180 K) and 2·$(CH_3)_2CO$ (at 200 K)

4.2.1 Geometry of the $[Pt\{4'\text{-}(Ph)trpy\}(NCS)]^+$ cation

There are no significant changes in the bond distances and angles for the cations in **2·CH_3CN**, **2·CH_3OH** and **2·$(CH_3)_2CO$** as compared to those reported in Table 3.3 for the cation of the parent compound, **2**; for this reason we do not discuss them further here. However, there are small but significant changes to the internal geometry of the cation, bought about by the inclusion of solvent molecules in the lattice. These changes are manifested in the interannular C7─C8─C16─C17 torsion angles; and in the angles subtended at the nitrogen and carbon atoms of the isothiocyanate ligand. The parameters are given in Table 3.4 below for the crystal structures of **2**, **2·CH_3CN**, **2·CH_3OH** and **2·$(CH_3)_2CO$**.

Table 3.4 Selected intramolecular parameters for the cations in **2** and **2·solvent**

Parameter	2	2·CH_3CN	2·CH_3OH	2·$(CH_3)_2CO$
C7─C8─C16─C17 (°)	2.4	5.0	5.8	9.6
Pt─N─C (°)	173.1(1)	175.7(1)	175.3(1)	175.1(1)
N─C─S (°)	179.5(5)	179.2(5)	176.5(5)	179.0(5)

It is extremely difficult to quantify a link between a change in the overall packing and an intramolecular parameter of the kind listed in Table 3.4. This is especially true here since, as noted below, there are very small differences in the 3-dimensional arrangements of the cations and anions in **2** and **2·solvent**. Nevertheless, some observations seem pertinent. The first is that the interannular C7─C8─C16─C17 torsion angle increases when solvent molecules are included in the lattice; and that this torsion angle increases with increasing size of the solvent molecule; for example, it is largest for **2·$(CH_3)_2CO$**. Secondly, the isothiocyanate ligand exhibits some flexibility, in that the combination of Pt─N─C and N─C─S angles for **2** is different to that for the solvates. On the other hand, in **2·CH_3CN**

and **2·$(CH_3)_2CO$** the geometries of the isothiocyanate ligand are very similar, but very different to that determined for **2·CH_3OH**: see Table 3.4. We suggest that in the solvates, the isothiocyanate ligand adjusts its geometry so as to (i) accommodate the steric demands of the bulky S atom and (ii) in the case of the methanol solvate, to allow for O─H◦◦◦SCN hydrogen bonding. To illustrate the point we show in Figure 3.6 the positioning of the solvent molecule with respect to the cation (in particular with respect to the S atom) in **2·CH_3OH**, **2·CH_3CN** and **2·$(CH_3)_2CO$**. From the figure it is (just) evident that the S atom maintains a distance from the acetonitrile and acetone molecules, but moves towards the methanol hydrogen so as to facilitate hydrogen bonding. That there is a hydrogen bond between the S atom and the methanol O─H group follows from a S◦◦◦H distance of 2.38 Å and an O─H◦◦◦SCN angle of 156°. Both parameters fall well within the range expected for an O─H◦◦◦S hydrogen bond (by analogy with O─H◦◦◦O=C examples).[116,117] A closer look at the O─H◦◦◦S hydrogen bond is given in Figure 3.7. Interestingly, the presence of the hydrogen bond seems to have an important effect on the ease with which methanol can be extricated from the single crystals of **2·CH_3OH**: see the discussion in Section 4.3 below.

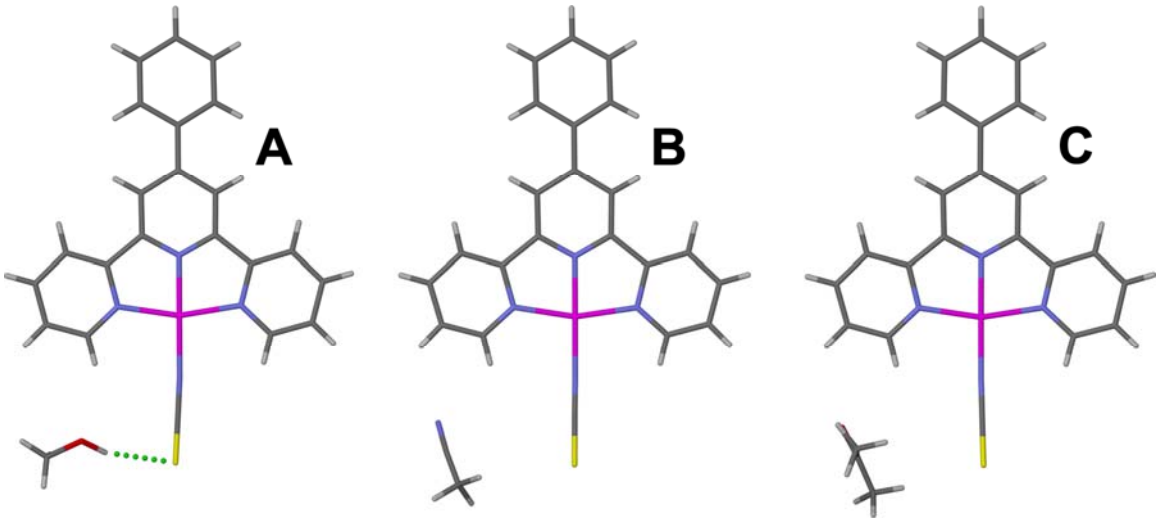

Figure 3.6 Diagrams that show the orientations and positions relative to the cation of the solvent molecules in (A) **2·CH_3OH** (B) **2·CH_3CN** and (C) **2·$(CH_3)_2CO$**; views have been taken perpendicular to the mean plane through platinum atoms and four coordinated nitrogens. Note the orientation of CH_3OH (A) differs from that of CH_3CN (B) and $(CH_3)_2CO$ (C).

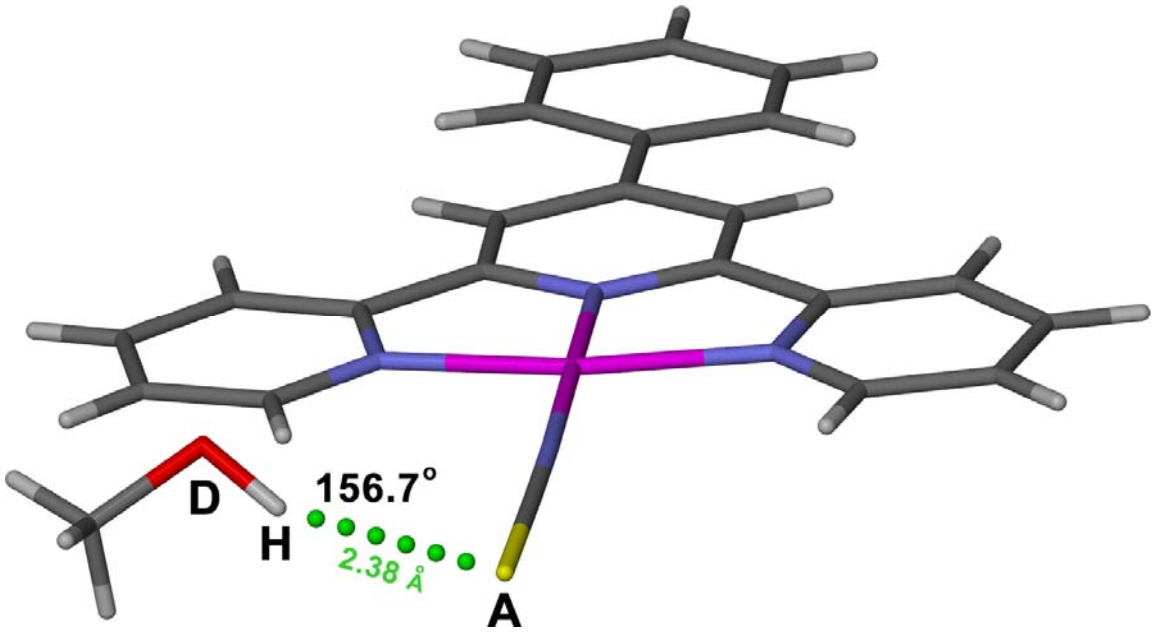

Figure 3.7 Diagram showing the hydrogen bond between the O─H group of a CH_3OH molecule and sulfur atom of a cation. The donor (D = oxygen), acceptor (A = sulfur) and hydrogen (H) atom are shown; along with the angle formed along the D─H◦◦◦A interaction, and the length of the H◦◦◦A interaction in green.

4.2.2 Crystal packing in 2·CH_3OH, 2·CH_3CN and 2·$(CH_3)_2CO$

In so far as the arrangement of the $[Pt\{4'\text{-}(Ph)trpy\}(NCS)]^+$ cations and SbF_6^- anions in crystals of **2**, **2·CH_3OH**, **2·CH_3CN** and **2·$(CH_3)_2CO$** is concerned, we first refer to Figure 3.2, where a view down the [c]-axis of the unit cell contents of **2** is given. The same plots for **2·CH_3OH**, **2·CH_3CN** and **2·$(CH_3)_2CO$** are given in Figures S5, S6 and S7 respectively, in the Supporting Information on the CD attached to the inside back cover of the thesis. The point we wish to make is that a visual comparison of the plot in Figure 3.2 with those in Figures S5, S6 and S7, shows no discernable changes in the positions of the cations and anions. Also true is that the brick-in-wall plot shown in Figure 3.3 for **2** is essentially repeated for **2·CH_3CN, 2·CH_3OH**, and **2·$(CH_3)_2CO$**, i.e. there are again no discernable differences in the porous cation/anion crystal structure packing arrangement, at least not differences that can be observed by inspection of a diagram with the naked eye. In fact, a careful comparison of the atom coordinates for the cations and anions in **2**, **2·CH_3OH**, **2·CH_3CN** and **2·$(CH_3)_2CO$** confirms that there are

only small changes when an acetonitrile, methanol or acetone molecule is added to a crystal of **2**. The small changes in the cation packing arrangement that do occur are reflected in changes in the three Pt∘∘∘Pt distances that define the three types of cation-cation overlap in **2**: see Figure 3.5. We give these Pt∘∘∘Pt distances in Table 3.5 below along with unit cell volumes – another measure of the degree to which the crystal structure packing arrangement of **2** changes on inclusion of solvent molecules.

Table 3.5 Unit cell volumes (Å^3) and Pt∘∘∘Pt distances (Å) for **2** and **2·solvent**[a]

	2	**2·CH_3OH**	**2·CH_3CN**	**2·$(CH_3)_2CO$**
Unit cell volume (Å^3) [a]	2523	2568	2610	2684
Pt∘∘∘Pt distance **A** (Å) [b]	3.553	3.395	3.519	3.443
Pt∘∘∘Pt distance **B** (Å) [b]	11.757	11.754	11.562	11.980
Pt∘∘∘Pt distance **C** (Å) [b]	9.616	9.724	9.930	9.786

[a] We recognise that the comparisons (of the unit cell volumes in particular) are not entirely valid since the structure determinations were not all done at 200 K; that for **2·CH_3OH** was done at 180 K. However, a difference of 20 K will not change the overall trends. [b] See Figure 3.5 for which Pt∘∘∘Pt distances the A, B and C labels apply to.

A clear trend in the above data is a small but systematic increase in the unit cell volume as the size of the solvent molecule increases; for **2·$(CH_3)_2CO$** the increase is the largest, but still by an amount of only ~ 6 %. The changes in the two longer Pt∘∘∘Pt distances brought about by inclusion of the solvent are small, and are unlikely to play any additional role in stabilising (or destabilising) the porous crystal structure packing arrangement, since they are way above the upper distance limit of 3.5 Å for finite d_{z^2}(Pt)-d_{z^2}(Pt) orbital interactions.[47] However, the shortest Pt∘∘∘Pt distance does drop below 3.5 Å for **2·CH_3OH** (3.395 Å) and **2·$(CH_3)_2CO$** (3.443 Å). The latter distance, being close to 3.5 Å, suggests that any contribution of d_{z^2}(Pt)-d_{z^2}(Pt) orbital interactions to stabilising the intermolecular interactions in **2·$(CH_3)_2CO$** is minimal. On the hand, the distance of 3.395 Å measured for the methanol solvate, is sufficiently short to suggest that d_{z^2}(Pt)-d_{z^2}(Pt) orbital interactions *do* play a role in stabilising single crystals of **2·CH_3OH**. Moreover, as already discussed, the presence of d_{z^2}(Pt)-d_{z^2}(Pt) orbital interactions can

have a dramatic effect on the solid state emission properties of the material. Also note that the crystal structure packing arrangement of **2·CH$_3$OH** has additional stability conferred upon it due to the presence of a hydrogen bond between a methanol molecule and S atom of the isothiocyanate ligand: see Figure 3.7.

We conclude: the porous crystal structure packing arrangement of a single crystal of **2** is essentially (but not wholly, there is some flexibility) retained when methanol, acetonitrile and acetone molecules are included in the lattice; but with methanol, the presence of O─H◦◦◦S hydrogen bonding and stabilising d_{z^2}(Pt)-d_{z^2}(Pt) orbital interactions could have implications with respect to (i) attempts to desolvate the material and (ii) whether the original crystal structure of **2** is obtained on desolvation. These implications are explored further in Section 4.3 below where we also describe the location of the solvent molecules in crystals of **2·CH$_3$CN**, **2·CH$_3$OH**, and **2·(CH$_3$)$_2$CO**; in particular in relation to the empty solvent channels in **2**.

4.3 Preliminary assessment of 2 as a porous metal-organic material

It is clear from the above discussion that compound **2** *viz*. [Pt{4'-(Ph)trpy}(NCS)]SbF$_6$ is crystalline, that it consists of a metal ion coordinated to a rigid organic molecule in a 3-dimensional structure and that it contains pores, or voids. Thus, it is correctly described as being a porous metal-organic material.[108,118] Of course, the real question is whether the pores are stable to the uptake and elimination of guest molecules, the most important of these being hydrogen as discussed in Section 1 of this chapter. We have yet to investigate the ability of compound **2** to sorb gases such as hydrogen and carbon dioxide, but we can report the results of our preliminary investigations into its ability to sorb molecules of solvent, in particular acetonitrile, methanol and acetone.

We start by simply describing the open solvent channels in **2** and how these are filled by molecules of solvent in the solvates. With regard to the solvent channels in **2**, the diagrams in Figure 3.8 refer. The channels are shown as green Conolly surfaces that are

plotted using a probe radius of 1.2 Å and the program X-SEED (v 2.0)[119] interfaced with MSROLL.[120] The empty space defined by the Conolly surface adopts a corkscrew motif, where the corkscrew comprises a series of bulges that are connected by narrower channels; the bulges protrude into regions between the layers of cations. The cross-section of a channel is estimated to be < 3.4 Å at the narrowest point (at 200 K, see Figure 3.9), a value too small to allow molecules as large as methanol, acetonitrile and acetone to squeeze through. However, it is important to note that the diagrams in Figure 3.8 represent the static crystal structure of **2** whereas, in reality, the atoms constantly vibrate about their mean positions. This vibrational motion will, in effect, widen the channels for a moment in time, thus allowing the solvent molecules to diffuse through the channels into the larger volume bulges. With regard to the location of the solvent molecules in the single crystals of their solvates the diagrams in Figure 3.9 refer. Note that the solvent molecules are drawn using the van der Waals radii of their constituent atoms and that they are placed inside a opaque green Conolly surface obtained originally from the crystal structure of the desolvated compound, **2**. From these diagrams it is clear that the solvent molecules are centred in the bulges but that their heteroatoms protrude out of the Conolly surface. This is most evident for the oxygen atoms of the methanol molecules in crystals of **2·CH$_3$OH**, an unsurprising result since, as illustrated in Figure 3.7, the methanol is hydrogen bonded to the S atom of an isothiocyanate ligand. Thus the empty channels in the crystal structure of **2** could be described as series of voids, occupied by solvent in the solvated forms, which are interconnected *via* narrow tunnels.

The next questions to address are: (i) the ease (or speed) with which the solvent molecules are included in (and lost from) crystals of **2** and (ii) how stable the porous packing arrangement of **2** is when subjected to an endless process of solvent molecule uptake and loss. We start with acetonitrile. Exposure of a single crystal of **2** to vapours of acetonitrile in a sealed container for 48 hours (see Section 6.1 of Chapter 4) affords a single crystal of **2·CH$_3$CN**. When a single crystal **2·CH$_3$CN** is exposed to air for ~ 6 days the acetonitrile molecules escape and the crystal structure of **2** is obtained; if a single crystal of **2·CH$_3$CN** is subjected to a vacuum at room temperature the removal of acetonitrile is speeded-up and occurs within 1 day.

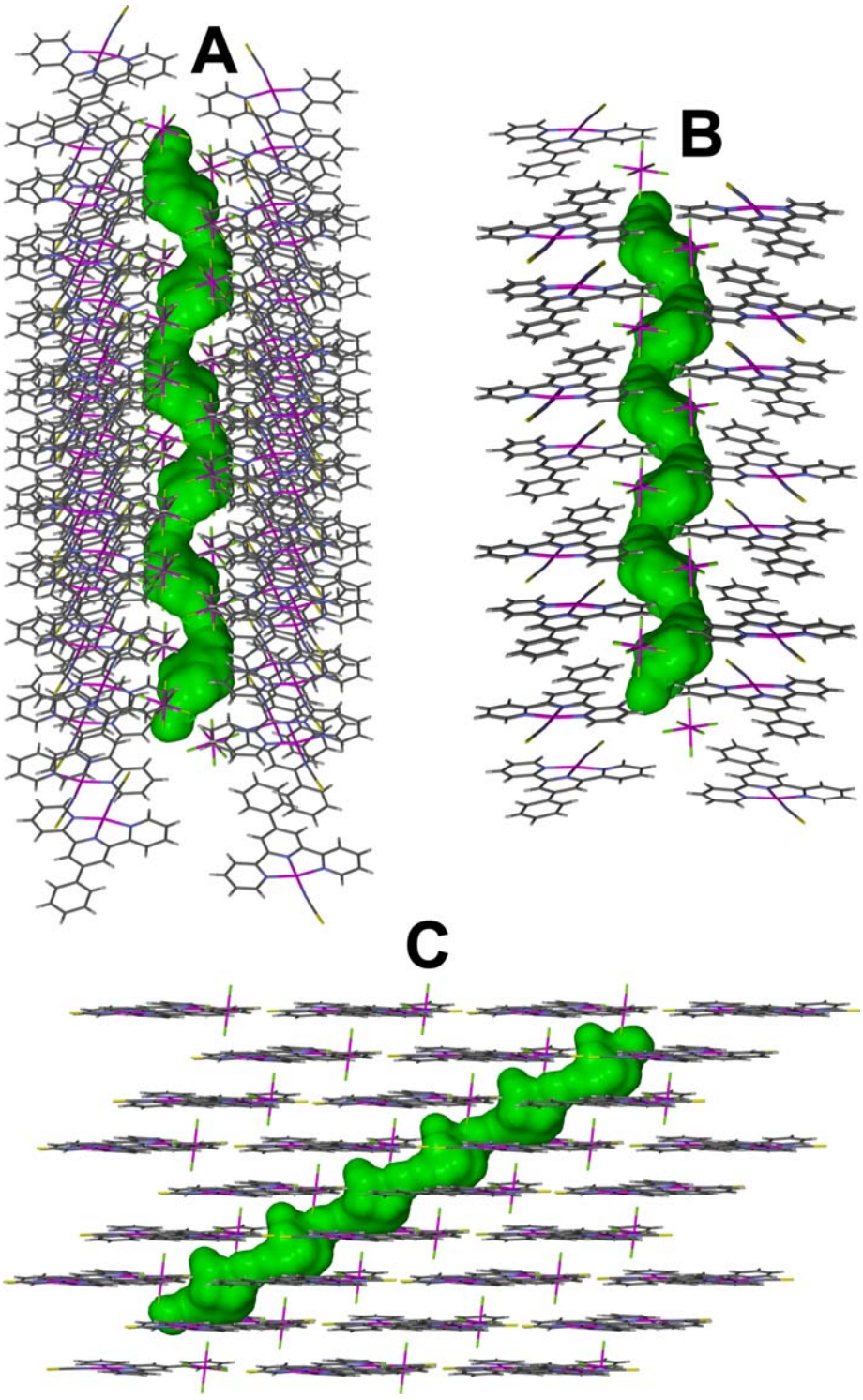

Figure 3.8 Three different views of the Conolly surfaces in a single crystal of **2**. The Conolly surfaces are shown in green and drawn with a probe radius of 1.2 Å. Views (A) and (B) depict the "corkscrew" shape of the channel; (B) and (C) show the narrower channels that join larger bulges. The bulges are filled by solvent molecules in the solvated salts: see Figure 3.9 below.

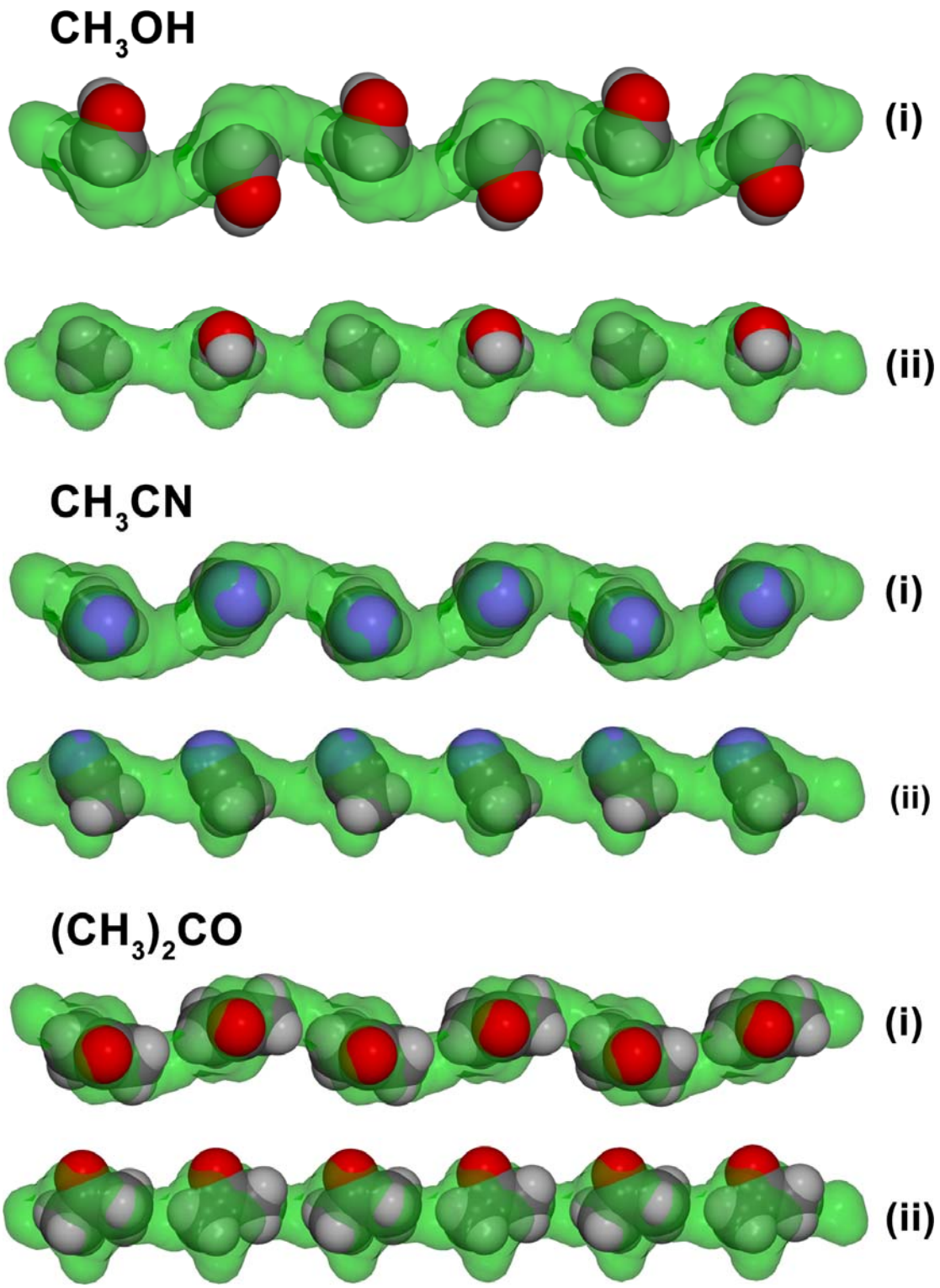

Figure 3.9 Plots showing two different views of the location of the solvent molecules in the crystals of **2·CH$_3$OH**, **2·CH$_3$CN** and **2·(CH$_3$)$_2$CO** in relation to the Conolly surface (shown in green) obtained from the crystal structure of **2**.

We have performed reliable single crystal structure determinations of each of the compounds in the following sequence, all using the *same single crystal*: **2·CH_3CN** (see **2MeCN_1st.cif**); **2** (see **2_1st.cif**); **2·CH_3CN** (see **2MeCN_2nd.cif**); and **2** (see **2_2nd.cif**). (The CIF files are in the Supporting Information on the CD attached to the inside back cover of the thesis.) We conclude that **2** sorbs and desorbs acetonitrile molecules relatively easily and with retention of its porous metal-organic structure; thus **2** performs well as a MOF material with respect to acetonitrile. This is not surprising since single crystals of **2** were obtained by desolvation of single crystals of **2·CH_3CN** in the first place.

Next is methanol. Exposure of a single crystal of **2** to vapours of methanol in a sealed container for 48 hours (see Section 6.1 of Chapter 4) affords a single crystal of **2·CH_3OH**. However, preliminary investigations show that the removal of methanol molecules from a single crystal of **2·CH_3OH** is not as facile as that for the removal of acetonitrile molecules from **2·CH_3CN**; given the hydrogen bonding of the methanol to the S atom of the isothiocyanate ligand this is expected. Moreover, we are still not certain as to whether if methanol is removed (for example by applying a vacuum) a single crystal with the original crystal structure of **2** is regained. In fact, there is circumstantial evidence that the original crystal structure of **2** is *not* obtained: see the discussion of the solid state emission properties of **2** and the various solvates in Section 5.2 of this chapter. It would seem that compound **2** has limitations as a porous metal-organic material with respect to methanol but clearly, more work is required with respect to methanol uptake and loss by single crystals of **2**; this is planned.

Next is acetone. Exposure of a single crystal of **2** to vapours of acetone in a sealed container for 48 hours (see Section 6.1 of Chapter 4) affords a crystal of **2·$(CH_3)_2CO$** that only allows for an unreliable structure solution, i.e. there is some loss of single crystallinity. We have included the relevant CIF file in the Supporting Information on the CD attached to the inside back cover of the thesis: see **2acet_exp.cif**, where "exp" denotes **exp**osed to vapours of acetonitrile. Note that the unit cell parameters and atom positions essentially match those obtained with the "good quality" crystal: see

2acet_dir.cif where "dir" denotes crystals grown **dir**ectly from acetone. In so far as the loss of acetone from a single crystal of **2·$(CH_3)_2CO$** is concerned, this occurs relatively slowly under ambient conditions (~ 2 weeks); but there is no loss of single crystallinity, as confirmed by a single crystal structure determination: see **2desacet.cif** in the Supporting Information. The first conclusion we draw is that the acetone molecule is the largest that could possibly fit into the voids in **2** without disruption of the long range order in the crystal. This sets a limit on the use of **2** as a porous metal-organic material for the sorption of larger molecules. Also, note the longer time it takes for acetone molecules to escape from a crystal of **2·$(CH_3)_2CO$** than for acetonitrile molecules to escape from single crystals of **2·CH_3CN**. This result is counter intuitive, since acetone has a higher vapour pressure than acetonitrile. We believe that it has to do with the larger size of the acetone molecule and that, because it is larger, it becomes more difficult for the acetone molecules to escape through the narrow channels that link the larger bulges: see Figure 3.9. Thus, compound **2** also has limitations with respect to the speed of solvent molecule loss when the molecule is relatively large in size.

If this thesis were to have sub-title it could be: "**Planar platinum complexes that can move; but sometimes don't**". When solvent is allowed to escape from single crystals of **1·CH_3CN—Y** the planar $[Pt(trpy)(NCS)]^+$ cations move (actually slide) into new positions, a powder is formed and the colour changes to maroon. Even after desolvation is complete, the cations of **1—M** are still able to slide over each other in response to change in temperature. When solvent is allowed to escape from single crystals of **2·CH_3CN,** the planar $[Pt\{4'\text{-}(Ph)trpy\}(NCS)]^+$ cations essentially retain their original positions, another single crystal forms and the colour remains yellow. Of course, the reason why the $[Pt\{4'\text{-}(Ph)trpy\}(NCS)]^+$ cations do not move is that they are locked into the "brick-in-wall" structure illustrated in Figure 3.3: as discussed this "brick-in-wall" arrangement is stabilised by an endless sequence of stabilising π(trpy)-π(trpy) interactions. To the best of our knowledge, there have been no previous reports of a ***porous*** metal-organic structure of this kind. This is not surprising as the idea that a resilient packing arrangement can be formed from planar cations that are arranged coplanar and parallel to one another, goes against observations reported by workers in the

field. The fact is that a MOF framework is usually retained on solvent loss only for crystals with strongly bonded networks, such as zeolites, some hydrogen bonded networks and materials consisting of robust building blocks with rigid molecular rings.[105,106] In fact, even the porous metal-organic material described by Barbour and co-workers makes use of two doubly bridged silver atoms within a relatively large rectangular shaped complex, to ensure that the solvent templated channels are formed in the first instance and then retained after solvent extrication.[108] So, we have a nice result, but it is not one that was predictable – we have to acknowledge that the crystal structure of [Pt{4'-(Ph)trpy}(NCS)]SbF_6 (**2**) was not deliberately engineered in any way. However, it is clear that the N-bound isothiocyanate ligand (in particular the large S atom) plays a crucial role in determining the crystal structure of **2**; we say this because other ionic platinum terpyridines that contain the 4'-(Ph)trpy ligand, but with a different co-ligand, have very different crystal structures to that of **2**.[10,16,24,33]

5 Luminescent properties of [Pt{4'-(Ph)trpy}(NCS)]SbF_6 (2) in the solid state

5.1 General

Initial efforts in terms of luminescence measurements focused on obtaining emission spectra from a sample consisting of single crystals of **2** and **2·solvent**. However the nature of the sample made it very difficult to obtain consistent spectra. For example; rotating the sample holder or changing the sample packing would produce differences in the emission spectrum. In addition to this, the slow rates of solvation and desolvation made it difficult to obtain reliable emission spectra for **2** and **2·solvent**. In Section 5.2 of Chapter 2 we described the use of a 1:5 KBr matrix of a powdered sample of **1—M** to facilitate more rapid solvation and desolvation of the VOCs – the same approach used by other workers for measurements of the same kind.[9] Thus all luminescence measurements have been recorded using a 1:5 KBr matrix of compound **2**, in which the original single crystals of **2** had been ground into a powder. Unlike for the vapochromic studies of

compound **1**, we have only measured the emission spectra of three solvates *viz*. **2·CH_3CN**, **2·CH_3OH** and **2·$(CH_3)_2CO$**. This is because there is no visible colour change (from yellow) when solvent vapours are included into the crystal lattice of **2** – an unsurprising result since, as discussed in Section 4.2, the crystal structure packing arrangement hardly changes on incorporation of solvent molecules of acetonitrile, methanol and acetone. Nevertheless, as we show below, there *is* a change in the *emission* spectrum and we wished to link this change to the single crystal structure determinations of **2**, **2·CH_3OH**, **2·CH_3CN** and **2·$(CH_3)_2CO$**. In order to make sure that the powder sample of **2** used for the emission measurements retained the crystal structure of a single crystal of **2**, we have recorded the powder XRD spectrum at room temperature. This powder spectrum is compared with that calculated from a single crystal structure determination of **2**, also performed at room temperature (295 K): see Figure S8 in the Supporting Information on the CD attached to the inside back cover of the thesis. There is a very close match, confirming that it is safe to assume that no phase change occurs on crushing a single crystal sample of **2**.

5.2 Luminescent properties of 2 and 2·solvent

All luminescence measurements of **2**, **2·CH_3OH**, **2·CH_3CN** and 2·**$(CH_3)_2CO$** have been recorded on 1:5 solutions of the powdered salts in a KBr matrix. Although the solvated powders are labelled as containing one solvent molecule per cation (**2·solvent**) the exact ratio of the solvent molecules to cations is strictly speaking, not certain; we assume that it is the same as determined for the single crystals. (In this respect, note that the method used to prepare the powdered sample for an emission measurement ensures that it is "dry", i.e. free of excess solvent: see Section 5.2 of Chapter 4.) Of course, a sensible experiment would be to measure the powder XRD spectra of the solvates and compare these with those calculated from the single crystal structure determinations; but this was very difficult to do for two reasons. First, the powder samples lose solvent relatively quickly and second, the powder XRD spectra should be measured at ~ 77 K for a comparison with the emission measurement done at 77 K. This was not possible with the powder X-ray diffractometer at our disposal: see Section 8.1 of Chapter 4.

In terms of the organisation of the next sections the single crystal structure determinations of **2·CH_3CN**, **2·CH_3OH** and **2·$(CH_3)_2CO$** described in Section 4.2 refer. With **2·CH_3CN** and **2·$(CH_3)_2CO$**, there is essentially no additional intramolecular interaction (that could influence the emission) as compared to those in crystals of **2**. In contrast there is an additional d_{z^2}(Pt)-d_{z^2}(Pt) orbital interaction in crystals of the methanol solvate. For these reasons the luminescent properties of **2**, **2·CH_3CN** and **2·$(CH_3)_2CO$** are discussed together first, while that of **2·CH_3OH** is discussed in the subsequent section.

5.2.1 Luminescent properties of 2, 2·CH_3CN and 2·$(CH_3)_2CO$

The emission spectra of **2**, recorded at 77 and 298 K, are shown in Figure 3.10; clearly the latter is so weak as to be virtually undetectable. The 77 K spectrum consists of a broad (fwhm = 3080 cm^{-1}) band centered at 650 nm, with shoulders at ~ 550 and ~ 590 nm which give the band a domed shape. We have inserted on the figure the lifetimes associated with each peak.

Note that analysis of the decay of the emission intensities at ~ 550 and ~ 590 nm shows that they are biphasic, i.e. two separate lifetimes are needed to fit the decay curve. This implies that the emission spectrum shown in Figure 3.10 derives from two different excited states, i.e. multiple emission is observed in the solid state. When we examine (below) the emission by the solvates **2·CH_3CN** and **2·$(CH_3)_2CO$** it will become clear that one of the emitting states is ^{3}MLCT in origin; as it turns-out the other is excimeric in origin: the discussion in Sections 1.3.2 and 1.3.3 of Chapter 1 now refers.

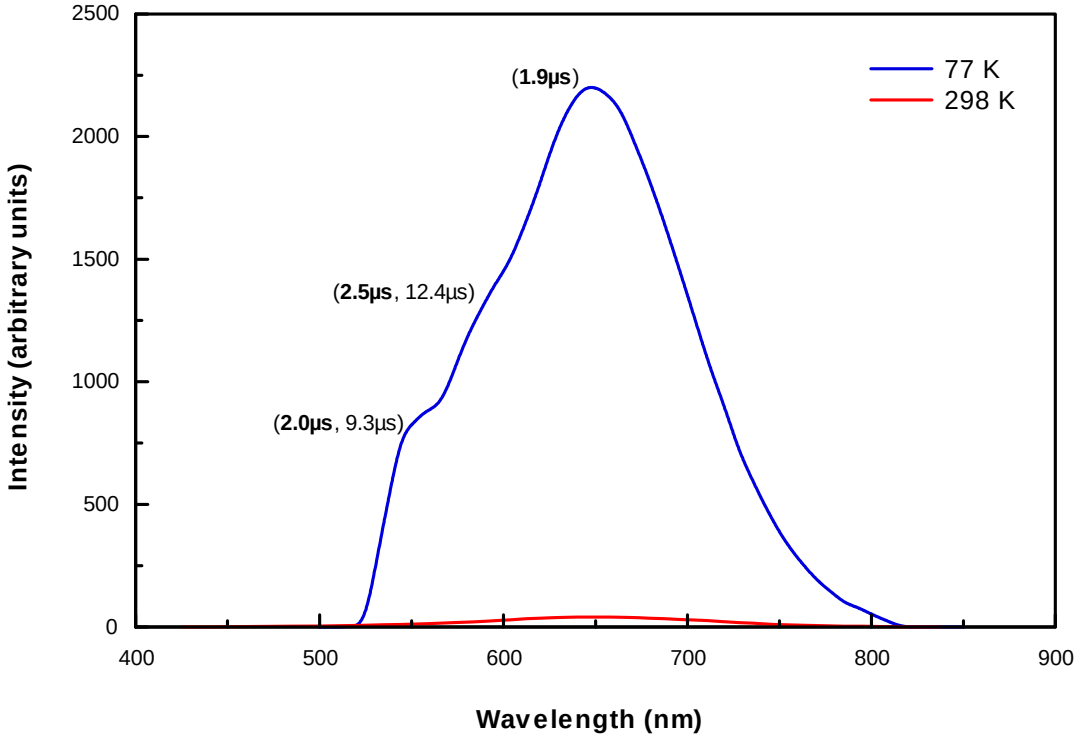

Figure 3.10 Solid state emission spectra of compound **2** at 77 (blue) and 298 K (red). The values in brackets indicate the excited state lifetime/s (τ) recorded for the different peaks. Note that two lifetimes indicates that the emission intensity decay curve is biphasic.

Turning our attention to the luminescence properties of **2·CH_3CN** we find considerable differences to those of **2**: the emission spectrum of **2·CH_3CN** recorded at 77 K is shown in Figure 3.11, along with that of **2·$(CH_3)_2CO$**, shown on the same scale. First note that emission by **2·CH_3CN** is ~ 12 times more intense than that of the desolvated compound. Secondly, the band profile is entirely different: three bands are also observed at 550, 587 and 632 nm but their intensity decreases monotonically with an increase in wavelength.

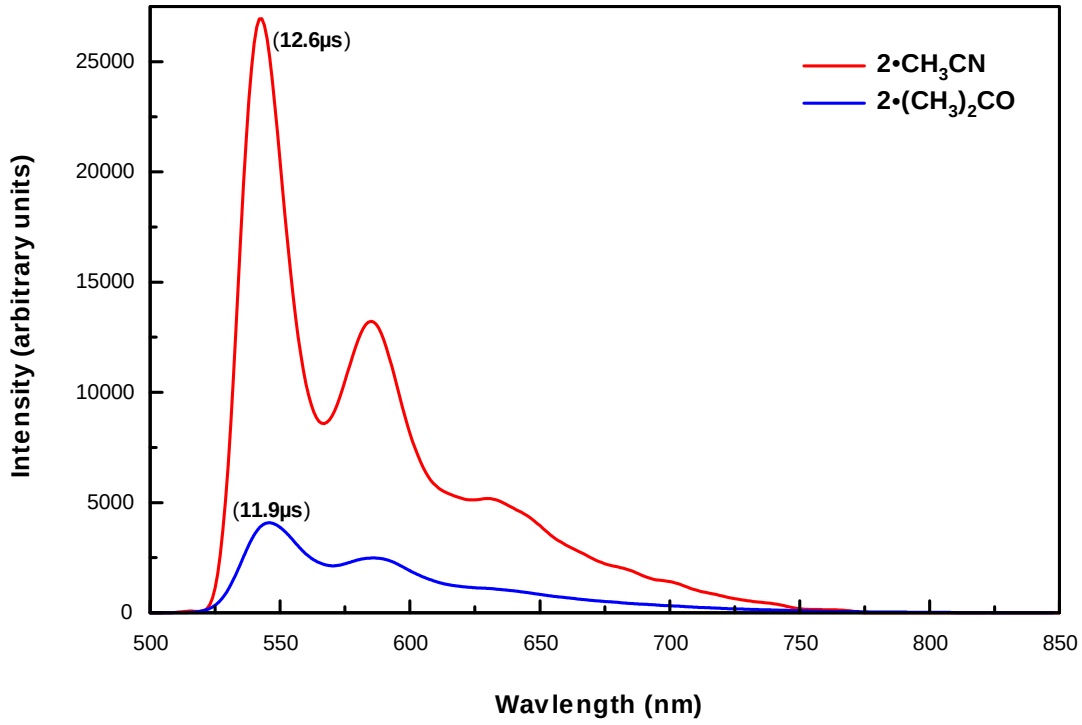

Figure 3.11 Solid state emission spectra of **2·CH_3CN** [red] and **2·$(CH_3)_2CO$** [blue] recorded at 77 K. The values in brackets indicate the excited state lifetimes (τ) recorded for the different peaks. Not that the intensity scale continues from that used in Figure 3.10, and illustrates the relative intensity of emissions from **2·CH_3CN** (77 K) and **2·$(CH_3)_2CO$** (77 K).

This envelope of vibronic structure is diagnostic for monomeric ^{3}MLCT emission.[13,23] Confirmation of the ^{3}MLCT assignment comes from a Huang-Rhys ratio ($I_{0\text{-}1}/I_{0\text{-}0}$) of 0.5, and an energy separation between the vibronic components of ~ 1300 cm^{-1}. This value is typical of the C─C and C─N stretching motions of the terpyridine framework.[44-46,121] The spectrum of the acetone solvate, although weaker, also shows the features typical of ^{3}MLCT emission, with vibrational components essentially matching those observed for **2·CH_3CN** both in terms of position and relative intensity. It should also be noted that the lifetimes of the most intense peak (0-0 transition at 550 nm) is monophasic for both **2·CH_3CN** and **2·$(CH_3)_2CO$**. In Section 4 of this chapter single crystal X-ray determinations showed that there are no significant differences between the packing arrangements of the cations and anions of **2** on one hand, and **2·CH_3CN** and

2·$(CH_3)_2CO$ on the other. Thus it is not unreasonable to expect the same emission spectrum from **2**, **2·CH_3CN** and **2·$(CH_3)_2CO$**. In fact, bands in the same positions are observed for **2**, **2·CH_3CN** and **2·$(CH_3)_2CO$**; it is simply that the relative intensities of the bands for the solvates are very different to those recorded for **2**. It is clear from the above discussion and the spectra in Figure 3.11 that both **2·CH_3CN** and **2·$(CH_3)_2CO$** display monomeric ^{3}MLCT emission ***only***. Thus, for some reason, there is a predisposition towards emission from a ^{3}MLCT excited state when solvent molecules are included in the lattice. Before attempting to explain why this is the case, we report a further experiment that highlights how the ^{3}MLCT component of the emission becomes less important as solvent is lost to form the desolvated compound, **2**.

We have monitored by recording emission spectra at varying degrees of solvation, the desolvation of **2·CH_3CN** to give **2**. This was done by exposing the solvated sample to ambient conditions for short periods, to allow desolvation to occur; and then the sample was rapidly cooled to 77 K. By freezing the sample to liquid nitrogen temperatures solvent loss is prevented while the spectra are recorded; thus each spectrum is a "freeze-frame" in time during the desolvation process. The results are shown in Figure 3.12. (Very similar changes in the emission spectra are observed when the acetone solvate, **2·$(CH_3)_2CO$**, is slowly desolvated and thus the following arguments also apply to that system.)

Initially, solvent loss causes the ^{3}MLCT emission to gradually and systematically drop in intensity, i.e. the relative intensities of the vibrational components stay the same but the overall (integrated) intensity of the emission drops. However, when the desolvation process is well advanced (see the insert graph) it becomes apparent that while the vibrational components at 550 and 587 nm continue to drop in intensity, that at ~ 650 nm stays much the same in intensity. Eventually, the spectrum characteristic of **2** is obtained. As already noted this spectrum is very weak and characterised by a broad peak that maximises at 650 nm with higher energy shoulders at ~ 550 and ~ 590 nm.

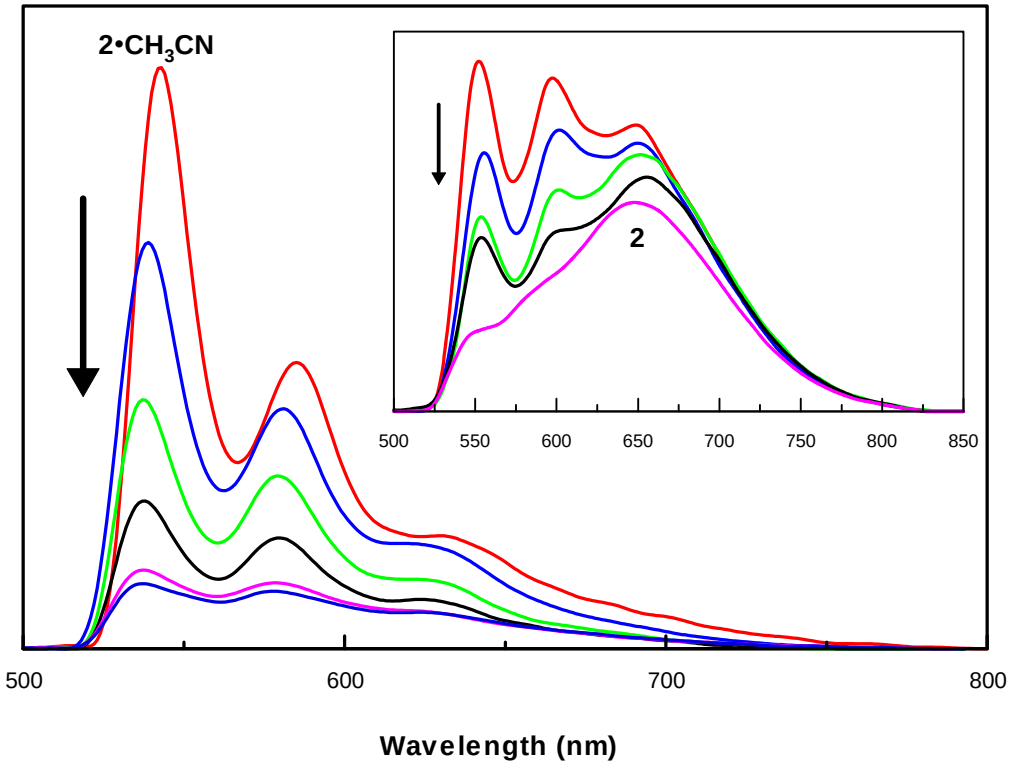

Figure 3.12 Solid state spectra of various levels of solvation of **2** by CH_3CN, starting with **2·CH₃CN** (red line on the main graph) and ending at **2** (purple line in the insert): the vertical axis in each plot reflects the relative intensity of the emission. Each spectrum was recorded at 77 K at a particular stage during the desolvation of **2·CH₃CN**. The desolvation process, followed using luminescence, is split into two graphs due to the large changes in emission intensity. The intensities of the spectra are such that the least intense spectrum on the main graph is slightly more intense than the most intense spectrum on the insert graph.

We now return to the assignment of the emission exhibited by the desolvated compound, **2**, in the solid state: see Figure 3.10. We suspect, based on the measured lifetimes and the desolvation experiment, that the peaks at ~ 550 and ~ 590 nm originate from the ^{3}MLCT excited state which is characteristic of the emission spectra of **2·CH₃CN** and **2·(CH₃)₂CO**. The remaining band at ~ 650 nm is asymmetric broad and devoid of any vibrational structure of its own. These features (see Figure 1.9) as well as the colour of **2** (yellow) are consistent with the assignment of the emission to an excimeric $^3(\pi\text{-}\pi^*)$ excited state.[12,15,16,18,23,24,34,52-57] Furthermore the excimeric emission occurs at a slightly

lower energy than that of the ^{3}MLCT emission – as would be expected: refer to Section 1.3.2 of Chapter 1. Thus it is evident that the excited state manifold of **2** consists of vibronically coupled ^{3}MLCT and excimeric excited states. The interconversion of excited state energy between the two states is thermally-mediated with the lower energy excimeric excited state being the thermodynamically favoured emitting state. However, at 77 K, the temperature used for the emission measurements, the rate of the transfer of energy from the ^{3}MLCT to the excimeric excited state, is slowed down: thus ^{3}MLCT emission is observed, along with the excimeric emission. Similar emission band profiles have been observed before and assigned to the same type of excited states: for example for the yellow polymorph of [Pt{4'-(Ph)trpy}(CN)]BF_4.[24]

In Section 4 of this Chapter we showed that there are no significant changes in the relative positions of the anions and cations between **2**, **2·CH_3CN** and **2·$(CH_3)_2CO$**. On this basis it seems reasonable to expect that **2**, **2·CH_3CN** and **2·$(CH_3)_2CO$** should exhibit the same emission in the solid state, especially since the cation is the chromophore; however this is clearly not the case given the absence of evidence for excimeric emission in the spectra recorded for **2·CH_3CN** and **2·$(CH_3)_2CO$**. A clue to why comes from the discussion of the mechanistic details of excimeric emission in Section 1.3.2 in Chapter 1. In order for an excimeric excited state to be attained, a monomer (in this case a cation) in its excited state must associate with a ground state monomer. This pathway contains a potential energy barrier which has to be surmounted before an excimer can form. We propose that the inclusion of solvent molecules in the crystal lattice (or absence of free space) interferes in some way with the formation of the excited state dimer by increasing the potential energy barrier to excimer formation. As a result excimeric emission does not occur, and for this reason is not observed for **2·CH_3CN** and **2·$(CH_3)_2CO$**. In terms of the mechanism proposed, the comparatively tightly packed ("overcrowded") crystal lattice of these solvated forms hinders the reorientation and/or association/interaction of the cations (monomers) necessary for the formation of excimers. Conversely, when there is no solvent present the crystal lattice is more loosely packed, due to empty solvent channels between "cation walls", which lowers the potential energy barrier to excimer formation. As a result the excimers can form, and excimeric emission is observed for **2**.

We finally comment on the fact that ^{3}MLCT emission exhibited by the solvate **2·CH_3CN** [and to a lesser extent **2·$(CH_3)_2CO$**] is more intense than the dual emission exhibited by the desolvated compound, **2**. The most common mechanism for the non-radiative decay of an excited state of a solid is *via* the thermal vibrations of the atoms comprising the solid. On average, the atom vibrations in the more tightly packed solvates will be less than in the desolvated compound, **2**; after all the latter contains empty solvent channels. Thus, more intense emission is to be expected for the solvates. That it is more intense for **2·CH_3CN** than **2·$(CH_3)_2CO$** is probably due to the fact that the acetone molecule has a larger number of vibrational modes (19) than the smaller acetonitrile molecule (12); the excited state energy in the acetone solvate [**2·$(CH_3)_2CO$**] is more easily dissipated *via* thermal vibrations.

5.2.2 Luminescent properties of 2·CH_3OH

Emission from **2·CH_3OH** is very weak at room temperature, and thus the spectrum has been recorded at 77 K: see Figure 3.13. The spectrum is characterised by two distinct peaks, one at 550 nm and a somewhat more intense and rather broad peak at 607 nm. Clearly, the spectrum is very different in terms of the profile from those recorded for the other two solvates, **2·CH_3CN** and **2·$(CH_3)_2CO$**: see Figure 3.11. Also different is that the peak separation is ~ 1800 cm^{-1}, a value which falls outside the normal range of 1200-1400 cm^{-1} for the relevant stretching vibrations of the terpyridyl ligand.[44-46,121]

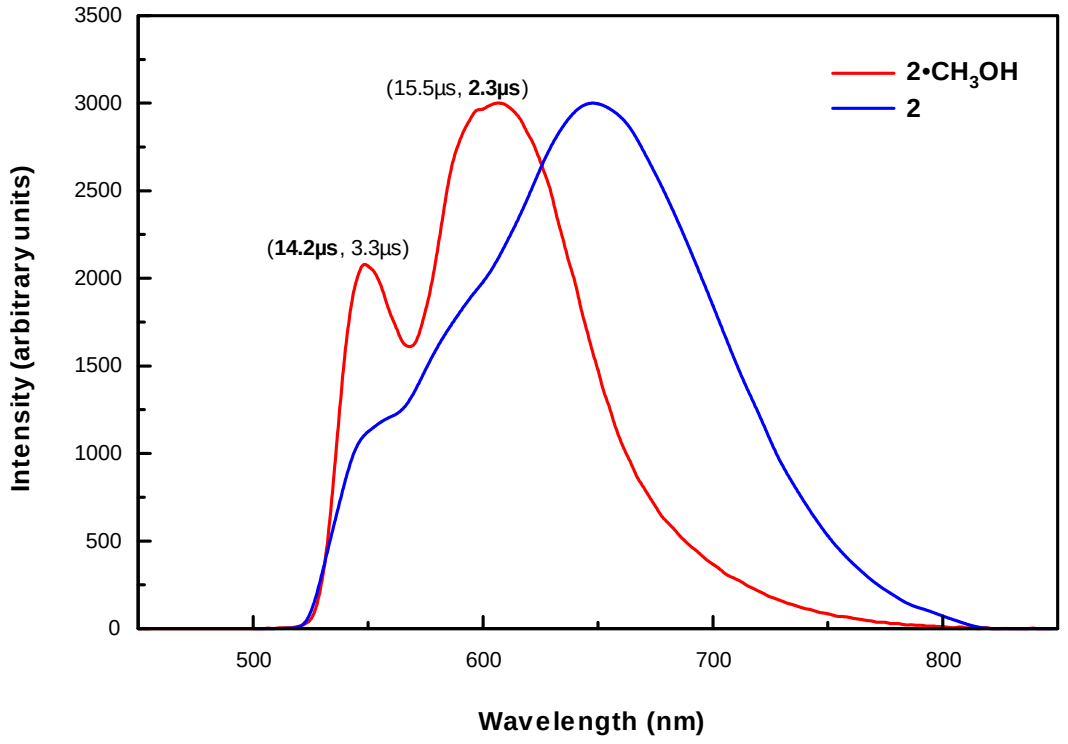

Figure 3.13 Solid state emission spectra of **2·CH_3OH** (red line) and **2** (blue line) recorded at 77 K. The relative intensities of the two spectra are arbitrary. The values in brackets indicate the lifetime/s (τ) recorded for the different peaks. Note that two lifetimes indicate that the emission intensity decay curve is biphasic.

These observations lead to the inevitable conclusion that the methanol solvate, unlike the other two solvates, does not exhibit vibronically structured monomeric ^{3}MLCT emission in the solid state – at least not *solely* ^{3}MLCT emission. Yet the peak at 550 nm does coincide with the 550 nm band assigned to the 0-0 component of the ^{3}MLCT emission by **2·CH_3CN** and **2·$(CH_3)_2CO$**: see Figure 3.11. Indeed the magnitude of the lifetime of the peak (14.2 µs) is consistent with this assignment, following the lifetimes determined for the ^{3}MLCT emission of **2·CH_3CN** and **2·$(CH_3)_2CO$**. Furthermore, it should be noted that the peak at 607 nm is significantly blue-shifted and narrower than the excimeric emission peak observed for the desolvated form, **2**: see Figure 3.13. Therefore it is highly unlikely that excimeric emission is solely responsible for the peak at 607 nm. Thus the strong peak at 607 nm is new and, being new, leads one to conclude that the peaks at 550 and 607 nm

have different origins, i.e. **2·CH_3OH** exhibits simultaneous emission from (*at least*) two separate excited states in the solid state.

We now address the question of the origin of the multiple emission by **2·CH_3OH**. The crystal structure determination of **2·CH_3OH** at 180 K is helpful in this regard: see Section 4.2 earlier in this chapter. This structure determination shows that there is a short Pt∘∘∘Pt distance of 3.395 Å linking the two platinum atoms of the pair labelled "A" in Figure 3.5; a distance well within the limit of ~ 3.5 Å for a finite d_{z^2}(Pt)-d_{z^2}(Pt) orbital interaction.[47] On this basis we would anticipate that a ^{3}MMLCT excited state would form part of the emission manifold for **2·CH_3OH**; and that, therefore, the "new" peak at 607 nm in Figure 3.13 has its origins in ^{3}MMLCT emission. As already implied, the peak at 550 nm is associated with the monomeric ^{3}MLCT emission that typifies emission by **2·CH_3CN** and **2·$(CH_3)_2CO$**. To test this assumption we have deconvoluted the spectrum in Figure 3.13 into constituent Gaussian bands using standard non-linear regression methods; the results are shown in Figure 3.14.

As shown in Figure 3.14, a total of five bands are mandatory in order to provide a suitable fit of the experimental emission spectrum of the sample. The Gaussian bands coloured blue, light blue and pink are centred at 550, 585 and 631 nm and, moreover, decrease monotonically in intensity as the wavelength increases. This profile, as well as the band energies, match that of the ^{3}MLCT emission exhibited by **2·CH_3CN** and **2·$(CH_3)_2CO$**: see Figure 3.11. The fourth band of interest, coloured green, is centred at 609 nm with a fwhm value of 1 590 cm^{-1}, i.e. it is relatively narrow. This band is, both in terms of energy and profile, typical of the kind of solid emission observed by planar complexes of platinum(II) that have crystal structures containing Pt_2 dimers: see for example [Pt(trpy)Cl]CF_3SO_3 (λ_{em}^{max} = 625 nm at 77 K),[23] [(2,6-di-(2'-naphthyl)-4-pyridine)Pt_2{μ-bis(diphenylphosphino)methane}] (λ_{em}^{max} = 602 nm) and its solvates.[89] We therefore assign it as ^{3}MMLCT in origin.

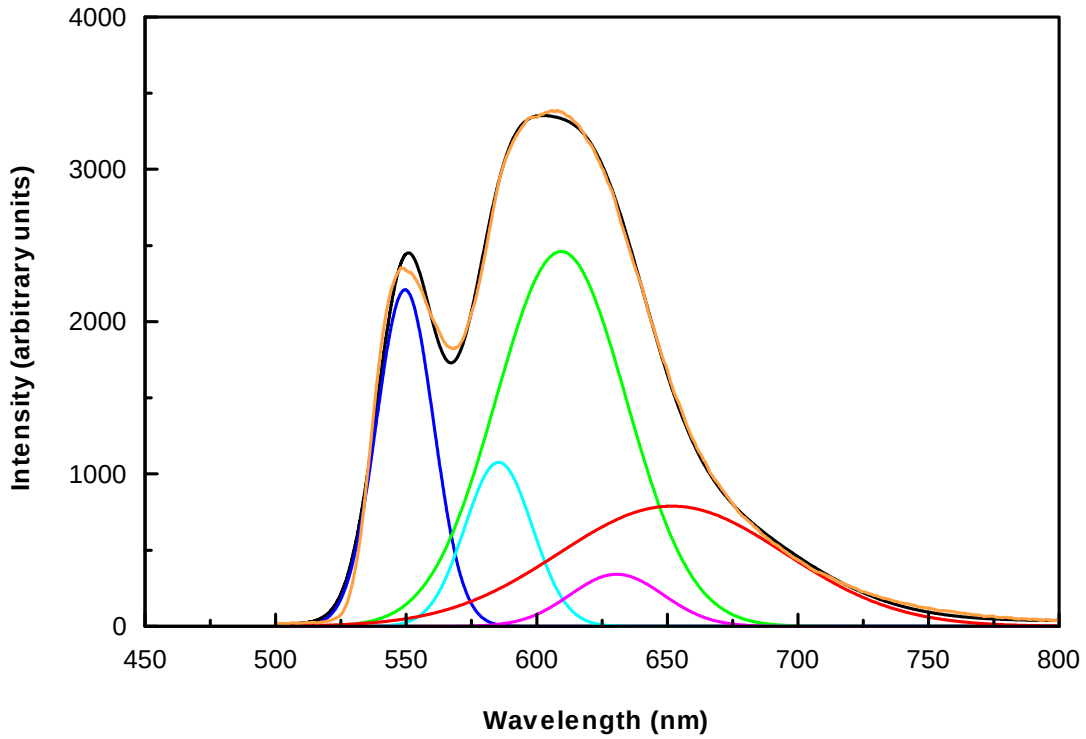

Figure 3.14 Solid state emission spectrum recorded at 77 K of **2·CH_3OH,** deconvoluted into five constituent Gaussian bands (r^2 = 0.9990; fit std error = 35.29). Different colours are used for the different components of the emission: see text. The observed intensity is shown by the orange line and the calculated intensity by the black line.

Finally, the fifth band, coloured red, is very broad and centered at 652 nm. Of course such a band is reminiscent of the 650 nm band observed in the emission spectrum of the desolvated compound, **2**: see Figure 3.10. We assume, therefore, that it originates from an excimeric excited state. The presence of an excimeric component in the emission by methanol solvate is not expected if the above argument explaining its absence in the emission spectra of acetonitrile and acetone solvates is extrapolated to the methanol system. However, as the crystal structure determination of **2·CH_3OH** shows, the methanol molecule is more tightly bound (*via* hydrogen-bonding) and differently orientated with respect to the cation than in **2·CH_3CN** and **2·$(CH_3)_2CO$**: see discussion in Section 4.2 of this chapter. Also, being a smaller molecule it occupies less space, i.e. there is more "empty" space between the cations in **2·CH_3OH** than in **2·CH_3CN** and

2·$(CH_3)_2CO$. We cannot be exact, but the point is that the crystal structure of the methanol solvate is different, not least because the presence of metallophilic Pt◦◦◦Pt interactions that "pull" the cations closer together; and these differences could account for the fact that the excited state dimers can and do form on irradiation of the solid.

We conclude that the emission spectrum of **2·CH_3OH**, though complicated, is understandable in terms of the simultaneous emission from ^{3}MLCT, ^{3}MMLCT and excimeric excited states. To the best of our knowledge such solid state emission has not been reported previously. We speculate that this may, in part, be a result of the unique packing arrangement of the cations (described in Section 4 of this chapter) and the presence of finite d_z^2(Pt)-d_z^2(Pt) stabilising orbital interactions in the solid state.

In Section 4.3 of this chapter we noted that the methanol molecule is more difficult to remove from a single crystal of **2·CH_3OH**, than are the acetonitrile and acetone molecules from single crystals of **2·CH_3CN** and **2·$(CH_3)_2CO$** respectively; easily understood because the methanol is hydrogen bonded to the sulfur atom in crystals of **2·CH_3OH**. We have experienced the same problem with the powder sample of **2·CH_3OH** in a KBr matrix used for the emission studies. In fact, we had to resort to gently heating the sample under vacuum to remove the methanol completely. Interestingly, the emission spectrum recorded on the product so obtained (labelled **2·CH_3OH_DS**) is not the same as that originally recorded for **2**: the spectra recorded at 77 K of **2**, **2·CH_3OH** and **2·CH_3OH_DS** are compared in Figure 3.15.

The principal feature of the **2·CH_3OH_DS** emission spectrum is a strong, relatively narrow (fwhm = 2 100 cm^{-1}) band centred at 627 nm. We associate this band with the ^{3}MMLCT component of the emission by **2·CH_3OH**, for the same reasons as given above. If this assignment is valid, then an inevitable conclusion must be that the slightly modified porous metal-organic structure of the methanol solvate, specifically with the short Pt◦◦◦Pt distance, is retained after the methanol is removed. Clearly, this conclusion is best tested by attempting to desolvate a *single* crystal of **2·CH_3OH**, without disruption of its single crystallinity, and then to carry-out a single crystal structure determination.

This will be tried as part of ongoing future work of this project. At this juncture, it should be noted that the emission spectrum of **2·CH$_3$OH_DS** exhibits, in addition to the 627 nm peak, a smaller peak at 550 nm: see Figure 3.15. As discussed above, such a peak indicates the occurrence of monomeric ^{3}MLCT emission in the solid state; as does the magnitude of the lifetime recorded (12.9 μs) being similar to that recorded for **2·CH$_3$CN** and **2·(CH$_3$)$_2$CO**. The presence of ^{3}MLCT emission would be expected if the crystal packing arrangement of **2·CH$_3$OH** is essentially retained after removal of the solvent molecules.

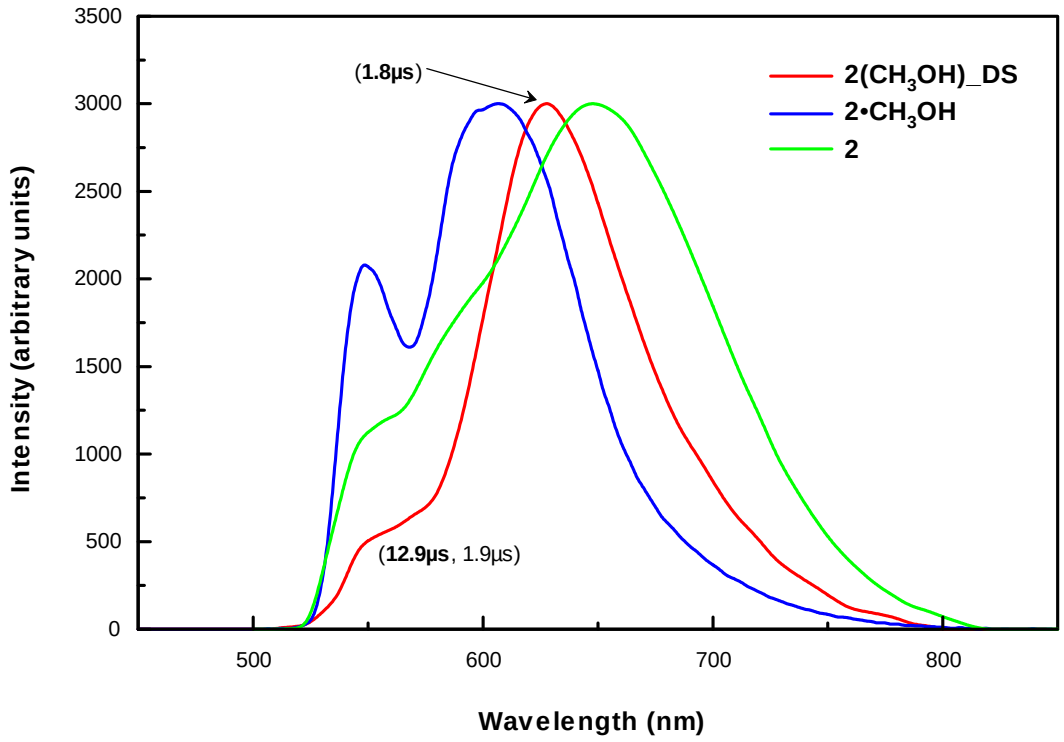

Figure 3.15 Solid state emission spectra of **2**, **2·CH$_3$OH**, and desolvated **2·CH$_3$OH** [**2·(CH$_3$OH)_DS**], recorded at 77 K. The values in brackets indicate the lifetime/s (τ) recorded for the different peaks. Note that two lifetimes indicates that the emission intensity decay curve is biphasic.

What also would be expected would be some contribution from excimeric emission given that **2·CH$_3$OH _DS** is bound to contain some form of free space – be it in the form of channels or voids. To this end we have deconvoluted the emission spectrum of

2·CH_3OH_DS: see Figure 3.16. This reveals the presence of a Gaussian component at 653 nm, indicative of excimeric emission; it also re-locates the position of the ^{3}MMLCT component to 625 nm, as well as very weak components representing the ^{3}MLCT emission at 550, 583 and 633 nm. Other than the relatively small change in the position of the ^{3}MMLCT band (which is most likely a result of a small change in the Pt∘∘∘Pt distance) the deconvulution is a very good match with that obtained by the deconvulution of the emission spectrum of **2·CH_3OH**. Thus the emission spectrum **2·CH_3OH_DS** at 77 K is characterised by multiple emission from ^{3}MLCT, ^{3}MMLCT and excimeric excited states.

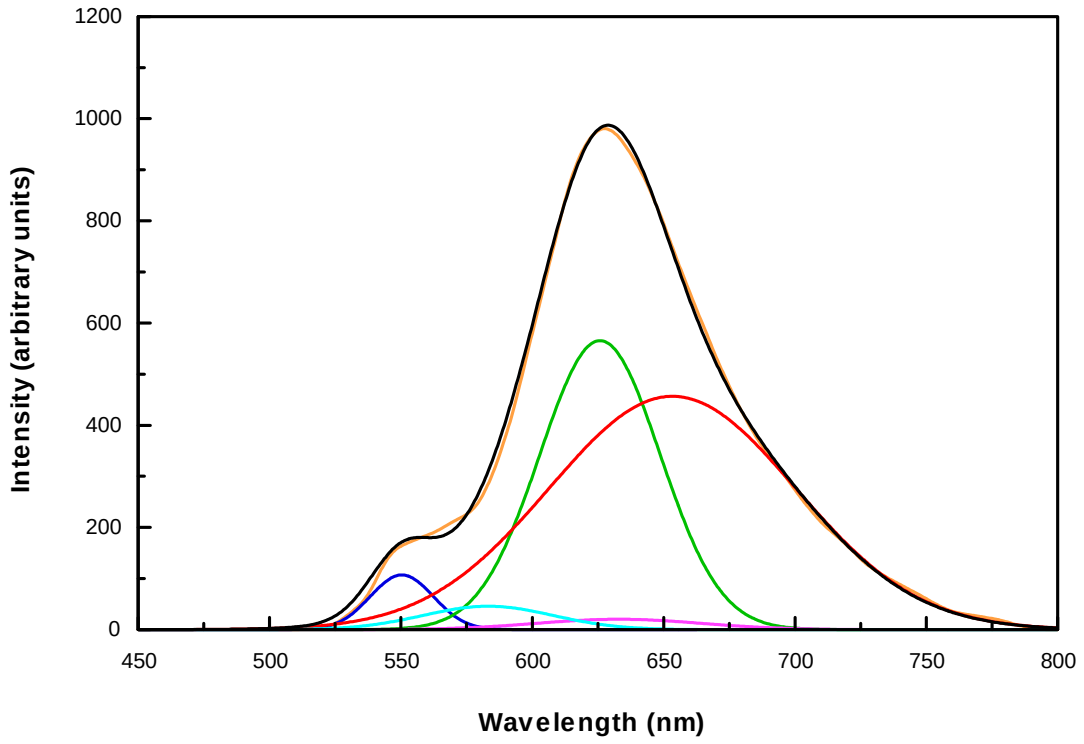

Figure 3.16 Solid state emission spectrum recorded at 77 K of desolvated **2·CH_3OH** [**2·(CH_3OH)_DS**], deconvoluted into five constituent Gaussian bands (r^2 = 0.9992; fit std error = 8.138). The colours follow from those in Figure 3.14.

We propose the following explanation for the small red-shift of λ_{em}^{max} upon desolvation of **2·CH_3OH** to give **2·CH_3OH_DS**: when the methanol solvent molecules are lost, the

Pt_2 dimer cations [linked by the d_{z^2}(Pt)-d_{z^2}(Pt) orbital interaction] are able to approach each other more closely. As a result the Pt∘∘∘Pt distance decreases slightly resulting in a stronger d_{z^2}(Pt)-d_{z^2}(Pt) orbital interaction, and thus the predicted red-shift of the ^{3}MMLCT component: see Section 1.3.1 of Chapter 1. It should also be noted that there is an apparent increase in the relative intensity of the excimeric band upon loss of methanol from the crystal lattice: compare the relative intensities of the excimeric emissions and ^{3}MMLCT emissions in Figures 3.14 and 3.16. This observation is the more significant if one takes into account that the "strength" of the Pt∘∘∘Pt interaction has increased from **2·CH_3OH** to **2·CH_3OH_DS**. In fact, this observation is consistent with our suggestion regarding the role played by the absence/presence of solvent molecules in modifying the potential energy barrier to the formation of excimers, i.e. when methanol is lost from the crystal lattice the potential energy barrier to the formation of excimers decreases resulting in a more intense excimeric emission.

5.3 Concluding remarks

From the results presented here, we propose that the arrangement of the cations in the crystal structures of **2**, **2·CH_3CN, 2·$(CH_3)_2CO$, 2·CH_3OH** and **2·CH_3OH_DS** does allow for emission from an excimeric excited state. However, whether the excimeric emission is actually observed depends on whether the potential energy barrier to excimer formation can be surmounted. Here the presence or absence of solvent molecules in the crystal lattice plays an important role; a critical role for **2·CH_3CN** and **2·$(CH_3)_2CO$** for which only monomeric ^{3}MLCT and no excimeric emission is observed. As we have shown for the methanol solvate, the actual size of the solvent molecule is also a factor; as indeed is the slight modification to the crystal structure of **2·CH_3OH**, in particular the presence of metallophilic Pt∘∘∘Pt interactions that clearly influence the emission by this solvate. The point is that in dealing with emission by a compound **in the solid state**, a number of factors can influence the emission; factors that are not relevant when dealing with an isolated chromophore in fluid solution.

6 Final comments

In conclusion, we note that the responses of crystals of **1—M** and **2** to the inclusion of solvent molecules are very different. In the case of **1—M**, a vapochromic response is observed for certain solvents; as such this material qualifies to be labelled as an "optical sensor". The reason for the change in colour and emission wavelength is simply that the crystal structure of the material changes on sorption (or desorption) of solvent; in particular the planar cations slide into new positions such that metallophilic interactions between the Pt atoms are disrupted (or facilitated). With **2**, there are hardly any changes in the crystal structure packing arrangement on sorption (or desorption) of solvent molecules, at least not with respect to acetonitrile and acetone; as a result there are no colour changes. The changes in the emission spectrum are indicative of changes in the potential energy barrier to the formation of the excimeric excited state, which is a consequence of changes in the amount of open space in the crystal lattice. With the sorption of methanol the situation is more complex, but methanol uptake is also not accompanied by a visual colour change; thus compound **2** does not qualify in any way as an optical sensor. What *is* interesting about **2**, is that it has an entirely novel porous metal-organic material, both in terms of the nature of construction and corkscrew shape of the channels; in particular one that allows for small molecule uptake and loss without loss of single crystallinity. Clearly more work is required in this respect: a study of the uptake and loss of gases, in particular hydrogen, is an example of one that should be done.

This leads to one last conspicuously unanswered question: **"Why does the introduction of a phenyl substituent in the 4'-position of the trpy ligand make such a difference to the way the cations position themselves in the solid, in particular when solvent molecules are sorbed or desorbed?"** The contrast between the inherent flexibility of the cation packing in **1—M** with that of inherent rigidity of the cation packing in **2** (and its solvates) can only be a result of the difference between the two, i.e. the 4'-phenyl substituent. Indeed all other features of the two cations, including the way in the final products are obtained, are the same. In the absence of the 4'-phenyl group it would be impossible to arrange the cations to give the ""brick-in-wall" packing arrangement

adopted by **2**. We say this because the π(pyridine)-π(phenyl) stabilising interactions illustrated in Figures 3.5(B) and (C) would not be possible. Thus, it appears that the extended aromatic system of the cations of **2** allows each cation to overlap with more than two cations, i.e. to form a wall of cations that is stabilised by multiple π-π interactions. It should be noted there are many examples of platinum(II) terpyridines with a phenyl group in the 4' position in literature, but none of which have the "brick-in-wall" packing arrangement of the cations. This shows that there are other factors that play a role in determining the crystal packing arrangement; one of which is probably the presence of the large pendant S atom on the isothiocyanate ligand. In conclusion, it is the combination of the 4'-phenyl group and the S atom that, taken together, force the $[Pt\{4'\text{-}(Ph)trpy\}(NCS)]^+$ cations into their positions in the porous metal-organic crystal structure of **2**.

4 EXPERIMENTAL

1 General reagents; synthetic and crystal growth procedures

1.1 Organic solvents

The acetonitrile used in the syntheses, for crystal growth and for generating vapours was obtained from SIGMA-ALDRICH and of the CHROMOSOLV® HPLC grade with a maximum of 0.02 % water. The diethyl ether, methanol (min. 99% assay) and acetone (min. 98% assay) used in reaction procedures and/or crystal growth were obtained from Saarchem and of the uniLAB® "Chemically Pure" grade.

1.2 Inorganic reagents and starting materials

The $AgNO_3$ was obtained from Saarchem and of the uniLAB® "Chemically Pure" grade. The (unlabelled) silver thiocyanate, i.e. AgSCN, was obtained from ALDRICH and used as received. The labelled silver thiocyanate, $AgS^{13}C^{15}N$, was prepared as follows using labelled $KS^{13}C^{15}N$ (from Isochem) as the starting material. To a solution of $KS^{13}C^{15}N$ (50 mg) in water (10 mL) was added an aqueous solution of $AgNO_3$ (10 mL, $AgNO_3$ in excess). The white precipitate of $AgS^{13}C^{15}N$ that forms was separated by filtration, washed with methanol and water and dried *in vacuo*. Yield 74 mg (87 %). Anal. Calc. for AgSCN (in test experiment): C, 7.23; N, 8.48. Found: C, 7.33; N, 8.16 %. IR (KBr, cm^{-1}): ν[$S^{13}C{\equiv}^{15}N$]: 2068w, 2024s, 2007s; *cf* ν[SC≡N] in unlabelled AgSCN: 2143w, 2101s, 2083s. The [Pt(trpy)Cl]SbF_6 and [Pt{4'-(Ph)trpy}Cl]SbF_6 precursors were synthesized using modified methods of those that described in ref. 10.

1.3 Ligands

The 2,2':6',2''-terpyridine was obtained from STREM and used as received. The 4'-phenyl-2,2':6',2''-terpyridine was prepared by the method of Constable.[115]

1.4 Synthetic procedures

The synthesis and isolation of the platinum complexes were performed in degassed solvents under dry nitrogen using standard vacuum line, cannulae transfer and Schlenk tube techniques.

2 Instrumentation

2.1 Microanalyses

Elemental analyses for %C, H and N were performed by Galbraith Laboratories Inc., Knoxville, Tennessee, USA.

2.2 Infrared, UV/vis absorption, NMR and mass spectroscopy

Fourier transform infrared (FTIR) spectra were measured using a Perkin Elmer Spectrum One spectrometer, and the samples prepared as KBr pellets. UV/vis absorption spectra were recorded at 22 ºC using a Perkin-Elmer Lambda 45 UV/vis spectrometer. ^{1}H (500 MHz), ^{13}C (125 MHz) and ^{15}N (50 MHz) NMR spectra were recorded at 22 ºC in CD_3CN on a Bruker Avance III 500 and 400 MHz spectrometers. A Bruker 600 MHz spectrophotometer with a Quad Nuclear Cold probe (QNP) was used to obtain the highly resolved ^{15}N NMR spectrum of [Pt(trpy)($^{15}N^{13}CS$)]SbF_6: see Figure 2.2 of Chapter 2. Chemical shifts were referenced to the solvent for the ^{1}H and ^{13}C spectra; to NH_3 for the ^{15}N spectra. Mass determinations were achieved by means of electrospray ionization mass spectrometry (ESIMS) using a Waters Acquity TOF mass spectrometer.

2.3 Emission spectroscopy

The instrument used for the measurement of emission spectra was a Photon Technologies Inc. (PTI) fluorescence spectrometer controlled by PTI's FeliX32© Version 1.1 software.[122] Steady state emission spectra were recorded using PTI's XenoFlash™ 300 Hz pulsed light source and gated emission scans with a delay of 95 μs, an integration window time of 100 μs and 50 pulses per channel (shots). Detection was by means of PTI's Model 814 Analog/Photon-Counting Photomultiplier Detector. The excitation wavelength was 420 nm for solid state samples; with the scattered light being removed by means of a suitable wavelength band-pass filter. The relative intensities of spectra where determined with the help of suitable neutral density filters. For the lifetime measurements, the excitation source was again the Xenon flash lamp, (set at 420 nm) with the (exponential) emission decay captured by the Photomultiplier Detector at a wavelength corresponding to the peak of interest, and analyzed by the FeliX32™ software. Excitation spectra were recorded by monitoring emission peak intensities as the excitation wavelength was varied over the given wavelength range. For the measurements at 77 K a PTI-supplied quartz cold finger filled with liquid nitrogen was used to hold the sample tube. This comprised a quartz NMR tube that had been widened at its mouth to fit a B14 female joint; into which a B14 cone (attached to a Rotaflow® stopcock) was inserted. By connecting the latter to a Schlenk line, it was possible to apply a vacuum and to purge a sample with argon prior to a measurement. This was done to prevent water in the atmosphere condensing on the inside of the sample tube. For the low temperature variable temperature emission measurements, the cryostat used was an Oxford Instruments DN1704 liquid-nitrogen-cooled system with an Oxford Instruments ITC4 temperature controller. For the variable temperature emission measurements at $T > 298$ K, the sample tube was inserted into a purpose-built thermostat; with a Rhomberg Thermoline® TC410 temperature controller that allowed the temperature at the sample to be measured to within ± 1 degree Kelvin; see Figure 4.1.

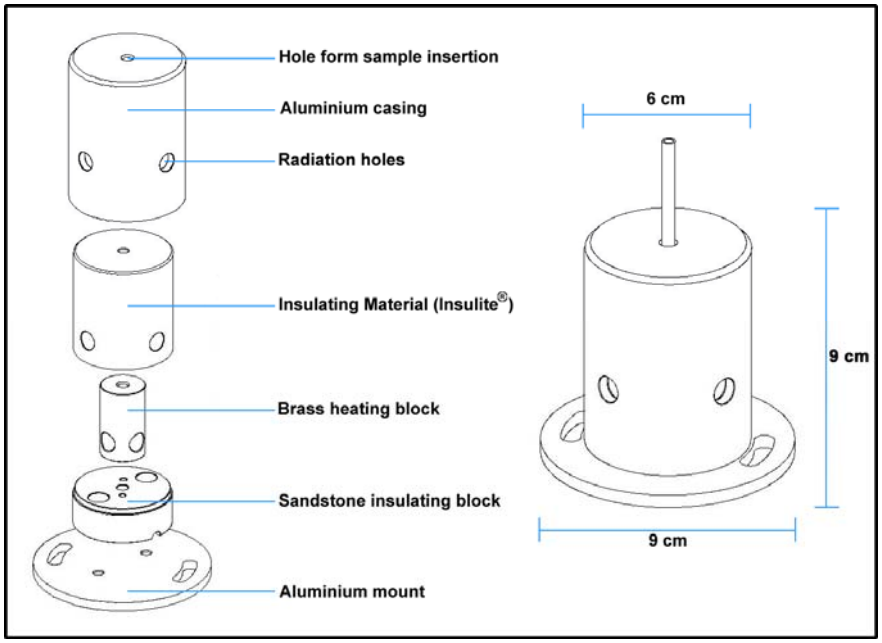

Figure 4.1 Schematic diagram showing the components and construction of the Heating Block (high temperature thermostat) used for high temperature (>295 K) emission studies, and phase change experiments.

2.4 Photography

The colour changes that **1—M** undergoes on cooling and/or heating and on exposure to solvent vapours was recorded using a KODAK® DX7630 camera.

3 Synthesis and characterisation of the platinum complexes

3.1 [Pt(trpy)(NCS)]SbF_6 (1—M)

A suspension of [Pt(trpy)Cl]SbF_6 (100 mg, 0.143 mmol) in acetonitrile (10 mL) was added to a suspension of a 10 % molar excess of AgSCN (26 mg) in acetonitrile (40 mL). The mixture was heated to reflux for 24 hrs. After cooling to room temperature, the AgCl precipitate that forms was first removed by cannular filtration; then the volume of solvent

was reduced *in vacuo* until saturation of the solution was achieved (~ 20 mL). The concentrated acetonitrile solution was transferred to the lower compartment of a dual chamber purpose-built apparatus; diethyl ether was added to the upper compartment. Slow vapour diffusion of diethyl ether into the concentrated acetonitrile solution resulted in the formation of yellow crystals over a period of ~ 10 days. (As discussed in Section 2 of Chapter 2, these yellow crystals are of the acetonitrile solvate, $[Pt(trpy)(NCS)]SbF_6 \cdot CH_3CN$, whose crystal structure is described in Section 4 of Chapter 2.) The yellow crystals were isolated by decantation of the mother liquor, and then washed with small amounts of cold acetonitrile followed by diethyl ether. Allowing the crystalline material to stand in air affords the maroon (desolvated) compound; the colour change from yellow to maroon takes approximately 10 seconds but, in order to ensure that all the acetonitrile solvent molecules are lost, the crystals were exposed to air for a full week. Analytical and spectroscopic data are as follows. $[Pt(trpy)(NCS)]SbF_6$: Yield 64 mg (62 %). Colour, maroon. Anal. calc. for $C_{16}H_{11}N_4F_6PtSSb$ (FW = 722.20 g mol^{-1}): C, 26.61; H, 1.54; N, 7.76 %. Found: C, 26.36; H, 1.59; N, 7.68 %. IR (KBr, cm^{-1}): ν[SC≡N]: 2097s; ν[S─CN]: 871m; ν(trpy): 1610s, 1557ms, 1479ms, 1418s, 881m; ν[SbF_6^-]: 656vs. ESIMS: *m/z* (relative intensity, ion): 486.0365 (100, M^{2+}). ^{1}H NMR (CD_3CN):* δ 8.52 (2H, m, $H_{5/5''}$); 8.43 (2H, t, $H_{3'/5'}$); 8.38 (2H, m, $H_{6/6''}$); 8.26-8.22 (3H, m, $H_{3/3'',4}$); 7.83 (2H, m, $H_{4/4''}$). ^{13}C NMR (CD_3CN):* δ 158.7 & 156.3 (4C, two s, quat.$C_{2/2'',2'/6'}$); 153.3 (2C, s, $C_{5/5''}$); 144.0 (2C, s, $C_{6/6''}$); 143.8 (2C, s, $C_{3'/5'}$); 130.7 (2C, s, $C_{4/4''}$); 126.8 & 125.3 (3C, two s, $C_{4,3/3''}$). UV/vis (1 μM in CH_3CN): λ_{max}/nm (ε, $M^{-1}.cm^{-1}$): 400 (54328); 375 (51239); 332 (183598); 325 (170625); 303 (123378); 289 (195747); 279 (225341); 269 (241612); 257 (285473).

* The chemical shifts listed are for the N-bound isomer that dominates in CD_3CN solution: see the discussion in Section 3 of Chapter 2.

3.2 $[Pt(trpy)(^{15}N^{13}CS)]SbF_6$ (isotopically labelled, 1─M)

The isotopically labelled compound was synthesised and purified using the same methods described in Section 3.1 above; except that $AgS^{13}C^{15}N$ was used in the metathesis

reaction. IR (KBr, cm^{-1}): ν[$S^{13}C{\equiv}^{15}N$]: 2015s; ν[$S{-}^{13}C^{15}N$]: 851m. For a summary of the ^{13}C and ^{15}N NMR data of the "$Pt^{15}N^{13}CS$" unit see Tables 3.1 and 3.2 in Section 3.3 of Chapter 3.

3.3 [Pt{4'-(Ph)trpy}(NCS)]SbF_6 (2)

To a suspension of [Pt{4'-(Ph)trpy}Cl]SbF_6 (100 mg, 0.129 mmol) in acetonitrile (10 mL) was added a suspension of a 10% molar excess of AgSCN (24 mg) in acetonitrile (40 mL). The mixture was heated to reflux for 24 hrs. After cooling to room temperature the resulting AgCl precipitate was removed by cannular filtration, and the volume of the solvent reduced *in vacuo*. The concentrated acetonitrile solution was transferred to the lower compartment of a dual chamber purpose-built apparatus; diethyl ether was added to the upper compartment. Slow vapour diffusion of diethyl ether into the concentrated acetonitrile solution resulted in the formation of yellow crystals over a period of ~ 7 days. (As discussed in Section 2 of Chapter 3, these yellow crystals are of the acetonitrile solvate, [Pt{4'-(Ph)trpy}(NCS)]$SbF_6{\cdot}CH_3CN$, whose crystal structure is described in Section 4 of Chapter 3.) The yellow crystals were isolated by decantation of the mother liquor, and then washed with small amounts of cold acetonitrile followed by diethyl ether. Allowing the crystalline material to stand in air affords the desolvated compound that is also yellow. In order to ensure that all the acetonitrile solvent is lost from the crystals, they were exposed to air for a full week. Analytical and infrared spectroscopic data are as follows. [Pt{4'-(Ph)trpy}(NCS)]SbF_6: Yield 71 mg (69 %). Colour, yellow. Anal. calc. for $C_{22}H_{15}N_4F_6PtSSb{\cdot}H_2O$ (FW = 816.30 g mol^{-1}): C, 32.37; H, 2.10; N, 6.86%. Found: C, 32.21; H, 1.95; N, 6.57 %. IR (KBr, cm^{-1}): ν[SC≡N]: 2095s; ν[S─CN]: 866m; ν[4'-(Ph)trpy]: 1610s, 1557ms, 1479ms, 1418s, 881m; ν[SbF_6^-]: 656vs. ESI MS: *m/z* (relative intensity, ion): 562.0670 (100, M^{2+}). ^1H NMR (CD_3CN):* δ 8.51 (4H, m, $H_{6/\,6'',3'/5'}$); 8.42 (4H, m, $H_{3/3'',2'''/6'''}$); 8.05 (1H, m, $H_{4'''}$); 7.83 (2H, q, $H_{4/4''}$); 7.71 (4H, m, $H_{5/5'',3'''/5'''}$). ^{13}C NMR (CD_3CN):* δ 157.8 (2C, s, quat.$C_{2/2''}$); 155.5 (2C, s, quat.$C_{2'/6'}$); 154.7 (1C, s, quat.$C_{1'''}$); 152.2 (2C, s, $C_{6/6''}$); 142.9 (2C, s, $C_{2'''/6'''}$); 142.4 (1C, s, quat.$C_{4'}$); 131.7 (2C, s, $C_{3'''/5'''}$); 129.7 (4C, s, $C_{5/5'',4/4''}$); 128.0 (1C, s, $C_{4'''}$); 125.8 (2C, s, $C_{3/3''}$); 122.1 (2C, s, $C_{3'/5'}$). UV/vis (1 μM in MeCN):

λ_{max}/nm (ε, M^{-1} cm^{-1}): 409 (20563); 387 (17055); 333 (46406); 319 (49463); 304 (49888); 290 (75511); 282 (68701); 273 (63785); 259 (64492).

* The chemical shifts listed are for the N-bound isomer that dominates in CD_3CN solution: see Section 3 of Chapter 3.

3.4 [Pt{4'-(Ph)trpy}($^{15}N^{13}CS$)]SbF_6 (isotopically labelled, 2)

The isotopically labelled compound was synthesised and purified using the same method described in Section 3.3 above; except that $AgS^{13}C^{15}N$ was used in the metathesis reaction. IR (KBr, cm^{-1}): ν[$S^{13}C{\equiv}^{15}N$]: 2019s; ν[$S{-}^{13}C^{15}N$]: 842m. For a summary of the ^{13}C and ^{15}N NMR data of the "$Pt^{15}N^{13}CS$" unit see Table 3.1 and 3.2 in Section 3.3 of Chapter 3.

4 Studies of the temperature dependence of the colour of 1—M

An analytically pure powder sample of [Pt(trpy)(NCS)]SbF_6 (**1—M**) was placed in a mortar, photographed at room temperature (maroon); then the mortar plus sample was cooled in liquid nitrogen and re-photographed (green). Note that when this sample is allowed to return to room temperature the original maroon colour is restored; and that this cycle can be endlessly repeated. To observe the colour changes on heating, the sample was again placed in a mortar: however, the mortar plus sample were now placed in an oven set at 473 K, and heated until such time as the orange colour detected at 473 K by controlled heating with the thermostat was observed; a photograph was then taken. Allowing this orange sample to cool to room temperature (under ambient conditions) returned it to its original maroon colour. Again, the thermochromic cycle is endlessly repeatable. To obtain photographs of the two (stable) high temperature phases, **1—O^{HTP}** (forms at T > 473 K) and **1—R^{HTP}** (forms at T > 518 K) the sample from the sample tube

inserted in the thermostat at the appropriate temperature was simply transferred to a mortar and photographed.

5 Solvation studies of 1—M

The sample of [Pt(trpy)(NCS)]SbF_6 (**1—M**) used for the solvation studies was an analytically pure powder that was ground and mixed thoroughly with finely divided KBr in the mass ratio 1:5; this facilitates the penetration of the crystallites by the solvent vapours and, at the same time, increases the surface area of the sample. The organic solvents used were of A.C.S. spectroscopic grade (from ALDRICH) with a maximum water content of ≤ 0.5 % for acetone. Solvent vapours for the vapochromic studies were generated by bubbling argon through the base of a modified Erlenmeyer flask (sealed at the top using a septa) containing the anhydrous solvent under a blanket of argon; onward transfer of the vapours was *via* cannulae inserted through a septum that sealed the flask. At the point where the argon line enters the flask there is a bulb with numerous small perforations; this creates many small bubbles of argon within the solvent (inside the flask) instead of large bubbles which are less efficient at evaporating the solvent.

5.1 Photography

The sample on a mortar was placed under an inverted beaker which had stopcocks added to the top and bottom. The inner wall of the beaker was lined with filter paper which had been wet with the appropriate solvent. A stream of dry solvent vapours, generated as described above, was directed into the inverted beaker by passing the cannulae through the lower stopcock. After an hour the cannulae was removed and both stopcocks where closed. The sample was left in this atmosphere, at room temperature, until the colour change from maroon to yellow was complete, after which the beaker was removed and a photograph taken. Note that the method used for solvation of **1—M** (described in Section 5.2 which follows) could not be employed here because the sample partially desolvated before it could be transferred to a mortar and photographed. If there was a colour change, it was to yellow and occurred virtually instantaneously; times taken for the material to

desolvate under ambient conditions back to the original maroon colour are given in Table 2.3.

5.2 Emission measurements

Emission measurements were only made with solvents whose vapours caused a colour change. Emission measurements were made at room temperature (~ 298 K) except for the acetonitrile solvate, for which it was necessary to record a spectrum at 77 K in order to observe finite emission: see insert in Figure 2.18.

For the emission measurements the sample was placed in the modified quartz NMR tube described in Section 2.3 above, but with a stopcock attached that allows for both purging of the sample with argon and the introduction into the sample space of the organic vapours *via* cannulae inserted through a septum. After purging, the sample was exposed to the stream of a solvent's vapour for about 1 hour, after which the cannulae was removed and the stopcock tap closed; it was kept closed with the solvent's vapour in contact with the sample for 3 hours. The envelope of solvent vapours was then removed by gently purging with argon. In this way, we ensured that the emission spectrum that was then recorded was on a "dry" solvated material; "dry" in the sense that no condensed solvent vapours were in contact with the surface of the sample.

6 Studies of vapour uptake/loss by single crystals of 2

6.1 Vapour uptake

A single crystal of [Pt{4'-(Ph)trpy}(NCS)]SbF_6 (**2**) was selected from the batch of crystals obtained by allowing acetonitrile to escape from the single crystals of **2·CH_3CN**, first isolated from the dual chamber crystal growth apparatus; the crystal was glued to a fibre attached to a brass pin, mounted on the diffractometer, and its crystal structure determined. (Different single crystals of **2** were used to test for the uptake of each of the

three solvents studied *viz* acetonitrile, methanol and acetone.) The brass pin was then transferred to a glass platform by inserting it into an adhesive that covered the platform. The glass platform was constructed by extending a B24 glass stopper, designed such that it when it is inserted through the mouth of a 250 mL two-necked round-bottomed Schlenk flask, the platform is positioned roughly halfway between the bottom of the flask and the stopper. The flask contained about 20 mL of solvent; note that, given the configuration, there can be no direct contact between the solvent and the platform. A vacuum was then applied to the flask until the solvent began to boil. In this way, the crystal was enveloped in a solvent's vapours at its vapour pressure at room temperature, in this case the laboratory temperature of about 20 ºC. (The relevant vapour pressures at 20 ºC are: acetonitrile ~ 43 torr; methanol ~ 125 torr and acetone ~ 230 torr.) The crystal was left exposed to the solvent vapours for 48 hrs. After this period, the brass pin with its crystal attached to the fibre was removed from the flask, and within a matter of minutes remounted on the diffractometer and cooled; to a temperature of 200 K for **2·CH$_3$CN** and **2·(CH$_3$)$_2$CO**, and a temperature of 180 K for **2·CH$_3$OH**. (The X-ray data collections of the solvates were done at low temperatures to slow down any potential loss of solvent.) The intensity data collection was then started, as usual with a determination of the cell parameters and followed by the measurement of a complete dataset. Following this procedure, reliable single crystal X-ray structure determinations could be made of **2·CH$_3$CN** and **2·CH$_3$OH**, i.e. both acetonitrile and methanol vapours were sorbed by a single crystal of **2**, without loss of single crystallinity. Acetone vapours were also sorbed by a single crystal of **2**, as evidenced by a crystal structure determination of **2·(CH$_3$)$_2$CO** obtained using the same procedure. However, this structure determination presented problems during refinement that indicated that the crystal was not of sufficient quality for the structure determination to be classified as completely reliable. For example, the internal *R*-factor was above 10 % and several atoms refined as "non-positive definite". We therefore circumvented the problem by simply growing single crystals of **2·(CH$_3$)$_2$CO** directly from acetone, using the same vapour diffusion method involving diethyl ether described in Section 1.5 above. These single crystals gave a reliable dataset at 200 K and it is this structure determination that is reported: see Table 4.1. Note that there is no significant difference between the atom positions determined for this "good"

crystal of **2·(CH$_3$)$_2$CO**, as compared to the atom positions obtained from the "unreliable" crystal structure determination on the crystal of **2·(CH$_3$)$_2$CO** obtained by exposure of **2** to vapours of acetone.

6.2 Vapour loss

The single crystals of **2·CH$_3$CN** and **2·(CH$_3$)$_2$CO** obtained using the procedure described in Section 6.1 above (and whose crystal structures had been subsequently determined) were exposed to ambient conditions for a period of 48 hrs. During this time the solvent molecules escaped from the crystal lattice without loss of single crystallinity; as evidenced by an X-ray crystal structure determination that showed the original crystal structure of **2**, i.e. without any solvent molecules present in the lattice: see **2_2nd.cif** and **2_deaect.cif** in the Supporting Information on the CD attached to the inside back cover of the thesis. The rate of desolvation could be increased by placing the single crystal (mounted on a brass pin) into the same Schlenk flask used for solvation; and reducing the pressure under vacuum with no solvent present. The same did not apply to the single crystal of the methanol solvate, **2·CH$_3$OH**, in that the solvent molecules are not as easily lost from the lattice. The desorption of methanol from single crystals of **2·CH$_3$OH** is the subject of an ongoing study.

7 Solvation studies of 2

The sample of yellow [Pt{4'-(Ph)trpy}(NCS)]SbF$_6$ (**2**) used for the solvation studies was (as for **1-M**) an analytically pure powder that was ground and mixed thoroughly with finely divided KBr in the mass ratio 1:5. The acetonitrile, methanol and acetone solvents used were of A.C.S. spectroscopic grade (from ALDRICH) with a maximum water content of ≤ 0.5 % for acetone. Solvent vapours were generated and exposure of the sample to the organic vapours in order to prepare the solvates for subsequent emission measurements was done exactly as described above in Section 5. However, since none of

the solvates of **2** gives detectable emission at room temperature, the emission measurements were made at 77 K. Note that solvation of **2** does not change its original yellow colour, and thus the uptake of solvent is not detectable with the naked eye. The solid state emission spectra of **2·CH$_3$OH** and **2·CH$_3$OH_DS** where deconvuluted using Peakfit™ Version 4.06.[123]

8 X-ray crystallography

8.1 Powder X-ray diffraction studies

X-ray diffraction analysis of the crystalline powder samples of **1—M**, **1—O^{HTP}**, **1—R^{HTP}** and **2** were carried out at room temperature (~ 295 K) on a Philips PW1050 diffractometer using monochromated CoKα radiation (λ = 1.7902 Å) from 3 to 40^o in 2θ with a scanning step of 0.02^o at 1^o per minute counting interval. The diffraction data were captured by a Sietronics 122D automated micro-processor attached to the X-ray diffractometer. Theoretical PXRD spectra were determined using Mercury 2.0.[124]

8.2 Single crystal X-ray diffraction studies

The instrument used for the collection of the X-ray intensity data was an Oxford Diffraction Xcalibur 2 CCD 4-circle diffractometer linked to an Oxford Cryostat System. The room temperature data collections were done at 295 K. For the low temperature data collections, the crystal was cooled to the appropriate temperature under a nitrogen vapor stream, and the data collected using MoKα radiation (2.0 kW, 0.71073 Å), 0.75 º frame widths, 20 s exposures at a crystal-to-detector distance of 50 mm, and omega 2-theta scans of -54.00 to 60.60 º or -54.00 to 60.75 º at θ = 30 º. The data were reduced with the program CrysAlis RED[125] (Version 170) using outlier rejection, scan speed scaling, as well as standard Lorentz and polarization correction factors. The structures were solved with SHELX97[126] using direct methods with all non-hydrogen atoms refined

anisotropically with SHELXL-97[126] (using WinGX[127] as an interface). Hydrogen atoms were geometrically constrained (C─H = 1.95 Å) using the appropriate AFIX command and refined isotopically with U_{iso} fixed at 1.20 times the equivalent isotropic temperature factor of the parent carbon atom. The one exception is the hydroxyl hydrogen of the methanol in **2·CH$_3$OH**; this hydrogen was assigned an individual and variable isotropic temperature factor. Note that two restraints were applied to the methanol, in particular to the O─H and C···H(O) distances so as to ensure a sensible C─O─H angle and O─H distance.

Particular attention was paid to the difference electron density map obtained after the final refinement of the crystal structure of **2**. This was to check for any evidence for water in the solvent accessible channels that amount to a volume of 320 Å^3 per unit cell at 200 K; see **2_1stcheckCIF** file in the Supporting Information on the CD attached to inside back cover of the thesis. The highest peak in the map of 1.86 e Å^3 is followed by other peaks that show small and systematic decreases in their electron densities, i.e. the electron density plot shows no dominant features. Nevertheless, we have plotted all peaks with an electron density of ≥ 1 e Å^3 (there are 10) to check where they are located in relation to the channels. In every case they are positioned within bonding distance of an atom in the cation (usually the Pt atom) or the Sb atom of the anion; thus there is simply no evidence at all for meaningful electron density in the channels. Of course, it is always possible to assign peaks as oxygen atoms with very small site occupation factors, i.e. to construct some kind of model that has water molecules disordered between different positions in the channels. Indeed, there is evidence from the microanalysis data (see Section 3.3 above) that there was water in the sample analysed by Galbraith Laboratories for %C, %H and %N. However, we are not sure at this stage whether this is superficial water that was simply picked-up during the course of the analysis; a further analysis under an atmosphere of nitrogen is planned. Also, we are of the opinion that, were water molecules present *in the single crystal* of **2**, they would be involved in hydrogen bonding, just like the methanol molecules in **2·CH$_3$OH** and, being H-bonded, would *not* be disordered. Finally, were water molecules present in the channels, they would have to be replaced rather easily by molecules of acetonitrile, methanol and acetone and we are not

convinced that this would be the case. In summary, the crystallographic evidence points to the existence of channels in **2** that are not only indisputably solvent accessible, but which are most likely actually empty.

Lattice constants, structure refinement details and final discrepancy indices for **1·CH_3CN─Y**, **2**, **2·CH_3CN**, **2·CH_3OH** and **2·$(CH_3)_2CO$** are given in Table 4.1.

Supporting Information Available: the crystallographic data for all the single crystal structure determinations are available in CIF format on the CD attached to the inside back cover of the thesis – this includes single crystal structure determinations not shown in Table 4.1 but referred to in the text. Each CIF file has a partner CHECKCIF file that shows the results of the basic structural check applied by the PLATON[128] program on the website of the International Union of Crystallography.[129]

Table 4.1 Crystal structure, data collection and refinement details for **1·CH_3CN─Y, 2, 2·CH_3CN, 2·CH_3OH and 2· $(CH_3)_2CO$**[a]**

Compound	**1·CH_3CN─Y**[b]	**2**[c]	**2·CH_3CN**[d]	**2·CH_3OH**[e]	**2· $(CH_3)_2CO$**[f]
Empirical formula	$C_{18}H_{114}F_6N_4PtSSb$	$C_{22}H_{15}F_6N_4PtSSb$	$C_{24}H_{18}F_6N_5PtSSb$	$C_{23}H_{19}F_6N_4OPtSSb$	$C_{25}H_{21}F_6N_4OPtSSb$
M_r	762.25	798.28	839.33	830.32	856.36
Crystal size/ mm	0.06 × 0.20 × 0.32	0.15 × 0.25 × 0.60	0.15 × 0.25 × 0.60	0.15 × 0.22 × 0.55	0.10 × 0.20 × 0.30
T / K	100	200	200	180	200
λ/ Å	0.71073	0.71073	0.71073	0.71073	0.71073
Crystal system	monoclinic	monoclinic	monoclinic	monoclinic	monoclinic
Space group	P-1	$P2_1/n$	$P2_1/n$	$P2_1/n$	$P2_1/n$
a/ Å	7.221(2)	9.6158(2)	9.9301(2)	9.7239(3)	9.7859(3)
b/ Å	12.271(3)	25.6118(7)	25.7960(9)	25.4860(7)	25.3897(8)
c/ Å	13.469(4)	10.3103(3)	10.347(3)	10.4632(3)	10.9182(4)
α/ º	109.77(2)	90	90	90	90
β/ º	95.37(2)	96.392(2)	100.060(2)	98.004(2)	98.355(3)
γ/ º	102.29(1)	90	90	90	90
V/ Å^3	1079.4(5)	2523.4(1)	2 609.7(8)	2 5 67.8(1)	2 684.0(2)
Z	2	4	4	4	4
D_c/g cm^{-3}	2.348	2.101	2.136	2.148	2.119
μ/ mm^{-1}	7.889	6.753	6.537	6.644	6.360
F(000)	712	1 496	1 584	1 568	1 624
θ Range/ º	2-25	2-25	2-25	2-25	2-25
Reflections collected (independent)	15 769 (4 747)	40 442 (9 037)	38 184 (8 961)	41 513 (9 434)	28 462 (5 291)
observed [$I > 2\sigma(I)$]	3 474	6 857	5 626	6 588	5 224
R_{int}	0.0438	0.0317	0.0423	0.0395	0.0338
No. refined parameters (restraints)	290 (0)	316 (0)	344 (0)	339 (2)	352 (0)
Final R_1 [$I > 2\sigma(I)$]	0.0243	0.0369	0.0803	0.0373	0.0865
Final wR_2 (all data)	0.0344	0.0821	0.2107	0.0862	0.1643
Max, Min Δρ/ e Å^{-3}	1.35, -.078	1.86, -1.51	5.66, -4.63	3.02, -2.30	3.36, -3.30

[a] All these crystals are yellow. [b] See **1MeCN100K.cif**. [c] Crystal selected from **1st** batch of crystals of **2**, i.e. the batch obtained after allowing acetonitrile to evaporate from the crystals of **2.CH_3CN** that originally formed in the crystal growth chamber: see **2_1st.cif**. [d] Crystal obtained by exposing **2_1st** to vapours of acetonitrile as described in Section 6.1 of Chapter 4: see **2MeCN_2nd.cif**. [e] Crystal obtained by exposing a different single crystal of **2** to vapours of methanol as described in Section 6.1 of Chapter 4: see **2MeOH.cif**. [f] Crystal grown **dir**ectly from acetone: see **2acet_dir.cif**.

References

[1] J. S. Field, R. J. Haines, D. R. McMillin, O. Q. Munro and G. C. Summerton, *Inorg. Chim. Acta*, 2005, **358**, 4567.

[2] D. K. Crites, C. T. Cunningham and D. R. McMillin, *Inorg. Chim. Acta*, 1998, **273**, 346.

[3] M. J. Hannon, P. S. Green, D. M. Fisher, P. J. Derrick, J. L. Beck, S. J. Watt, S. F. Ralph, M. M. Sheil, P. R. Barker, N. W. Alcock, R. J. Price, K. J. Sanders, R. Pither, J. Davies and A. Rodger, *Chem. Eur. J.*, 2006, **12**, 8000.

[4] E. M. A. Ratilla, H. M. Brothers II and N. M. Kostic, *J. Am. Chem. Soc.*, 1987, **109**, 4592.

[5] G. Lowe and T. Vilaivan, *J. Chem. Research*, 1996, 386.

[6] H.-S. Lo, S.-K. Yip, N. Zhu and V. W.-W. Yam, *J. Chem. Soc., Dalton Trans.*, 2007, 4386.

[7] P. Du, J. Schneider, P. Jarosz and R. Eisenberg, *J. Am. Chem. Soc.*, 2006, **128**, 7726.

[8] J. F. Michalec, S. A. Bejune, and D. R. McMillin, *Inorg. Chem.*, 2000, **39**, 2708.

[9] T. J. Wadas, Q.-M. Wang, Y.-J. Kim, C. Flaschenreim, T. N.Blanton and R. Eisenberg, *J. Am. Chem. Soc.*, 2004, **126**, 16841.

[10] R. Büchner, C. T. Cunningham, J. S. Field, R. J. Haines, D. R. McMillin and G. C. Summerton, *J. Chem. Soc., Dalton Trans.*, 1999, 711.

[11] M. H. Wilson, L. P. Ledwaba, J. S. Field and D. R. McMillin, *J. Chem. Soc., Dalton Trans.*, 2005, 2754.

[12] J. A. Bailey, M. G. Hill, R. E. Marsh, V. M. Miskowski, W. P. Schaefer and H. B. Gray, *Inorg. Chem.*, 1995, **34**, 4591.

[13] D. R. McMillin and J. J. Moore, *Coord. Chem. Rev.*, 2002, **229**, 113.

[14] D. K. C. Tears and D. R. McMillin, *Coord. Chem. Rev.*, 2001, **211**, 195.

[15] J. S. Field, L. P. Ledwaba, O. Q. Munro and D. R. McMillin, *CrystEngComm*, 2008, **10**, 740.

[16] G. C. Summerton, PhD Thesis, University of Natal, Pietermaritzburg, Republic of South Africa, 1997.

[17] V. W.-W. Yam, R. P.-L. Tang, K. M.-C. Wong and K.-K. Cheung, *Organometallics*, 2001, **20**, 4476.

[18] J. S. Field, R. J. Haines, D. R. McMillin and G. C. Summerton, *J. Chem. Soc., Dalton Trans.*, 2002, 1369.

[19] J. S. Field, J.-A. Gertenbach, R. J. Haines, L. P. Ledwaba, N. T. Mashapa, D. R. McMillin, O. Q. Munro and G. C. Summerton, *J. Chem. Soc., Dalton Trans.*, 2003, 1176.

[20] J. F. Michalec, S. A. Bejune, D. G. Cuttell, G. C. Summerton, J. A. Gertenbach, J. S. Field, R. J. Haines and D. R. McMillin, *Inorg. Chem.*, 2001, **40**, 2193.

[21] C. S. Peyratout, T. K. Aldridge, D. K. Crites and D. R. McMillin, *Inorg. Chem.*, 1995, **34**, 4484.

[22] T. K. Aldridge, E. M. Stacey and D. R. McMillin, *Inorg. Chem.*, 1994, **33**, 722.

[23] H.-K. Yip, L.-K. Cheng, K.-K. Cheung and C.-M. Che, *J. Chem. Soc., Dalton Trans.*, 1993, 2933.

[24] L. P. Ledwaba, *PhD Thesis*, University of KwaZulu-Natal, Pietermaritzburg, Republic of South Africa, 2005.

[25] S. E. Hobert, J. T. Carney and S. D. Cummings, *Inorg. Chim. Acta*, 2001, **318**, 89.

[26] K. M.-C. Wong and V. W.-W. Yam, *Coord. Chem. Rev.*, 2007, **251**, 2477.

[27] M. G. Hill, J. A. Bailey, V. M. Miskowiski and H. B. Gray, *Inorg. Chem.*, 1996, **35**, 4585.

[28] K. M.-C. Wong, N. Zhu and V. W.-W. Yam, *J. Chem. Soc., Chem. Commun.*, 2006, 3441.

[29] A. J. Goshe, I. M. Steele and B. Bosnich, *J. Am. Chem. Soc.*, 2003, **125**, 444.

[30] E. Sakuda, A. Funahashi and N. Kitamura, *Inorg. Chem.*, 2006, **45**, 10670.

[31] X. Zhou, H.-X. Zhang, Q.-J. Pan, B.-H. Xia and A.-C. Tang, *J. Phys. Chem. A.*, 2005, **104**, 8809.

[32] J. A. Bailey, V. M. Miskowiski and H. B. Gray, *Inorg. Chem.*, 1993, **32**, 369.

[33] J. S. Field, R. J. Haines, L. P. Ledwaba, R. McGuire Jr., O. Q. Munro, M. R. Low and D. R. McMillin, *J. Chem. Soc., Dalton Trans.*, 2007, 192.

[34] R. Büchner, J. S. Field, R. J. Haines, C. T. Cunningham and D. R. McMillin, *Inorg. Chem.*, 1997, **36**, 3952.

[35] R. Büchner, J. S. Field, R. J. Haines, L. P. Ledwaba, R. McGuire Jr., D. R. McMillin and O. Q. Munro, *Inorg. Chim. Acta*, 2007, **360**, 1633.

[36] D.-L. Ma, T. Y.-T. Shum, F. Zhang, C.-M. Che and M. Yang, *J. Chem. Soc., Chem. Commun.*, 2005, 4675.

[37] K. M.-C. Wang, W.-S. Tang, X.-X. Lu, N. Zhu, and V. W.-W. Yam, *Inorg. Chem.*,2005, **44**, 1492.

[38] W.-S. Tang, X.-X. Lu, K. M.-C. Wong and V. W.-W. Yam, *J. Mater. Chem.*, 2005, **15**, 2714.

[39] P. Du, K. Knowles, and R. Eisenberg, *J. Am. Chem. Soc*, 2008, **130**, 12576.

[40] K. M.-C. Wong, W.-S. Tang, B. W.-K. Chu, N. Zhu, and V. W.-W. Yam, *Organometallics*, 2004, **23**, 3459.

[41] S. J. Lippard and M. Howe-Grant, *J. Biochemistry*, 1979, 5762.

[42] J. Depriest, G. Y. Zheng, N. Goswami, D. M. Eichorn, C. Woods and D. P. Rillema, *Inorg. Chem.*, 2000, 1955.

[43] J. J. Moore, J. J. Nash, P. E. Fanwick and D. R. McMillin, *J. Am. Chem. Soc., Inorg. Chem.*, 2002, **41**, 6387

[44] H. Yersin and D. Donges, *Top. Curr. Chem.*, 2001, 81.

[45] M. K. DeArmond and J. E. Hills, *J. Chem. Phys.*, 1971, **54**, 2247.

[46] M. Maestri, D. Sandrini, V. Balzani, A. von Zelwesky, C. Deuschel-Cornioley and P. Jolliet, *Helv. Chim. Acta*, 1988, **71**, 1053.

[47] D. S. Martin; *"Extended interactions between metal ions"*, ed. L. V. Innerannte, ACS Symp. Ser. 5, *ACS*, Washington, DC, 1974, 254.

[48] W. B. Connick, R. E. Marsh, P. Schaefer and H. B. Gray, *Inorg. Chem.*, 1997, **36**, 913.

[49] C. A. Hunter and J. K. M. Saunders, *J. Am. Chem. Soc.*, 1990, **112**, 5525.

[50] C. Janiak, *J. Chem. Soc., Dalton Trans.*, 2000, 3885.

[51] V. W.-W. Yam, K. M.-C. Wong and N. Zhu, *J. Am. Chem. Soc.*, 2002, **124**, 6506.

[52] V. M. Miskowiski and V. H. Houlding, *Inorg. Chem.*, 1989, **28**, 1529.

[53] C. N. Pettijohn, E. B. Jochnowitz, B. Chuong, J. K. Nagle and A. Vogler, *Coord. Chem. Rev.*, 1998, **171**, 85.

[54] (a) K.-T. Yam, C.-M. Che and K.-C. Cho, *J. Chem. Soc., Dalton Trans.*, 1991, 1077. (b) H. Kunkely and A. Vogler, *J. Am. Chem. Soc.*, 1990, **112**, 5625.

[55] I. Bertini and A. Sabatini, *Inorg. Chem.*, 1996, **5**, 1025.

[56] T. Förster, *Angew. Chem., Int. Ed.(Engl. Transl.)*, 1969, **8**, 333

[57] (a) J. B. Birks, *"The photophysics of aromatic molecules"*, Wiley-Interscience, New York, 1970. (b) J. B. Birks, D. J. Dyson and I. H. Munro, *Proc. Phys. Soc. (London)*, 1963, **275**, 575.

[58] W. T. Yip and D. H. Levy, *J. Phys. Chem.*, 1996, **100**, 11539.

[59] See Abstract of: Y. N. Kukushkin, L. V. Vrublevskaya, R. A. Vlasova, T. S. Isachkina, E. S. Postnikova and N. K. Sheleshkova, *Russ. J. Inorg. Chem. (Engl. Transl.)*, 1985, **30**, 224.

[60] J. L. Burmeister and F. Basolo, *Inorg. Chem.*, 1964, **3**, 1587.

[61] J. L. Burmeister, *Coord. Chem. Rev.*, 1966, **1**, 205.

[62] J. L. Burmeister, *Coord. Chem. Rev.*, 1968, **3**, 225.

[63] (a) M. J. Coyer, M. Croft, J. Chen and R. H. Herber, *Inorg. Chem.*, 1992, **31**, 1752. (b) M. J. Coyer, R. H. Herber, J. Chen, M. Croft and S. P. Szu, *Inorg. Chem.*, 1994, **33**, 716.

[64] S. Kishi and M. Kato, *Inorg. Chem.*, 2003, **42**, 8728.

[65] R. G. Pearson, *J. Am. Chem. Soc.*, 1963, **3**, 1587.

[66] K. F. Purcell and J. C. Kotz, *"Inorganic Chemistry"*, W. B. Saunders Press, Philadelphia, 1977, 618-619.

[67] J. L. Burmeister, R. L. Hassel and R. J. Phelan, *Inorg. Chem.*, 1971, **10**, 2032.

[68] M. F. Farona and A. Wojcicki, *Inorg. Chem.*, 1965, **4**, 857.

[69] R. G. Kidd and H. G. Spinney, *J. Am. Chem. Soc.*, 1981, **103**, 4579.

[70] J. M. Homan, J. M. Kawamoto and G. L. Morgan, *Inorg. Chem.*, 1970, **9**, 2533.

[71] T. G. Appelton, J. R. Hall and S. F. Ralph, *Inorg. Chem.*, 1985, **24**, 4685.

[72] P. S. Pregosin, H. Streit and L. M. Venanzi, *Inorg. Chim. Acta*, 1980, **38**, 237.

[73] R. J. Goodfellow, S. J. Anderson and P. L. Goggin, *J. Chem. Soc., Dalton Trans.*, 1976, 1959.

[74] L. Prasad and F. E. Smith, *Acta Crystallogr., Sect.B: Struct. Crystallogr. Cryst. Chem.*, 1982, **38**, 1815.

[75] L. Hou, D. Li, Y.-G. Yin, and S.W.Ng, *Acta Crystallogr., Sect. E: Struct. Rep. Online*, 2005, **61**, m21.

[76] M. I. Arriortua, J. L. Mesa, T. Rojo, T. Debaerdemaeker, D. Beltran-Porter, H. Stratemeier and D. Reinen, *Inorg. Chem.*, 1988, **27**, 2976.

[77] C. Mantel, C. Baffert, I. Romero, A. Deronzier, J. Pecaut, M.-N .Collomb and C. Duboc, *Inorg. Chem.*, 2004, **43**, 6455.

[78] S. A. Cotton, V. Franckevicius, R. E. How, B. Ahrens, L. L. Ooi, M. F. Mahon, P. R. Raithby and S. J. Teat, *Polyhedron*, 2003, **22**, 1489.

[79] D. V. Naik and W. R. Scheidt, *Inorg. Chem.*, 1973, **12**, 272.

[80] S. M. Zakeeruddin, M. K. Nazeeruddin, P. Pechy, F. P. Rotzinger, R. Humphry-Baker, K. Kalyanasundaram, M. Gratzel, V. Shklover and T. Haibach, *Inorg. Chem.*, 1997, **36**, 5937.

[81] J. Rall, F. Weingart, D. M. Ho, M. J. Heeg, F. Tisato and E. Deutsch, *Inorg. Chem.*, 1994, **33**, 3442.

[82] L. Hou, D. Li and S. W. Ng, *Acta Crystallogr., Sect. E: Struct. Rep. Online*, 2004, **60**, m1734.

[83] R. C. T. Rojo, L. Lezama, M. I. Arriortua, K. Urtiaga and G. Villeneuve, *J. Chem. Soc. Dalton Trans.*, 1991, 1779.

[84] F. A. Cotton and G. Wilkinson, *"Advanced Inorganic Chemistry: A Comprehensive Text"*, 2nd Edition, J. Wiley and Sons, Inc., London, 1966.

[85] *IUPAC Compendium of Chemical Terminology*: 2nd Edition 1997, **68**, 2279.

[86] L. J. Grove, J. M. Rennekamp, H. Jude and W. B. Connick, *J. Am. Chem. Soc.*, 2004, **126**, 1594.

[87] (a) C. E. Buss and K. R. Mann, *J. Am. Chem. Soc.*, 2002, **124**, 1031. (b) S. M. Drew, D. E. Janzen, C. E. Buss, D. I. MacEwan, K. M. Dublin and K. R. Mann, *J. Am. Chem. Soc.*, 2001, **123**, 8414.

[88] M. Kato, A. Omura, A. Toshikawa, S. Kishi and Y. Sugimoto, *Angew. Chem. Int. Ed.*, 2002, **41**, 3183.

[89] S. C. F. Kui, S. S.-Y. Chui, C.-M. Che and N. Zhu, *J. Am. Chem. Soc.*, 2006, **128**, 8297.

[90] J. Lefebvre, R. J. Batchelor and D. B. Leznoff, *J. Am. Chem. Soc.*, 2004, **126**, 16117.

[91] Y. Kunugi, K. R. Mann, L. L. Miller and C. L. Exstrom, *J. Am. Chem. Soc.*, 1998, **120**, 589.

[92] W. B. Connick, L. M. Henling, R. E. Marsh and H. B. Gray, *Inorg. Chem.*, 1996, **35**, 6261.

[93] V. M. Miskowiski and V. H. Houlding, *Inorg. Chem.*, 1991, **30**, 4446.

[94] S.-W. Lai, M. C.-W. Chan, T.-C. Cheung, S.-M. Peng and C.-M. Che, *Inorg. Chem.*, 1999, **38**, 4046.

[95] G. Blasse and B. C. Grabmaier, *"Luminescent Materials"*, Springer-Verlag, Berlin, Germany, 1994, 103-104.

[96] http://bilbo.chm.uri.edu/SST/thermochromic.html; a webpage from the University of Rhode Island Chemistry Department website.

[97] www.tut.fi/units/ms/teva/projects/intelligenttextiles/chromic.htm; a webpage from the Tampere University of Technology Materials Science Department.

[98] C. Astin, D. Talbot and P. Goodhew, *Phys. Educ.*, 2002, 519.

[99] P. U. Biedermann, J. J. Stezowski and I. Agranat, *Chem. Comm.*, 2001, 954.

[100] T. Ren, D. P. Bancroft, W. I. Sundquist, A. Masschelein, M. V. Keck and S. J. Lippard, *J. Am. Chem. Soc.*, 1993, **115**, 11341.

[101] D. Leznoff, 88th Canadian Society of Chemistry Conference, May 28th – June 1st, 2005, Saskatoon, Canada. (www.csc2005.ca)

[102] (a) See Abstract of: A. M. Seayard and D. M. Antonelli, *Adv. Mater.*, 2004, **16**, 765. (b) M. D. Ward, *Science*, 2003, **300**, 1104. (c) J. L. C. Rowsell and O. M. Yaghi, *Angew. Chem., Int. Ed.*, 2005, **44**, 4670.

[103] (a) T. Burchell and M. Rogers, SAE Techol. Pap. Ser., 2000, 2000-01-2205. (b) A. R. Millward and O. M. Yaghi, J. Am. Chem. Soc., 2005, **127**, 17998. (c) www.eere.energy.gov/hydrogenandfeulcells/docs/hc_h2_storage.doc

[104] S. Noro, S. Kitagawa, M. Kondo and K. Seki, *Angew. Chem., Int. Ed.*, 2000, **39**, 2082.

[105] (a) O. M. Yaghi, M. Eddaoudi, D. B. Moler, H. Li, T. M. Reineke and M. O'Keeffe, *Acc. Chem. Res.*, 2001, **34**, 319. (b) O. M. Yaghi, M. O'Keeffe, N. W. Ockwig, H. K. Chae, M. Eddaoudi and J. Kim, *Nature*, 2003, **423**, 705.

[106] (a) O. M. Yaghi, H. Li, C. Davis, D. Richardson and T. L. Groy, *Acc. Chem. Res.*, 1998, **31**, 474.

[107] (a) M. Eddaoudi, J. Kim, N. Rosi, D. Vodak, J. Wachter, M. O'Keeffe and O. M. Yaghi, *M. Science*, 2002, **295**, 469. (b) D. Britt, D. Tranchemontange and O. M. Yaghi, PNAS, 2008, 105, 11623. (article available at: www.pnas.org/cgi/doi/10.1073/pnas.0804900105)

[108] L. Dobrzanska, G. O. Lloyd, H. G. Raubenheimer and L. J. Barbour, *J. Am. Chem. Soc.*, 2005, **127**, 13134.

[109] H. Li, M. Eddaoudi, T. L. Groy and O. M. Yaghi, *J. Am. Chem. Soc.*, 1998, **120**, 8571.

[110] L.-G. Zhu, H.-P. Xiao and J. Y. Lu, *Inorg. Chem.*, 2004, **7**, 94.

[111] B. Rather and M. J. Zaworotko, *J. Am. Chem. Soc.*, 2003, 830.

[112] J. Y. Lu and A. M. Babb, *J. Am. Chem. Soc.*, 2002, 1340.

[113] K. Biradha and M. Fujita, *Angew. Chem., Int. Ed.*, 2002, **41**, 3392.

[114] R. J. Goodfellow and S. J. Anderson, *J. Chem. Soc., Dalton Trans.*, 1977, 1683.

[115] E. C. Constable, J. Lewis, M. C. Liptrot and P. R. Raithby, *Inorg. Chim. Acta*, 1990, **178**, 47.

[116] T. Steiner and G. R. Desiraju, *Chem. Commun.*, 1998, 891.

[117] M. J. Calhorda, *Chem. Commun.*, 2000, 801

[118] http://en.wikipedia.org/wiki/Metal-organic_framework

[119] L. J. Barbour, X-SEED Version 2.0, program for the analysis of single crystal structure determinations, University of Stellenbosch, Republic of South Africa, 1999.

[120] M. L. Connolly, Molecular Surface Package Version 3.9.3, program for the determination of atom (solvent) accessible areas and volumes, California, United States of America, 2006.

[121] J. J. Moore, J. J. Nash, P. E. Fanwick and D. R. McMillin, *Inorg. Chem.*, 2002, **41**, 6387

[122] Felix32© Analysis Version 1.1 (Build 51 Beta 8), program for the analysis of emission spectra, 2003

[123] Peakfit™ Version 4.06, AISN software, 1991.

[124] www.ccdc.cam.ac.uk/mercury, Mercury 1.4.2 (Build 2), program for the analysis of single crystal structure determinations and determination of theoretical powder X-ray diffraction patterns, University of Cambridge, United kingdom.

[125] Oxford Diffraction Ltd., Abingdon, Oxford OX14 1RL, UK, 2003.

[126] G. M. Sheldrick, SHELXS97 and SHELXL-97/2, programs for crystal structure determination and refinement, University of Göttingen, Germany, 1997.

[127] L. J. Farrugia, *J. Appl. Cryst.*, 1999, **32**, 837-838

[128] A. L. Spek, PLATON, A multipurpose crystallographic tool; Utrecht University, Utrecht, The Netherlands, 2001.

[129] International Union of Crystallography website: www.iucr.org